Probing Entanglement and Symmetry Breaking Orders via Spectroscopies and Machine Learning

by

Tongtong Liu

B.S. Physics, Peking University, 2017

Submitted to the Department of Physics
in partial fulfillment of the requirements for the degree of
Doctor of Philosophy in Physics, Statistics, and Data Science
at the
MASSACHUSETTS INSTITUTE OF TECHNOLOGY
September 2023

Author .....
Department of Physics
August 18, 2023

Certified by .....
Mingda Li
Class '47 Career Development Professor,
Associate Professor of Nuclear Science and Engineering
Thesis Supervisor

Certified by .....
Paola Cappellaro
Ford Professor of Engineering,
Professor of Nuclear Science and Engineering,
Professor of Physics
Thesis Supervisor

Accepted by .....
Lindley Winslow
Associate Department Head of Physics

Probing Entanglement and Symmetry Breaking Orders via Spectroscopies and Machine Learning

by

Tongtong Liu

Submitted to the Department of Physics
on August 18, 2023, in partial fulfillment of the
requirements for the degree of
Doctor of Philosophy in Physics, Statistics, and Data Science

Abstract

Quantum materials are essential components in the development of advanced technologies, including magnetic-field sensors, energy-related technologies, and quantum computers. Especially, the search of highly entangled quantum materials is crucial, because entanglement is a resource in quantum information applications. A key step towards finding and fabricating highly-entangled materials is to develop experimental and theoretical methods to characterize entanglement. In large-scale solid-state systems, the experimental characterization relies on spectroscopies, including X-ray and neutron spectroscopies. Among different conceptual and mathematical formalisms of entanglement, multipartite entanglement has gained significance due to its accessibility through local probe techniques such as spectroscopies. The resonant inelastic X-ray scattering (RIXS) is an advanced X-ray spectroscopic technique that can probe collective excitations arising from charge, spin, and orbital degrees of freedom, which makes it suitable to characterize multipartite entanglement. RIXS also exhibits potential that extends beyond current understandings, under exceptional precision, it can measure four-point correlations beyond the capability of other spectra techniques, which inspires new entanglement probes.

This dissertation contains many aspects of probing entanglement and symmetry breaking orders using both spectroscopies and machine learning. In the first part about probing entanglement using spectroscopies, we will introduce a theoretical proposal for using RIXS to probe entanglement. We propose a new RIXS technique that can extract four-point correlations beyond the scope of the spin and charge structure factors. We verify our method using computational RIXS spectra and theoretically propose multipartite entanglement witnesses based on the four-point correlations for general fermion systems. Building upon the theme of extracting information from materials using spectroscopies, we further present two theoretical works that predict symmetry breaking orders in two-dimensional systems, which can be directly visualized using spectroscopic techniques. (1) We investigate local signatures of quantum Hall ferroelectric and nematic states arising near impurities that can be observed via Scanning Tunnelling Microscopy (STM). (2) We study charge orders at the frac-

tional fillings in twisted transition metal dichalcogenide (TMD) bilayers that can be observed directly via STM.

The second part is about the prediction of magnetic orders using machine learning. We'll present a machine-learning model based on the Euclidean equivariant graph neural network (E3NN) which preserves the crystallographic symmetry, that is trained to predict magnetic orders (ferromagnetic, antiferromagnetic, and non-magnetic) and magnetic propagation vectors (zero or nonzero) with the crystal structures as input. The descriptor used has the advantage to encode general crystal structures of any space group while retaining all spatial information, this characteristic holds significant potential for advancing material science studies.

Thesis Supervisor: Mingda Li
Title: Class '47 Career Development Professor,
Associate Professor of Nuclear Science and Engineering

Thesis Supervisor: Paola Cappellaro
Title: Ford Professor of Engineering,
Professor of Nuclear Science and Engineering,
Professor of Physics

Acknowledgments

During my graduate studies at MIT, I am extremely fortunate to have the support of many people. Without them, it would not have been possible for me to navigate this challenging yet rewarding journey and ultimately achieve my goal.

First of all, I am very grateful to my advisor, Professor Mingda Li, for giving me a second chance to continue my research after leaving my initial research group. His consistent encouragement and support allowed me to pursue my research interests. I would also like to extend my gratitude to my co-advisor, Professor Paola Cappellaro, for her valuable suggestions regarding presentations and my thesis. Furthermore, my committee members, Professor Xiao-Gang Wen and Professor Marin Soljačić, provided invaluable insights and guidance in the fields of science and research. Additionally, I would like to acknowledge Professor Yao Wang for his mentorship in the RIXS project and his career development advice.

I wish to express my appreciation to the incredible collaborators with whom I had the pleasure of working. Professor Yao Wang, with whom I worked on the RIXS projects, Professor Yang Zhang, who collaborated with me on the TMD project, and Dr. Pok Man Tam along with Professor Inti Sodemann, who collaborated with me on the valley quantum Hall project. I must also thank my former advisor, Professor Liang Fu, for introducing me to the world of condensed matter theory and guiding my early studies. Many individuals have contributed to my interest in science. Professor Cheng Chin at the University of Chicago accepted me as an undergraduate intern, which influenced my decision to pursue a Ph.D. My undergraduate advisor, Professor Biao Wu, kindled my fascination with condensed matter physics. The captivating lectures by Professor Xiao-Gang Wen and Professor Aram Harrow at MIT further fueled my interest in the interdisciplinary aspects of condensed matter physics and quantum information science. Lastly, my advisor, Professor Mingda Li, led me into the new field of machine learning.

I am grateful to have shared this journey with my amazing colleagues from the

Quantum Measurement Group: Dr. Zhantao Chen, Dr. Nina Andrejevic, Thanh Nguyen, Nathan Drucker, Ryotaro Okabe, Abhijatmedhi (Earth) Chotrattanapituk, Dr. Manasi Mandal, Artittaya (Tiya) Boonkird, and Phum Siriviboon. The engaging research discussions and the good times we shared will be cherished memories.

Last but not least, I want to extend my heartfelt gratitude to my parents for their unwavering support. I also want to thank my boyfriend, Congjian Ni, for standing by me, providing encouragement during the most challenging times, and supporting me throughout this journey.

Contents

List of Figures

Chapter 1

Introduction

Quantum materials are essential components in the development of advanced technologies, including magnetic-field sensors[1], energy-related technologies[2], and quantum computers[3]. In this context, the search of highly entangled quantum materials is crucial, because entanglement is a quantum resource in information applications and topological quantum computing[4, 5, 6]. There are two central questions in the study of entanglement, (1) How to detect entanglement in the laboratory, and (2) How to characterize and quantify entanglement theoretically. Both of these questions are key steps toward discovering and fabricating highly-entangled materials. In large-scale solid-state systems, the experimental characterization relies on spectroscopies that measure certain correlation functions of the systems, including X-ray, neutron, and photoemission spectroscopies. The most commonly used theoretical formalism to characterize entanglement is the Von Neumann entanglement entropy, however, it is hard to measure the entanglement entropy using spectroscopies. The multipartite entanglement has gained significance due to its accessibility through local probe techniques such as spectroscopies[7]. The resonant inelastic X-ray scattering (RIXS) [8] is an advanced X-ray spectroscopy technique that can probe collective excitations arising from charge, spin, and orbital degrees of freedom, which makes it suitable to characterize multipartite entanglement[9].

Besides the quantum entanglement, symmetry breaking in the context of classical Landau theory plays a crucial role in understanding the macroscopic properties of

materials. This is because most physical phenomena in the materials are dictated by their underlying symmetry breaking, including, but not limited to, spin-polarization effects, valley-contrasting physics, unconventional superconductivity, nematic order, and ferroelectricity. Symmetry breaking phases often exhibit distinct patterns or signatures that can be observed through experimental techniques including thermal measurements, transport measurements, and spectroscopies. Among other spectral techniques, scanning tunneling microscopy adds spatial resolution. In some cases, it enables local determination of the symmetry breaking, and can even provide a direct image of the order parameters of the symmetry breaking, providing fundamental insights into the behavior of materials and offering opportunities for technological applications.

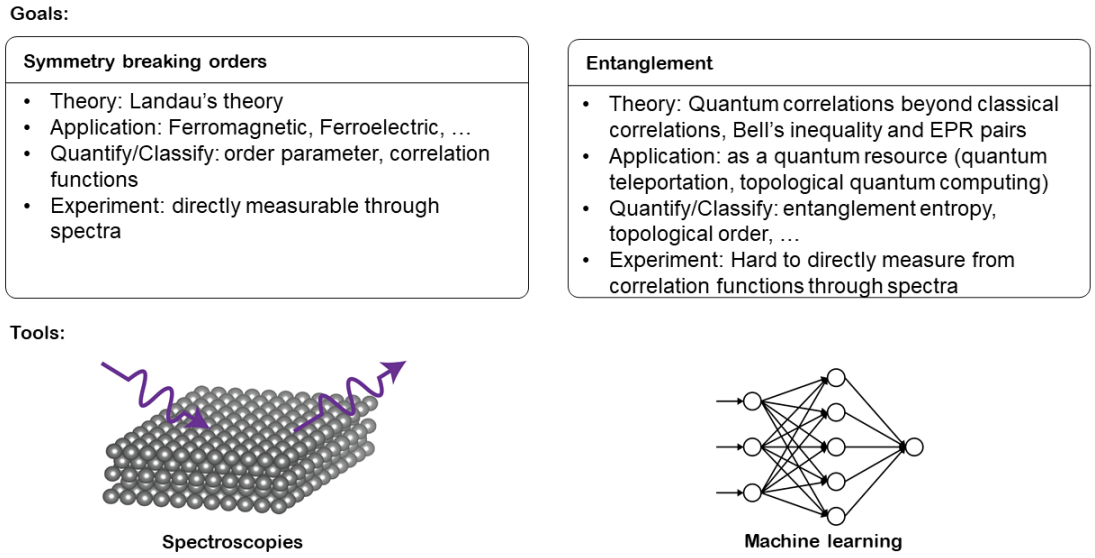

Figure 1-1: Conceptual overview: interrelationships and explanations of key concepts

Machine learning methods are particularly valuable in predicting symmetry-breaking orders of materials, even prior to experiments and extensive theoretical calculations. This capability provides an alternative approach to understanding materials, complementing traditional methods. By combining these tools—spectroscopic techniques, machine learning, and theoretical investigations—we can enhance our understanding of materials and unlock new insights into their properties and behavior.

In this chapter, I will provide an overview of the experimental spectra methods as well as delve into the machine learning methods that will be further explored throughout the remainder of the thesis. In Section. 1.1, I'll introduce the resonant inelastic scattering spectra (RIXS), emphasizing its ability to probe specific types of correlations. This discussion serves as a foundation for exploring the role of RIXS in probing entanglement in Chapter 3. Additionally, a brief overview of the scanning tunneling microscope (STM) will be presented, focusing on its capacity to capture spatial images that are valuable for investigating symmetry-breaking orders within a system, particularly when influenced by defects. In Section. 6, I'll introduce the machine learning technique, called Euclidean equivariant neural network (E3NN), which will have a significant impact on the application of machine learning in predicting material properties based on their crystal structures. This topic will be further elaborated upon in Chapter 6. To adequately address the entanglement in many-body systems, I will defer the introduction on entanglement to the subsequent Chapter 2, specifically pertaining to multipartite entanglement and indistinguishable particles, crucial for the comprehensive exploration in Chapter 3.

1.1 Spectroscopy methods in condensed matter systems

Spectroscopic methods play a vital role in probing the properties of solid-state systems, offering insights into their electronic, magnetic, and structural characteristics. With theoretical insights and the application of spectroscopic methods, it is possible to investigate classical and topologically ordered phases, as well as identify and characterize quantum entanglement. In this section, I will introduce the basic idea of some spectroscopic techniques that will support the subsequent chapters, they are resonant inelastic X-ray scattering (RIXS) and scanning tunneling microscopes (STM).

The resonant inelastic X-ray scattering (RIXS) [8] is an advanced X-ray spectroscopy technique that can probe many different collective excitations arising from

charge, spin, and orbital degrees of freedom by measuring their energy, momentum, and polarization dependence. It's achieved by tuning the incident X-ray energy to an atomic absorption edge, resulting in resonance that boosts the scattered intensity and can probe new excitations fundamentally different from non-resonant processes. It is not sensitive to sample size since the wavelength of this radiation is comparable to that of atomic spacing.

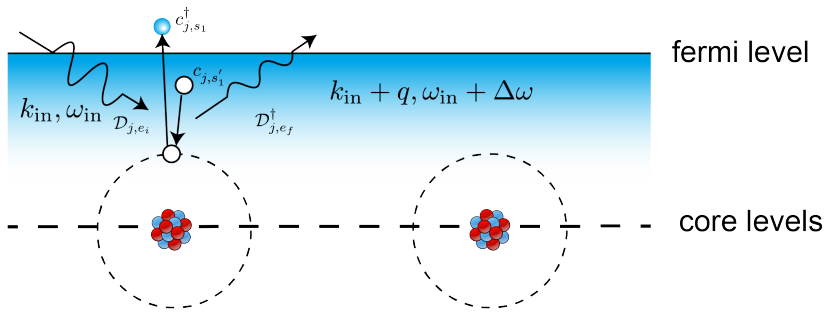

Figure 1-2: A schematic that illustrates the RIXS process.

The direct RIXS process consists of two dipole transitions, as illustrated in Fig. 1-2. In the first step, an incoming photon with momentum $\vec{k}_{\rm in}$ and frequency $\omega_{\rm in}$ excites the ground state by promoting an electron from a filled core shell into the valence band. An intermediate state undergoes an evolution determined by the system Hamiltonian over the core-hole lifetime $\frac{1}{\Gamma}$. In the second step, an electron from the valence band fills the core hole, accompanied by an outgoing photon with momentum $\mathbf{k}_{\rm in} - \mathbf{q}$ and frequency $\omega_{\rm in} - \omega$, which leaves the system in an excited final state.

The RIXS cross section is

$$I(\mathbf{q}, \omega) = \sum_f |\langle f|O_{\mathbf{q},\mathbf{e}}|i\rangle|^2 \delta(\omega + E_i - E_f) \tag{1.1}$$

where $|i\rangle$ ($|f\rangle$) is the initial (final) state of the system in the RIXS process with energy $E_i(E_f)$, the transferred momentum (energy loss) is $\mathbf{q}(\omega)$, and $\mathbf{e} = \mathbf{e}^i \cdot (\mathbf{e}^f)^\dagger$ is the tensor that describes the incoming (i) and outgoing (f) photon polarizations.

Here, the operator $O_{\mathbf{q},\mathbf{e}} = \frac{1}{\sqrt{N}} \sum_j e^{i\mathbf{q}\cdot\mathbf{r_j}} O_{j,\mathbf{e}}$ where

$$O_{j,\mathbf{e}} = D^{\dagger}_{j,\mathbf{e}_f} \frac{1}{\omega_i - \mathcal{H} + i\Gamma} D_{j,\mathbf{e}_i} \tag{1.2}$$

which describes the evolution of the system in the RIXS experiment, from the initial ground state to the excited final state, the intermediate states contain a core hole and an excited valance electron created by the dipole transition operator $\mathcal{D}_{j,\mathbf{e}_i}$. The dipole transition operator $\mathcal{D}_{m,\mathbf{e}} = (c^{\dagger}_{m,\uparrow}, c^{\dagger}_{m,\downarrow}) M_e \begin{pmatrix} p_{m,\uparrow} \\ p_{m,\downarrow} \end{pmatrix}$, where $p_{m,\sigma}(c^{\dagger}_{m.\sigma})$ is an annihilation (creation) operator in the core (valence) shell at the site index m and the spin orbital σ. The matrix $M_{\mathbf{e}}$ depends on the light polarization $\mathbf{e}$, and can be simplified into a normalized linear combination of two-by-two Pauli matrices, representing different spin channels.

The above two-level description (one core level and one valance level) is an effective model much simplified based on the realistic setup. In real experiments, there are often multiple core levels involved and the system should be described by a multi-band model instead of a 2-band model (1 valance band and 1 core band). For example, in the Cu L-edge 2p $\rightarrow$ 3d transition, there are three 2p orbitals as core levels denoted as $2p_\alpha, \alpha = x, y, z$. Actually, the multiple core orbitals combined with the spin-orbital effects are the cause of spin flip. The dipole transitions preserve the total spin, however, due to the spin-orbit coupling at multiple core levels, the pair of photon absorption and emission may flip a spin. This is derived for $2p_\alpha$ orbitals in the Supplementary Information of Ref. [10]. Here we use the effective theory model with only one core level and four spin channels, for simplicity and for generality in different X-ray edges. The four spin channels are represented by $M_{e_f} = \sigma^{0,x,y,z}$, while keeping $M_{e_i} = \sigma^0$. There is one spin-conserved channel ($M_{e_f} = \sigma^0$) and three spin-flip channels ($M_{e_f} = \sigma^{x,y,z}$).

Under the spin-flip channel with $M_{e_i} = \sigma^0, M_{e_f} = \sigma^z$, RIXS gives a good approximation to the spin excitation susceptibility usually represented by $S^z(q, \omega)$, which becomes exact at the ultra-short core-hole lifetime (UCL) limit [11]. We will discuss

this in detail in Chapter. 3.

Scanning tunneling microscopy (STM) is a powerful technique that provides not only spatially resolved information about surfaces, but also spectroscopic measurements of the electronic density of states at the atomic length scale. Thus, it is ideal for investigating local excitations and observing defect effects at the atomic scale, especially on two-dimensional materials. A schematic illustration of STM is shown in Fig. 1-3, a tip is brought close to a sample surface, and a bias voltage is applied in between, due to the quantum tunneling, electrons will be removed from or injected into the sample. The tip scans over the surface with fine control of its position, thus one acquires a spatial profile of the sample. The STM intensity is the local differential conductance $\frac{dI}{dV}$ with both spatial and energy resolution. Because the tunneling current I is proportional to the integral of the sample density of states over the range of the tip Fermi surface energy and the sample Fermi surface energy which is differed by $-eV$, the differential conductance is proportional to the local density of states (LDOS) of the single particle charged excitations at certain energy denoted as ε. The differential conductance G as a function of the applied voltage bias V reads

$$G(V) = \frac{dI}{dV} = \frac{2e^2}{h} \sum_{\mathbf{k}} A(\mathbf{k}) \rho(\mathbf{k}, V) \tag{1.3}$$

where the summation $\sum_{\mathbf{k}}$ accounts for summing over different wavevectors $\mathbf{k}$, capturing the contributions from various electronic states. The tunneling matrix element $A(\mathbf{k})$ signifies the coupling strength between the scanning tunneling microscope (STM) tip and the sample at wavevector $\mathbf{k}$. Lastly, $\rho(\mathbf{k}, V)$ represents the local density of states (LDOS) at wavevector $\mathbf{k}$ and energy eV, representing the availability of electronic states for tunneling at specific energy and position in the sample.

In this thesis, we explore the use of various spectroscopic techniques to extract information from a diverse range of quantum materials. The information obtained includes multipartite entanglement, ferroelectric and nematic orders, and charge orders. In Chapter 3, we discuss the use of resonant inelastic X-ray scattering (RIXS) to measure four-point correlations. This approach enables us to probe a more general piece of

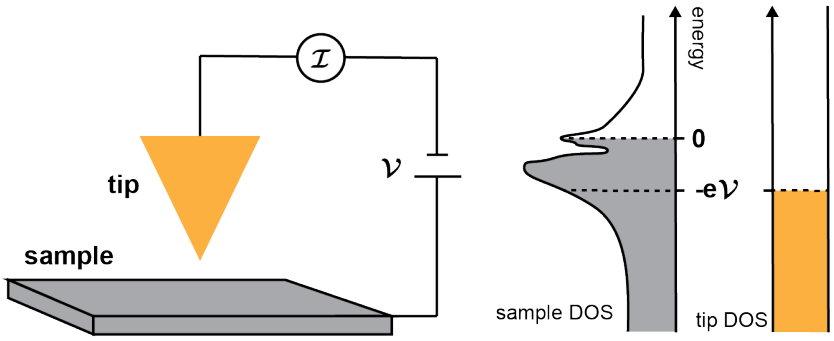

Figure 1-3: A schematic that illustrates the STM tunneling.

information applicable to any quantum material: fermion multipartite entanglement. In Chapter 4, we delve into employing scanning tunneling microscopy (STM) to probe impurity states and detect ferroelectric and nematic phases in valley quantum Hall systems. In Chapter 5, we again utilize STM to investigate various charge orders, including stripe phases, in twisted transition metal dichalcogenide (TMD) bilayers.

1.2 Machine learning applications

Machine learning has emerged as a promising tool in the field of quantum materials, with applications spanning from predicting material properties to accelerating numerical algorithms used in condensed matter theory[12].

We explore the use of symmetry-preserved graph neural networks to predict the properties of materials in Chapter 5. Graph neural networks are naturally suited for material structures, as they can represent atoms and bonds (interactions) between atoms in a straightforward manner. Information about atoms can be encoded on the nodes of the graph neural network, while interactions or bond information, such as distances, can be represented by the connections between nodes.

Any space group that describes the crystal geometric symmetries in three dimensions is a subgroup of E(3) (Euclidean group in 3 dimensions), we utilize an Euclidean equivalent neural network called E3NN[13], which preserves all geometric symmetries of the crystal structure. This approach leverages the inherent structure of the materi-

als and their symmetries to make accurate predictions of their properties and removes the need for extensive data augmentation needed to consider arbitrary translations or rotations of the input structures. The mathematical foundation of E3NN lies in the tensor field neural networks developed by Thomas and Smidt et al. [14]. The NNs perform pointwise convolutions on three-dimensional point clouds with permutation, rotation, and translation equivariances into account. Such properties make it extremely suitable for studying crystals.

Intuitively, the convolution step is implemented as:

$$f'_a = \frac{1}{\sqrt{z}} \sum_{b;|\vec{r}_{ab}|<r_{max}} f_b \otimes (h(\|\vec{r}_{ab}\|))\, Y(\vec{r}_{ab}/\|\vec{r}_{ab}\|)$$

where f'_a is the output for node a. The output is the sum of the tensor product between the input from neighborhood nodes f_b and the neural networks h depending on the distances between nodes. Y is the spherical harmonics, which serve as basis functions that enable the mapping of the relative angles to the weights of the tensor product. The prefactor $1/\sqrt{z}$ adjusts the different numbers of the neighborhoods. With such implementation, it can almost preserve complete geometric information of the input crystal structure when applied to encode materials.

1.3 Outline

As can be surmised from the broad list of topics mentioned in the previous sections of the introduction, this thesis will touch upon many aspects of measurements of quantum materials and machine learning applications. Therefore, except Chapter 2 which is an extra intro chapter for the entanglement in many-body systems and Chapter 7 is a conclusion chapter, each chapter will begin with its own introduction to a specific problem considered within it. This thesis focuses on various topics surrounding the themes of entanglement, spectroscopies, and machine learning: the experimental-driven proposals to detect multipartite entanglement using X-ray scattering spectroscopy (Chapter 3), and the prediction of symmetry breaking in two-dimensional

platforms, which are detectable via scanning tunneling microscopy (STM) (Chapters 4 and 5). Another is machine learning-assisted prediction of magnetic structures (Chapter 6).

I will begin in Chapter 2 with an introduction of entanglement in many-body systems, focusing on the multipartite entanglement and entanglement in systems of indistinguishable particles, in support of Chapter 3. In Chapter 3, I'll propose a new technique to extract high-order correlations using Resonant inelastic X-ray scattering (RIXS). I'll then define a new multipartite entanglement witness in a many-body fermion system that utilizes higher-order correlations and gives tighter boundaries than quantum Fisher information (QFI). In Chapter 4, I will discuss the impurity bound states arising near impurities in two-dimensional multivalley electronic systems under strong quantizing magnetic fields, that can be directly probed via STM spectroscopy, thus serve as local signatures for detecting the quantum hall ferroelectric and nematic order. In Chapter 5, I will move on to the charge orders at the fractional band fillings in twisted transition metal dichalcogenide (TMD) bilayers that can be and later measured in experiment via STM, the charge orders at various fractional fillings arise from the interplay of long wavelength moiré potential and long-range Coulomb interaction. In Chapter 6, I'll present a machine-learning model based on the Euclidean equivariant graph neural network (E3NN) which preserves the crystallographic symmetry, that is trained to predict magnetic orders (ferromagnetic, antiferromagnetic, and non-magnetic) and magnetic propagation vectors (zero or nonzero) with the crystal structures as input. The descriptor used has the advantage to encode general crystal structures of any space group and the model reached an accuracy of 77.8% for magnetic ordering prediction over all materials containing magnetic elements in the database Materials Project. In Chapter 7, I'll summarize and provide insights into potential future efforts.

Chapter 2

Entanglement in many-body systems

This chapter reviews the entanglement in many-body systems in supporting Chapter 3, for both distinguishable particles and identical particles, with a focus on the accessibility through spectroscopies. Among various topics, we'll include fermion multipartite entanglement and quantum Fisher information that supports the ideas in Chapter 3. A more comprehensive review on quantum entanglement can be found in Refs. [4, 15].

This chapter is structured as followings. In Sec. 2.1, we review the entanglement in systems of distinguishable particles, such as qubit/spin system, where we first introduce bipartite entanglement following Refs [16, 17, 18], then we introduce the multipartite entanglement and quantum Fisher information following Refs [19, 20, 7]. In Sec. 2.2, we initiate the discussion on entanglement in systems of indistinguishable(identical) particles[21, 22], with a specific focus on the differences between identical and distinguishable particles regarding exchange symmetry[23] and basis invariance. Furthermore, we elucidate the need for a distinct entanglement definition than the distinguishable case and introduce a classification scheme for entangled and non-entangled fermion states[24]. In Sec. 2.3, we review the efforts of identity entangled states in fermion systems, the Slater number in Refs. [21, 22] and the pairing theory in Ref. [24], this part is to be compared with the fermion multipartite entanglement witness we propose in Sec. 3. In Sec. 2.4, we formally present the definition of fermion multipartite entanglement, drawing parallels to multipartite entanglement in

spin systems, but tailored specifically to indistinguishable fermionic particles.

2.1 entanglement in systems of distinguishable particles

2.1.1 bipartite entanglement

In the spin/qubit system, there are various ways to quantify the entanglement. For bipartite systems(two-qubit systems of multi-qubit systems divided into two subsystems), people usually use the entanglement entropy as a measure of the entanglement[17], there are a full set of Rényi entropies[25], the most commonly used one is the von Neumann entropy $S(\rho_A) = -\mathrm{Tr}(\rho_A \log_2 \rho_A)$, where ρ_A is the reduced density matrix of a subsystem A obtained by tracing out the other subsystem B, $\rho_A = Tr_B \rho_{AB}$. For a bipartite system in a pure state, the entanglement entropy of both subsystems is equal, reflecting the monogamy of entanglement.

Another important concept in the study of bipartite entanglement is quantum mutual information ($I(A:B)$), which measures the total correlations between subsystems A and B, including both classical and quantum correlations. It is defined as $I(A:B) = S(\rho_A) + S(\rho_B) - S(\rho_{AB})$, where ρ_A and ρ_B are the reduced density matrices of subsystems A and B, respectively, and ρ_{AB} is the joint density matrix of the composite system. Quantum mutual information can be interpreted as the reduction in uncertainty about one subsystem when the state of the other subsystem is known. In this context, it provides valuable insights into the relationship between entanglement and correlations in bipartite quantum systems. The quantum mutual information can be applied to tripartite systems [26],

$$I(A:B:C) = S(\rho_A)+S(\rho_B)+S(\rho_C)-S(\rho_{AB})-S(\rho_{AC})-S(\rho_{BC})+S(\rho_{ABC}) \quad (2.1)$$

We will show that quantum mutual information plays a role in the definition of topological entanglement entropy.

While the above definitions have been proven useful for quantifying entanglement in few-body systems, they face some limitations when applied to many-body systems, such as large-scale solid-state systems. The major issue lies in the fact that both the entanglement entropy and the quantum mutual information depend on the chosen division of the whole system into subsystems, resulting in a quantified value that varies with this choice. Besides, the measurement of entanglement entropy is usually only possible in small/synthetic quantum systems.

In solid-state systems, an alternative definition of entanglement, known as topological entanglement entropy, has been proposed to address this concern. Dividing a large system into regions A and B with a shared boundary, the entanglement entropy S obeys the area law[27] for each region, scaling as the boundary length, if the states are ground states of local gapped quantum Hamiltonian.

$$S(\rho_A) = \alpha L - \gamma + \cdots \tag{2.2}$$

where L is the area of boundary, $\cdots$ are terms that will vanish at the thermodynamic limit, γ is called the topological entanglement entropy[17, 18]. The topological entanglement entropy carries information about the topological order of the system. In topologically trivial systems, $\gamma = 0$, while for topologically nontrivial systems, $\gamma > 0$. This quantity is invariant under smooth deformations of the system and is independent of the choice of subsystems, making it a robust indicator of topological order. There is another way to define the topological entanglement entropy in a tripartite system with regions A, B, C, the topological entanglement entropy is simply the quantum mutual information between tripartites, $\gamma = I(A : B : C)$[18].

However, the topological entanglement entropy is still not ideal when we consider its accessibility, as it necessitates global measurements over a large N system[28, 29], that are often unattainable through spectroscopic methods, which effectively measure few-point correlations that are in the region of local measurements. There is a need for an entanglement definition for many-body systems that can be probed by local measurements, such as spectroscopies.

2.1.2 multipartite entanglement and quantum Fisher information

The multipartite entanglement, on the other hand, can be witnessed by local measurements, as shown in Refs. [20, 7]. The definition of multipartite entanglement[30, 31] is that, for a pure state $|\psi\rangle$, if the state can be decomposed into

$$|\psi\rangle = \otimes_{l=1}^{p} |\psi_l\rangle \tag{2.3}$$

where $|\psi_l\rangle$ is a state with $N_l < k$ particles (qubits), then the state is called k-producible, a state that is k-producible but not $k-1$-producible is called k-particle entangled, meaning that if we decompose the state into the form where each product term can not be further separable, meaning they are genuinely entangled, then the largest genuinely entangled block are formed by k particles(qubits). Some contents also call the state as p-partite separable or p separable, when it can be decomposed into at most p product terms. In this definition, the fully separable state is 1-producible, a mixed state $\rho = \sum_i p_i |\psi^i\rangle \langle\psi^i|$ is k-particle entangled if each $|\psi^i\rangle$ is N^i-particle entangled and $\max_i N^i = k$. The multiparticle entanglement, unlike the previous definitions that can apply a continuous measure of the entanglement of the systems, is only a coarse-grained classification. An integer k is used to classify all quantum states as k-particle entangled, it doesn't require to specify subsystems. It is not the only way to classify quantum many-body states, a further classification can be achieved by means of stochastic local quantum operations and classical communication (SLOCC), a topic beyond the scope of this discussion. Interested readers are referred to relevant references for more detailed information[32, 33, 4].

In Ref .[20, 7], the quantum Fisher information (QFI) is proposed to be a witness of the multipartite entanglement. An observable W is called an entanglement witness, if for all separable states ρ_{sep} it has a non-negative mean value, $Tr[W\rho_{\text{sep}}] \geq 0$ and there exist at least one entangled state $\rho_{textent}$ such that $Tr[W\rho_{\text{ent}}] < 0$, changing the direction of inequality signs or adding constant number to both side of the equation does not affect the definition. The definition stems from the geometry: the set for all

separable states is convex, and the convex sets can be described by hyperplanes. Actually, each set of all k-producible states is also convex[20], which suggests proposing witnesses for multipartite entanglement.

QFI originates from the field of quantum metrology[34, 35, 36, 37, 38], it quantifies the maximal precision one can achieve for the parameter(phase) estimation in a quantum state. Namely, a probe state ρ transform as $\rho(\theta) = e^{-i\theta\hat{H}}\rho e^{i\theta\hat{H}}$, depending on the parameter/phase to be estimated θ and the operator $\hat{H}$. An estimator $\theta_{\text{est}}\left(\{\mu_i\}_m\right)$ depends on the results $\{\mu_i\}_m = \{\mu_1, \cdots, \mu_m\}$ of m independent repeated measurements of a positive operator valued measurement(POVM) with elements $\{\hat{E}_\mu\}_\mu$. If the estimator is unbiased, then its minimal standard deviation is limited by the so-called quantum Cramer-Rao bound,

$$\Delta\theta_{\text{est}} \geq \frac{1}{\sqrt{mF}} \geq \frac{1}{\sqrt{mF_Q}} \tag{2.4}$$

where F is the Fisher information that depends on the POVM, maximizing F over all possible POVMs leads to the quantum Fisher information F_Q. The QFI depends on the generator operator $\hat{H}$ but does not depend on the POVM $\{\hat{E}_\mu\}_\mu$.

For a mixed state $\rho = \sum_l \lambda_l \left|\psi_l\right\rangle \left\langle\psi_l\right|$, the QFI is given by

$$F_Q[\rho; \hat{H}] = 2\sum_{l,l'} \frac{(\lambda_l - \lambda_{l'})^2}{\lambda_l + \lambda_{l'}} |\left\langle\psi_l\right|\hat{H}\left|\psi_{l'}\right\rangle|^2 \tag{2.5}$$

For pure states, it reduces to $F_Q = 4(\Delta\hat{H})^2$, where $(\Delta\hat{H})^2 = \langle\hat{H}^2\rangle - \langle\hat{H}\rangle^2$ is the variance of the generator of the phase shift $\hat{H}$.

If we select the generator $\hat{H}$ as the ones in linear two-mode interferometers, so it is a summation over local operators on each particle(qubit) of the states, such as

$$\hat{H} = \frac{1}{2}\sum_{l=1}^{N} \hat{\sigma}_{\vec{n}_l}^{(l)} \tag{2.6}$$

where N is the number of qubit in the state, $\hat{\sigma}_{\vec{n}_l}^{(l)} = \vec{n}_l \cdot \vec{\sigma^{(l)}}$, $\vec{n}_l$ is a vector on the Bloch sphere. The QFI with this linear generator has three properties that allow it

to serve as a witness of multipartite entanglement. (1) QFI is convex in states, i.e. $F_Q[p\rho_1 + (1-p)\rho_2] \leq pF_Q[\rho_1] + (1-p)F_Q[\rho_2]$. (2)QFI is additive for product states, $F_Q[|\phi\rangle \otimes |chi\rangle] = F_Q[|\phi\rangle] + F_Q[|\chi\rangle]$. (3) For a k-qubit state, QFI has an upper bound k^2 that uniquely saturated by the GHZ state, $|GHZ_k\rangle = \frac{1}{\sqrt{k}}(|0\rangle^{\otimes k} + |1\rangle^{\otimes k})$. Combining three properties, there is an upper bound of QFI for any k-particle entangled state with N total particles,

$$F_Q[\rho_{k-part}; \hat{H}_{\text{lin}}] \leq sk^2 + r^2 \tag{2.7}$$

where $s = \left[\frac{N}{k}\right]$ and $r = N - sk$. Hence a violation of the bound proves $(k+1)$-particle entanglement, so it is a multipartite entanglement witness. The bounds are uniquely saturated by a product of s GHZ states of k particles and another GHZ states of r particles.

2.2 entanglement in systems of indistinguishable particles

Entanglement is very well understood for distinguishable particles, however, in a system of indistinguishable particles like fermions or bosons, the definition of entanglement and separability becomes tricky. One can find discussions about the different definitions of entanglement between identical particles in Refs. [39, 40, 41, 21, 22, 24], we briefly summarize the basic ideas below.

2.2.1 exchange symmetry and Slater determinant

We follow the idea in Ref. [21] to discuss the consequence of exchange symmetry in identical particles. Considering a two-particle state where Alice has one particle and Bob the other, in the mode-occupation, or Fock, representation, the state is $|1,1\rangle$, which appears unentangled. If the two particles are distinguishable, we can write the wavefunction as $\psi_A(x)\psi_B(y)$, which also has a product state form. However, since the two particles are identical and indistinguishable, exchanging the two particles leave the state unchanged ignoring a phase factor, the wave function must be symmetrized

as

$$\psi_A(x)\psi_B(y) \pm \psi_A(y)\psi_B(x) \tag{2.8}$$

for bosons and fermions, respectively. This has the appearance of an entangled state. The same story happens all the time in many-body fermion and boson states, where there could be ambiguity on whether the state is entangled or separable, and the entanglement could merely come from the indistinguishability of particles. Taking the fermion Fock state as an example, its wavefunction can be written as a Slater determinant,

$$\Psi(\vec{x_1}, \vec{x_2}, \cdots, \vec{x_n}) = \frac{1}{\sqrt{N!}} \begin{vmatrix} \chi_1(\vec{x_1}) & \chi_2(\vec{x_2}) & \cdots & \chi_N(\vec{x_1}) \\ \chi_1(\vec{x_2}) & \chi_2(\vec{x_2}) & \cdots & \chi_N(\vec{x_2}) \\ \vdots & \vdots & \ddots & \vdots \\ \chi_1(\vec{x_N}) & \chi_2(\vec{x_N}) & \cdots & \chi_N(\vec{x_N}) \end{vmatrix} \tag{2.9}$$

There have been some debates about whether such a state is entangled or not, some literature view this entanglement purely from indistinguishability and the exchange relation of particles as a failure of the mathematical formalism [42, 39], and count them as unuseful or unphysical entanglement. Here we adopt this viewpoint, the naive reason is that all fermion/boson states will be entangled if oppositely, and we need the ability to distinguish entangled and separable states in a system of indistinguishable particles. More formally we can argue that the entanglement from indistinguishable particle exchange is not useful for practical propose. Considering a two-particle state well separated in two locations, such that their wavefunction $\psi_A(x)$ and $\psi_B(x)$ has only vanishingly small overlap, then all the exchange correlations of physically meaningful operators will tend to zero, as shown in the Hatree-Fock theory. Therefore, for condensed matter systems where the single-particle wavefunctions are essentially centered around locations being sufficiently apart from each other, or the particles are separated by a sufficiently large energy barrier, the entanglement from exchange statistics does not have any physical effect.

The Slater determinant is frequently used as an approximation to describe the

wave function of multi-fermionic systems. It fulfills the anti-symmetry requirements and, consequently, the Pauli principle by changing its sign when two electrons are exchanged. In reality, almost none of the condensed matter systems can precisely match the Slater determinant. In fact, most strongly correlated systems deviate significantly from it. This is due to two main reasons: Firstly, finding a set of single-particle orthogonal orbitals for a many-body fermionic state is challenging since there can be overlapping between different orbitals, regardless of the chosen orbital wavefunctions, for example, in non-Fermi liquids such an orthogonal basis does not exist. Secondly, even with a set of single-particle orthogonal (non-overlapping) basis, which allows us to utilize the second quantization formalism, the state can still be entangled in the second quantization form, as discussed in Section 2.2.2. Two examples with negligible overlapping between single-particle orbitals are Mott insulators, where electrons are nearly localized at atomic sites due to strong Coulomb interactions, and metals with weak Coulomb interactions that can be described by Fermi liquid theory, which exhibit properties similar to those of an ideal Fermi gas (non-interacting fermions). As discussed earlier, we consider the Slater determinant state to be non-entangled. Therefore, both of these distinct examples are non-entangled in this sense.

The failure of Slater determinant approximation also suggests that the energy-filling picture in conventional condensed matter physics fails to explain many strongly correlated quantum states. The mean-field approximation and Fermi liquid theory fail accordingly. If a measure could be established to quantify the extent of error in the Slater determinant approximation for a particular state, it might likely serve as an indicator of the state's level of strong correlation. One of these relevant measures will be explored in Chapter 3.

2.2.2 single-particle orbital basis invariance

Having excluded the unphysical entanglement from exchange symmetry, here we analyze the useful entanglement in the second-quantization form, because the second-quantization naturally avoids the difficulty of representing an antisymmetric wavefunction as a product state in the first-quantization form. The antisymmetric Fock

state in Eq. 2.9 can be represented in the second-quantization form as

$$|\Psi\rangle = c_1^\dagger c_2^\dagger \cdots c_N^\dagger |0\rangle \tag{2.10}$$

where $c_i^\dagger$ is the creation operator that satisfied the canonical anticommutation relations, $\{c_i^\dagger, c_j^\dagger\} = 0, \{c_i, c_j^\dagger\} = \delta_{i,j}$. We want to view this state as unentangled since it has a separate product state form. Besides, for all operators O_1, O_2 locally act on $1, 2$ modes, we have

$$\langle\Psi|O_1 \otimes O_2|\Psi\rangle = \langle\Psi|O_1|\Psi\rangle \langle\Psi|O_2|\Psi\rangle \tag{2.11}$$

this is another view to distinguish entangled states and separable states, by showing that for selected subsystems, two-point correlations of all local operators can be factorized as above, such that the subsystems can be individually addressed.

Up to here, it seems all good, we have found the definition of the product state (unentangled state), however, there are linear transformations of the fermionic operators which preserve the canonical anticommutation relations and the total particle numbers, called the passive canonical transformations, and they are of the form $c_i^\dagger \mapsto c_i'^\dagger = \sum_j U_{ji} c_j^\dagger$, where U is unitary on the single-particle Hilbert space $\mathcal{H}$. The above definitions, either the product state form or the factorization of two-point correlations, depend on the choice of basis/subsystems. Naively, a Fermi sea state where electrons fill in the energy bands without Coulomb interaction is a product state on the momentum space basis, but it is not in the product state form on the real space basis. In Ref. [24], a state is defined as a product/separable/unentangled state, if there exists a basis change of the fermion operators (a passive transformation) $c_i^\dagger \mapsto c_i'^\dagger = \sum_j U_{ji} c_j^\dagger$ such that

$$|\Psi\rangle = c_1'^\dagger c_2'^\dagger \cdots c_N'^\dagger |0\rangle \tag{2.12}$$

Such a state also fulfills the factorization relation of the two-point correlations between any two modes in any basis(transformation). All other states are called entangled, now the definition of entanglement becomes basis-invariant.

A mixed state ρ_s is called unentangled/separable, if it can be written as the convex combination of product states, i.e.

$$\rho_s = \sum_{p=1}^{K} \lambda_p \rho_p \tag{2.13}$$

where $\rho_p = |\psi_p\rangle \langle\psi_p|$ are product states, $\sum_{p=1}^{K} \lambda_p = 1, \lambda_p \leq 1$.

2.3 Entanglement witnesses in fermionic systems

Based on this definition, there have been some efforts in finding an entanglement witness for the entangled states in the fermionic system. To make a comparison with the multiparticle witness in a fermionic system defined in Sec. 3, here I briefly review two types of witnesses, the Slater number/rank or concurrence[21, 22], and the pairing witness[24].

In the two-particle system, we can always write the state as a sum of elementary Slater determinants where each single-particle basis state occurs at most in one term. The general state vector is

$$\begin{aligned} |\omega\rangle &= \sum_{i,j=1}^{N} \omega_{ij} c_i^\dagger c_j^\dagger |0\rangle \\ tr(\omega^* \omega) &= -\frac{1}{2} \end{aligned} \tag{2.14}$$

where $|0\rangle$ is the vacuum state, ω_{ij} is an antisymmetriy matrix fulfills the above normalization condition. Under a unitary transformation of the single-particle space, $c_i^\dagger \mapsto \mathcal{U} c_i^\dagger \mathcal{U}^\dagger = U_{ji} c_j^\dagger$, there exist a transformation U for any antisymmetric ω such that

$$\omega \mapsto U \omega U^T = \text{diag}\left[Z_1, \cdots, Z_r, Z_0\right] \tag{2.15}$$

where $Z_i = \begin{bmatrix} 0 & z_i/2 \\ -z_i/2 & 0 \end{bmatrix}$ and $z_i > 0, \sum_i z_i^2 = 1$, and Z_0 is the $(N-2r)\times(N-2r)$ null matrix. This process is called Slater decomposition, any two-particle fermion state $|\omega\rangle$

can be written as a sum of elementary Slater determinants where each single-particle basis state occurs at most in one term, this is analogous to the Schmidt decomposition in bipartite qubit systems.

The Slater number/rank is defined as the minimum number r of the non-vanishing basis of elementary Slater determinants. If the Slater number is 1, meaning the state can be written as $|\omega\rangle = c_i^\dagger c_j^\dagger |0\rangle$ which is a fully separate product state. We conclude that the state is unentangled if and only if the Slater number is 1. The Slater number coalign with the definition above of entangled/non-entangled states. The concurrence $\mathcal{C}(|\omega\rangle)$ is an entanglement measure and defined as

$$\mathcal{C}(|\omega\rangle) = |\sum_{i,j,k,l} \epsilon^{ijkl}\omega_{ij}\omega_{kl}|. \tag{2.16}$$

It ranges from zero for non-entangled states to one for fully entangled states, which are colinear with their dual states.

The Slater decomposition, however, does not apply to k-particle fermion states for $k > 2$, a sum of elementary Slater determinants does not always exist for multi-particle states, which can be understood by counting the dimensions, we will discuss this in more details in Sec. 3. As a result, the concurrence does not apply directly to multiparticle fermion states. For a general k-particle fermion state, $|\omega\rangle = \sum \omega_{i_1,i_2,\cdots,i_k} c_{i_1}^\dagger \cdots c_{j_k}^\dagger |0\rangle$, It is possible to define alternative measure which is zero if and only if the state is non-entangled(has Slater number 1), however, such a measure will be highly complicated and involve the matrix elements $\omega_{i_1,i_2,\cdots,i_k}$, which are only accessible through high-order correlations where the number of fermion operators is in the order of k.

Naively, if we can access all correlations of a N-particle system, we already have all the information to reconstruct the state. Experimentally, most spectroscopic techniques can only measure correlations whose operators are the product of at most two creation and two annihilation operators, including correlations like $\langle c_i c_j^\dagger \rangle$, $\langle c_i c_j c_k^\dagger c_l^\dagger \rangle$, we call these kinds of correlations as one-particle and two-particle correlations. The practical question is whether we can construct entanglement witnesses just with one-

particle and two-particle correlations. This question is discussed in Ref. [24], where it refers to the states whose one-particle and two-particle correlations can not be reproduced by any separable state as paired states. Paired states are fermionic states exhibiting non-trivial quantum correlations up the two-particle level, however, it is not equivalent to entanglement, a short answer is that there exist states that are entangled according to the Slater rank concept, but not paired. For example, the non-entangled state $\rho = \frac{1}{2}|\phi\rangle\langle\phi| + \frac{1}{2}|\chi\rangle\langle\chi|$, where $|\phi\rangle = c_1^\dagger c_2^\dagger c_3^\dagger c_4^\dagger |0\rangle, |\chi\rangle = c_5^\dagger c_6^\dagger c_7^\dagger c_8^\dagger |0\rangle$, has all the one- and two-particle expectations the same with the entangled state $|\Psi\rangle = \frac{1}{\sqrt{2}}|\phi\rangle + \frac{1}{\sqrt{2}}|\chi\rangle$, so they are indistinguishable at the two-particle correlation level.

2.4 The Multipartite Entanglement

Among the entangled states in multiparticle fermionic systems, we want to further compare whether one state is more entangled than another, and consider the indistinguishability and basis-invariant as discussed above. A natural generation is to adopt a similar concept of multipartite entanglement in the spin systems and apply it to the fermionic system. The definition is based on the previous attempt in Ref. [43], and accommodates the basis-invariant property inspired by Ref. [44]. We will first elaborate the definition, and some discussions follow behind.

Consider a set of fermionic modes M, with associated creation and annihilation operators $c_m^\dagger$ and c_m, labeled by $m \in M$. A k partition of the system is defined as a partition $M = M_1 \cup M_2 \cup \cdots \cup M_p$. A pure fermionic state $|\psi\rangle$ defined on the set of modes M with conserved particle number N is k particle entangled if there exist a unitary transformation $c_k \mapsto c'_k$ such that it can be decomposed as

$$|\psi_{\text{k-particle}}\rangle = C_1^* C_2^* \cdots C_p^* |0\rangle \tag{2.17}$$

where the operator C_j^* is restricted to act on M_j, and there are n_j particles created by C_j^*, $\sum_j n_j = N, max(n_1, n_2, \cdots, n_p) = k$. The state $C_j^*|0\rangle$ is a genuinely multipartite

entangled(GME) state, meaning it cannot be written as a product in any possible bipartition of the state for any single-particle fermion basis we use. We thus call each C_j^* a GME block with modes M_j and particle number n_j. A GME block with two fermions is easy to describe, if performing Slater decomposition on C_j^*, the result is full rank, i.a. the rank number is equal to $|M_j|/2$. And we can divide modes in M_j as subgroups $M_j^1, M_j^2, \cdots, M_j^{|M_j|/2}$, each contains 2 modes. The C_j^* operator with 2 fermions in the Slater decomposition basis can be written as

$$C_j^* = \sum_{i=1}^{|M_j|/2} \phi_i^j \prod_{M_j^i=\{m_1,m_2\}} c_{m_1}^\dagger c_{m_2}^\dagger \tag{2.18}$$

where $\phi_i^j > 0$ and $\sum_{i=1}^{|M_j|/2} (\phi_i^j)^2 = 1, M_j^{i_1} \cap M_j^{i_2} = \emptyset, i_1 \neq i_2$.

Following the definition of product/entangled fermionic states, we naturally inherit the second-quantization form and allow a passive transformation, so it excludes the unphysical entanglement from antisymmetry exchange of indistinguishable fermions, while also being basis-invariant. The definition adopts a similar idea of multipartite entanglement in the qubit(spin) system, while the particles here refer to fermionic particles instead of qubits.

Chapter 3

Entanglement witness and multi-point correlations in resonant inelastic X-Ray scattering

The characterization of entanglement in quantum materials is crucial for the development of next-generation quantum technologies, yet defining and measuring a quantifiable figure of merit for entanglement in a many-body quantum system is theoretically and experimentally challenging. The presence of entanglement in fermionic systems can be diagnosed by extracting entanglement witnesses from spectroscopies, which are directly related to the spin dynamic structure factors of the system. With cross-polarization, RIXS(Resonant inelastic X-ray scattering) approximates the spin and charge dynamic structure factors, which becomes exact at the ultra-short core-hole lifetime limit. Here, we propose a new RIXS technique that can extract higher-order correlations beyond the scope of the spin and charge structure factors. We verify our method using computational RIXS spectra, and theoretically propose a new entanglement witness of fermion systems. Using the extended Hubbard model and sampled random states as examples, we show the entanglement witness can quantify the multipartite entanglement in different phase regions.

3.1 introduction

Quantum materials are essential components in the development of advanced technologies, including magnetic-field sensors, energy-related technologies, and quantum computers. In particular, the search for highly-entangled quantum materials is crucial, because entanglement is a resource in quantum information applications[4]. A key step towards finding and fabricating highly-entangled materials is to develop experimental and theoretical methods to characterize entanglement. The concept of multipartite (multiparticle) entanglement [45] has been introduced for the purpose of characterizing entangled states in large-scale solid-state systems. We can coarse-grid classify [32, 46, 30, 31, 47, 48] multipartite entanglement by an integer number k and name it k-partite entanglement or entanglement depth k, this apply generally to any quantum state. While other descriptions of entanglement in a large-scale system like the topological entanglement entropy are usually only accessible through global measurements [18, 49, 50, 27], studies have shown that a witness of multipartite entanglement can be measured through dynamic susceptibilities [7], which are simply local measurements achievable via many spectroscopic techniques.

The experimental methods of probing entanglement have been developed mostly in two scenarios, for few-body quantum information setups, and for many-body systems like large-scale solid states. The former usually requires creating multiple copies of quantum states and measuring the same operator repeatedly to obtain its statistics, like in quantum metrology [34, 51]. It is hard to prepare or copy particular states in large-scale solid-state systems, and single local measurement usually does not carry enough information, consequently, most information is measured through spectroscopies, including X-ray, neutron, and photoemission spectroscopy. The typical procedure is to define an entanglement witness that can be derived from the spectra, such as the quantum Fisher information (QFI). The QFI is a concept originating from the quantum metrology [52, 36, 35, 38, 34, 45], it is later used as an entanglement witness for multipartite entanglement [20], and measurable through spectroscopies for a direct relation between the QFI and dynamic susceptibility [7].

Both the multipartite entanglement and the QFI as a witness are mostly well-studied on the spin basis. To apply them to general fermionic systems, an extension for multiparticle entanglement in systems consisting of indistinguishable particles is required, and a new entanglement witness that is related to the measurable spectra has to be defined accordingly.

Among different spectral techniques, the resonant inelastic X-ray scattering (RIXS) [8] is an advanced X-ray spectroscopy technique that can probe many different collective excitations arising from charge, spin, and orbital degrees of freedom by measuring their energy, momentum, and polarization dependence, and is not sensitive to sample size. With cross polarization resolution, RIXS gives a good approximation to the spin excitation susceptibility usually represented by $S(q, \omega)$, which becomes exact at the ultra-short core-hole lifetime (UCL) limit [11]. The capability of measuring spin susceptibility makes RIXS a suitable spectroscopy technique for measuring QFI [9]. However, since RIXS is a high-order process involving the intermediate core-hole state and can measure correlations that involve four fermion operators in the valence band, and it is momentum and polarization-resolved, it has the potential to go beyond just the spin susceptibility, i.e. the spin-spin correlations. We will show that RIXS with high precision can extract even more information from the target materials, and we can relate it to a new multipartite entanglement witness which is more general than the QFI.

In this chapter, we consider the role of the core-hole mobility in the probe of multipartite entanglement of valence electrons. We found that when the dispersion of the core level is considered, the 4-point correlations can be directly read from the RIXS spectra, and the connected part of the correlations can be derived from the difference between the RIXS and ARPES spectra. The incident-momentum-dependence in RIXS, which was usually ignored in previous studies, plays a crucial role to extract the multipoint correlations. The later sections focus on defining a multiparticle entanglement witness based on the connected four-point correlations, and examine the witness in 1D extended Hubbard model and uniformly sampled states in certain subspaces.

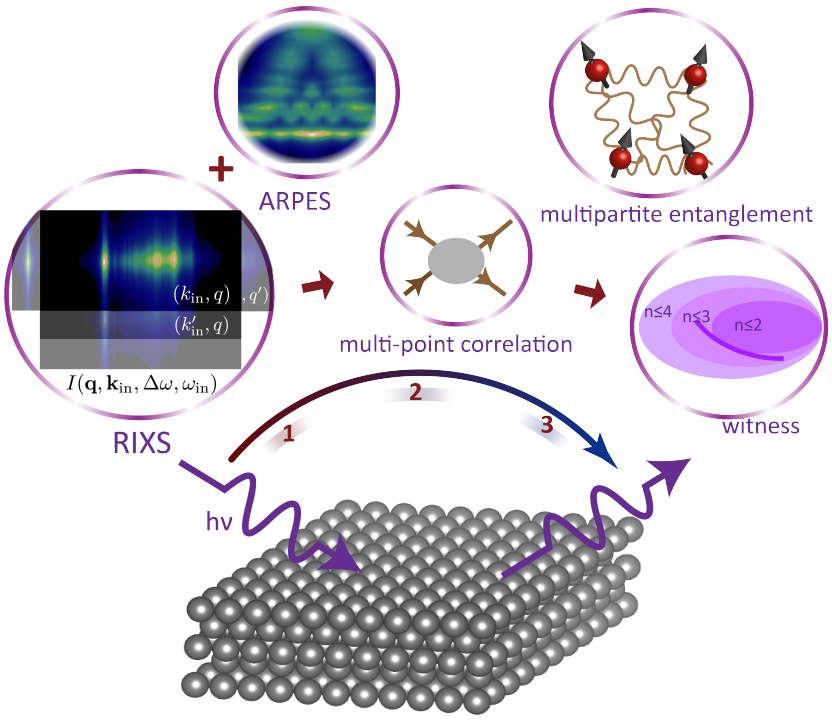

Figure 3-1: **Probing multiparticle fermion entanglement through RIXS and ARPES.** The connected parts of four-point correlations are derived from the difference between RIXS and ARPES spectra. We propose fermion entanglement witnesses based on the correlations that can detect multiparticle entanglement.

3.2 Four-point correlations from RIXS spectra

3.2.1 Expansion of the scattering cross section

If the core hole created by the incoming photon can hop to a nearby site, the RIXS intensity contains a small expansion originating from the mobile core hole, that is related to four-mode correlations. This expansion term can be separated from the rest by considering its dependence on the incoming photon momentum, which is rarely used in RIXS spectra analysis before.

The cross section of RIXS is evaluated by the Kramers-Heisenberg formula,

$$I\left(k_{\rm in}, q, \omega_{\rm in}, \Delta\omega\right) = \sum_{\rm f} \left|\langle\Psi|{\rm f}\rangle\right|^2 \delta\left(E_f - E_0 - \Delta\omega\right). \tag{3.1}$$

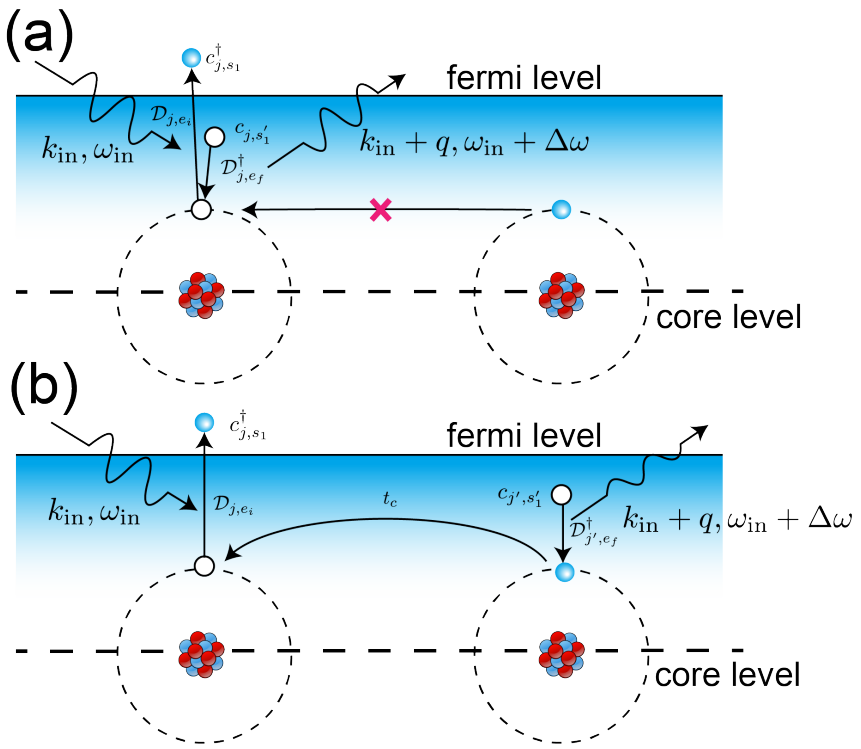

Figure 3-2: **An illustration of extracting four-point correlations from RIXS spectra.** (a) The RIXS spectra at each (k_{in}, q) plotted over incoming photon frequency ω_{in} and frequency difference $\Delta\omega$. (b) After a double integration over both frequencies, an integrated 2D RIXS intensity map over incoming photon momentum k_{in} and the momentum change q is obtained. By summing over the two momenta and considering a phase factor, we finally derive (c) the four-point correlations with i, j, k, and l each referring to a different index in the real space. (d) The mechanism of RIXS is when a higher orbital serves as a core level and allows core-hole mobility. The corresponding RIXS is k_{in}-dependent and allows the extracting of four-point correlations with all different real space indices.

The intermediate state is given by

$$|\Psi\rangle = \frac{1}{N}\sum_{m_1,m_2} e^{ik_{\text{in}}\cdot r_{m_1}} e^{-i(k_{\text{in}}+q)\cdot r_{m_2}} \times \mathcal{D}^{\dagger}_{m_1,e_f}\frac{1}{\Delta-\mathcal{H}}\mathcal{D}_{m_2,e_i}|\Psi_0\rangle \tag{3.2}$$

where $\Delta = E_0+\omega_{\text{in}}+i\Gamma$, $|\Psi_0\rangle = |\Psi_0^v\rangle\otimes|\Psi_0^c\rangle$ is the initial state and can be decomposed into the initial state of valence band and core level, the core level initial state is fully filled, and N is the system size. If there is no core-hole hopping term in Hamiltonian $\mathcal{H}$, all terms with $m_1 \neq m_2$ disappear, and we restore the original intermediate

state with an immobile core-hole. The dipole operator $\mathcal{D}_{m,e} = (c^\dagger_{m,\uparrow}, c^\dagger_{m,\downarrow}) M_e \begin{pmatrix} p_{m,\uparrow} \\ p_{m,\downarrow} \end{pmatrix}$ describes the excitation from initial to intermediate state, $c^\dagger_{m.\sigma}$ is creation operator in valence band, $p_{m,\sigma}$ is annihilation operator in core level. With the presence of strong spin-orbit coupling at core-level, and when multiple core-level orbitals are involved in the transition, the RIXS spectra can have contributions from both the spin-conserved (SC) and three non-spin-conserved (NSC) channels, represented by different dipole operator and controlled by the polarization of incoming and outgoing photons, the matrix M_e depends on light polarization e. The M_e matrix and $p_{m,\sigma}$ operator here use a basis after diagonalizing multiple core-level orbits, so effectively we only consider a single core-level orbit. A detailed derivation is shown in Ref. [10]. In the following, we fix the incoming photon polarization $M_{e_i} = \sigma^0$, the SC channel corresponds to $M_{e_f} = \sigma^0$, and the three NSC channels correspond to $M_{e_f} = \sigma^{1,2,3}$, we denote M_{e_f} as σ^α, $\alpha = 0, 1, 2, 3$ in the following content.

For a general case, the Hamiltonian $\mathcal{H} = \mathcal{H}_0 + \mathcal{H}_c$, where $\mathcal{H}_0$ is the valence band Hamiltonian, including the interaction between core-hole and valence band electron which is usually treated as a local core-hole potential with strength U_c, $\mathcal{H}_c$ is the core level Hamiltonian that describes hopping between core sites. The hopping amplitude t is small, so $\mathcal{H}_c$ can be treated as a perturbation. Taking the first order perturbation, the eigenenergies of $\mathcal{H}$ are $E_N \simeq E_N^{(0)} + E_N^{(1)}$, with $\{|N\rangle\}$ as its eigenstates. Performing the following expansion in the intermediate state, keep only the first order of $E_N^{(1)}$

$$\frac{1}{\Delta - \mathcal{H}} \simeq \sum_N |N\rangle \left(\frac{1}{\Delta - E_N^{(0)}} + \frac{E_N^{(1)}}{\left(\Delta - E_N^{(0)}\right)^2} \right) \langle N| \tag{3.3}$$

The term proportional to $E_N^{(1)}$ is our focus, it is a small perturbation, but we can distinguish it from the leading order because they have different incoming momentum k_{in} dependence. To show this relation explicitly, let us assume a specific form of the

core-hole Hamiltonian $\mathcal{H}_c$

$$\mathcal{H}_c = -t \sum_{i,\sigma} \left(p^\dagger_{i,\sigma} p_{i+1,\sigma} + \text{h.c.} \right). \tag{3.4}$$

The eigenstates with single core-hole are $|k,\sigma\rangle = \frac{1}{\sqrt{N}} \sum_i e^{ikr_i} p_{i,\sigma} |\Psi^c_0\rangle$ with eigenenergies $t\cos(ka)$, and $\sum_N |N\rangle E^{(1)}_N \langle N| = \sum_{k,\sigma} |k,\sigma\rangle t\cos(ka) \langle k,\sigma|$, where a is the distance between nearest sites. Under this assumption and the ultrashort core-hole lifetime approximation, we can set $\omega_{\text{in}} = \omega^{peak}_{\text{in}}$ at the X-ray edge, integrate the RIXS spectra over $\Delta\omega$, and use the explicit form of $\mathcal{D}_{m,e}$ to derive it into correlation functions that only involve the operators in valence band (details in Appendix)

$$\begin{aligned} I^\alpha(k_{\text{in}},k_s) &= \int \omega_{\text{in}} \int d\Delta\omega \; I^\alpha(k_{\text{in}}, k_s, \omega_{\text{in}}, \Delta\omega) \\ &\simeq \frac{1}{N^2} \sum_{m_1,m_3} e^{iq\left(r_{m_1} - r_{m_3}\right)} \Bigg[\frac{1}{\Gamma^2} I^\alpha_{\{0,0\}} + \frac{t^2}{4\Gamma^4} \times \\ &\quad \Big(e^{i(2k_{\text{in}}+q)\cdot a} I^\alpha_{\{1,1\}} + e^{iqa} I^\alpha_{\{1,-1\}} + \\ &\quad e^{-iqa} I^\alpha_{\{-1,1\}} + e^{-i(q+2k_{\text{in}})a} I^\alpha_{\{-1,-1\}} \Big) \Bigg] \end{aligned} \tag{3.5}$$

$$I^\alpha_{\{x,y\}} = \langle \Psi^v_0 | \, \mathbf{c_{m_1}} \sigma^\alpha \mathbf{c^\dagger_{m_1+x}} \mathbf{c_{m_3}} \sigma^\alpha \mathbf{c^\dagger_{m_3+y}} \, |\Psi^v_0\rangle$$

where $q = k_{\text{in}} - k_s$ is the momentum difference between incoming and outgoing photon, $\mathbf{c_m} = (c_{m,\uparrow}, c_{m,\downarrow})$, $\alpha = 0,1,2,3$ correspond to the SC channel and three NSC channels. The ultra-short core-hole lifetime condition is used for an approximation to achieve the final result.

From Eq. 3.5, $I^\alpha_{\{0,0\}}$ is a correlation including only two sites, the rest $I^\alpha_{\{x,y\}}$ are four-site correlation, we can target $I^\alpha_{\{1,1\}}$ or $I^\alpha_{\{-1,-1\}}$ by summing over both q and k_{in},

with proper phase factor added

$$
\begin{aligned}
I^{\alpha} &= \frac{4\Gamma^4}{t^2}\sum_{q} e^{iq(r_c-a)}\sum_{k_{\rm in}} e^{-i2k_{\rm in}a} I^{\alpha}(k_{\rm in},k_s) \\
&= \frac{1}{N}\sum_{m_1} \langle \Psi_0^v|\, \mathbf{c_{m_1}}\sigma^{\alpha}\mathbf{c^{\dagger}_{m_1+1}}\mathbf{c_{m_1+c}}\sigma^{\alpha}\mathbf{c^{\dagger}_{m_1+c+1}}\,|\Psi_0^v\rangle \\
&= \langle \Psi_0^v|\, \mathbf{c_{m}}\sigma^{\alpha}\mathbf{c^{\dagger}_{m+1}}\mathbf{c_{m+c}}\sigma^{\alpha}\mathbf{c^{\dagger}_{m+c+1}}\,|\Psi_0^v\rangle
\end{aligned}
\tag{3.6}
$$

where N is the total number of sites. In the last line of Eq. 3.6, we assume the Hamiltonian has translational symmetry, so the correlation functions only depend on the spatial difference.

We can not, however, target $I^{\alpha}_{\{1,-1\}}$ or $I^{\alpha}_{\{-1,1\}}$, because

$$
\begin{aligned}
&\sum_{q} e^{iqr_c}\sum_{k_{\rm in}} I(k_{\rm in},k_s) = \\
&\quad \sum_{m_1}\frac{1}{\Gamma^2}\langle \Psi_0^v|\, \mathbf{c_{m_1}}\sigma^{\alpha}\mathbf{c^{\dagger}_{m_1}}\mathbf{c_{m_1+c}}\sigma^{\alpha}\mathbf{c^{\dagger}_{m_1+c}}\,|\Psi_0^v\rangle \\
&\quad + \frac{t^2}{4\Gamma^4}\Big(\langle \Psi_0^v|\, \mathbf{c_{m_1}}\sigma^{\alpha}\mathbf{c^{\dagger}_{m_1+1}}\mathbf{c_{m_1+c+1}}\sigma^{\alpha}\mathbf{c^{\dagger}_{m_1+c}}\,|\Psi_0^v\rangle \\
&\quad + \langle \Psi_0^v|\, \mathbf{c_{m_1}}\sigma^{\alpha}\mathbf{c^{\dagger}_{m_1-1}}\mathbf{c_{m_1+c-1}}\sigma^{\alpha}\mathbf{c^{\dagger}_{m_1+c}}\,|\Psi_0^v\rangle \Big).
\end{aligned}
\tag{3.7}
$$

$I_{\{0,0\}}$, $I_{\{1,-1\}}$, $I_{\{-1,1\}}$ are inseparable because they all have no dependence with $k_{\rm in}$, however, by tuning Γ, we can distinguish the first order part from the rest.

The ultrashort core-hole lifetime approximation plays an important role in connecting the RIXS spectra with correlation functions as shown in Eq. 3.5, where it implies $\Gamma \gg E_{N_1} - E_{N_2}$ for any low energy levels E_N of the valence band Hamiltonian. Numerically, we can fix it by only calculating the second order expansion $I_{\{1,1\}}$ as needed.

3.2.2 Connected two-particle correlations from RIXS and ARPES

If the Hamiltonian of the valence band $\mathcal{H}_0$ has the time-reversal symmetry, the correlations of eigenstates or thermal states of $\mathcal{H}_0$ fulfill $\langle c_{i\uparrow}c^{\dagger}_{j\uparrow}c_{k\uparrow}c^{\dagger}_{l\uparrow}\rangle = \langle c_{i\downarrow}c^{\dagger}_{j\downarrow}c_{k\downarrow}c^{\dagger}_{l\downarrow}\rangle$, $\langle c_{i\uparrow}c^{\dagger}_{j\downarrow}c_{k\uparrow}c^{\dagger}_{l\downarrow}\rangle = \langle c_{i\downarrow}c^{\dagger}_{j\uparrow}c_{k\downarrow}c^{\dagger}_{l\uparrow}\rangle$ and $\langle c_{i\uparrow}c^{\dagger}_{j\downarrow}c_{k\downarrow}c^{\dagger}_{l\uparrow}\rangle = \langle c_{i\downarrow}c^{\dagger}_{j\uparrow}c_{k\uparrow}c^{\dagger}_{l\downarrow}\rangle$. In addition, if the

Hamiltonian has the translational symmetry, $\sum_{m=1}^{N} \langle c_{m+a,\sigma_a} c^\dagger_{m+b,\sigma_b} c_{m+c,\sigma_c} c^\dagger_{m+d,\sigma_d} \rangle = N \langle c_{n+a,\sigma_a} c^\dagger_{n+b,\sigma_b} c_{n+c,\sigma_c} c^\dagger_{n+d,\sigma_d} \rangle$ for any n. Combining the four fundamental RIXS channels (one SC I^0 and three NSC I^1, I^2, I^3), we can derive all four-point correlations in the form of $\langle c_{m_1,\sigma_1} c^\dagger_{m_1+x,\sigma_2} c_{m_1+c,\sigma_3} c^\dagger_{m_1+c+1,\sigma_4} \rangle$, short note as $I(\sigma_1, \sigma_2, \sigma_3, \sigma_4)$

$$
\begin{aligned}
I(\uparrow,\uparrow,\downarrow,\downarrow) = I(\downarrow,\downarrow,\uparrow,\uparrow) &= \frac{I^0 - I^3}{4} \\
I(\uparrow,\uparrow,\uparrow,\uparrow) = I(\downarrow,\downarrow,\downarrow,\downarrow) &= \frac{I^0 + I^3}{4} \\
I(\uparrow,\downarrow,\uparrow,\downarrow) = I(\downarrow,\uparrow,\downarrow,\uparrow) &= \frac{I^1 - I^2}{4} \\
I(\uparrow,\downarrow,\downarrow,\uparrow) = I(\downarrow,\uparrow,\uparrow,\downarrow) &= \frac{I^1 + I^2}{4}.
\end{aligned}
\tag{3.8}
$$

In Fig. 3-3 (a), a comparison of the exact correlations and the correlations calculated from RIXS spectra is shown. The model is an extended Hubbard model with the Hamiltonian in Eq. A.21, the RIXS intensity is calculated on a two-band model with both the core band and the valance band. The comparison shows that RIXS fits exact correlations very well at an ultra-short core-hole lifetime when $\Gamma = 10t$. We compare the results for $\Gamma = 1$ and 10 in Fig. 3-3 (b,c,d).

For convenience purposes, we would like to take the correlation in the anti-normal ordering, i.e. $\langle ccc^\dagger c^\dagger \rangle$. This can be achieved by exchanging two operators. In addition, we are interested in the connected part of the correlation, like $\langle c_i c_j c^\dagger_k c^\dagger_l \rangle - \langle c_i c^\dagger_l \rangle \langle c_j c^\dagger_k \rangle + \langle c_i c^\dagger_k \rangle \langle c_j c^\dagger_l \rangle$, the reason of interest will be explained in Sec. 3.3. The one-particle (two-point) correlations $\langle c_i c^\dagger_j \rangle$ can be obtained from the spin-resolved ARPES spectra by $\mathrm{Tr}[\rho(c_{m\uparrow} c^\dagger_{m+c,\uparrow})] = \sum_k e^{-ikr_c} \int d\omega A^+(k,\omega)$, note $\langle c_\uparrow c^\dagger_\downarrow \rangle$ derives zero for spin conserved system. We will obtain the following connected correlation

$$
\begin{aligned}
&\langle c_{m_1,\sigma_1} c_{m_1+c,\sigma_3} c^\dagger_{m_1+x,\sigma_2} c^\dagger_{m_1+c+x,\sigma_4} \rangle^{con} = \\
&\delta_{1,c} \langle c_{m_1,\sigma_1} c^\dagger_{m_1+c+x,\sigma_4} \rangle \\
&- \langle c_{m_1,\sigma_1} c^\dagger_{m_1+x,\sigma_2} c_{m_1+c,\sigma_3} c^\dagger_{m_1+c+x,\sigma_4} \rangle \\
&- \langle c_{m_1,\sigma_1} c^\dagger_{m_1+c+x,\sigma_4} \rangle \langle c_{m_1+c,\sigma_3} c^\dagger_{m_1+x,\sigma_2} \rangle \\
&+ \langle c_{m_1,\sigma_1} c^\dagger_{m_1+x,\sigma_2} \rangle \langle c_{m_1+c,\sigma_3} c^\dagger_{m_1+c+x,\sigma_4} \rangle .
\end{aligned}
\tag{3.9}
$$

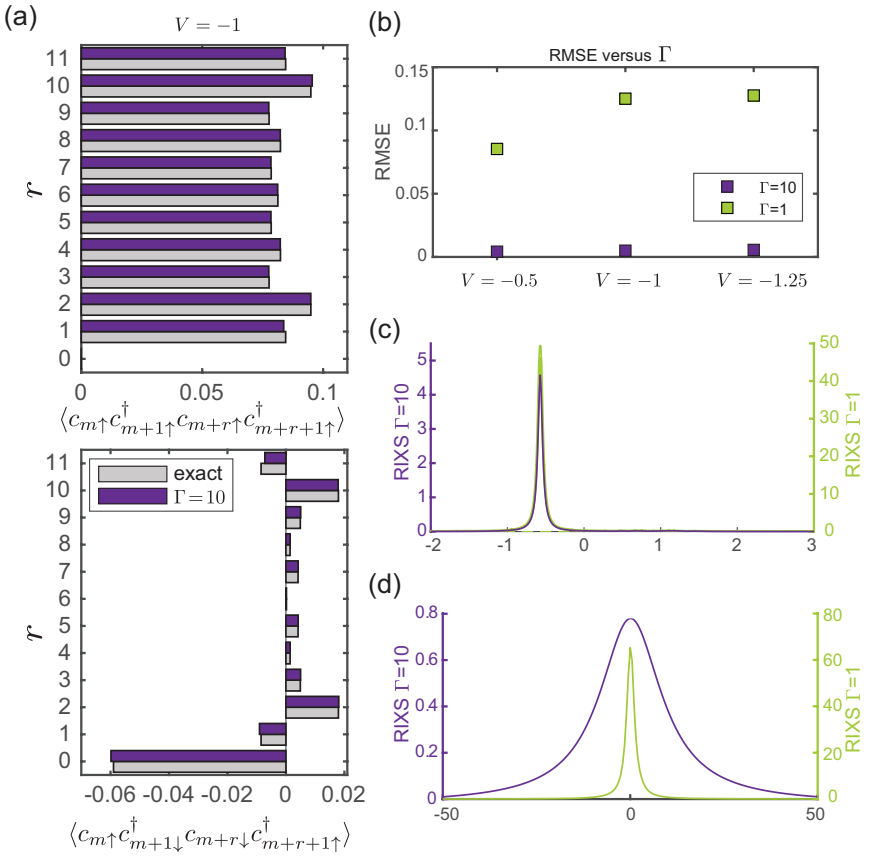

Figure 3-3: (a) The comparison between correlations derived from computational RIXS spectra and the exact values directly from exact diagonalization calculation. The results shown are from the extended Hubbard model, with $U = 1.6$, $t = 1$, $t_c = 0.1$, $\Gamma = 10$, and $V = -1$, the upper (lower) panels correspond to the spin channel $\uparrow,\uparrow,\uparrow,\uparrow$ $(\uparrow,\downarrow,\downarrow,\uparrow)$. (b) The root mean square error(RMSE) between the RIXS-derived correlations and exact correlations, in the x-axis the nearest neighbor interaction in the Hamiltonian V varies, we compare the RMSE at different inverse core-hole lifetime Γ, a large Γ is required for the small error. (c)(d) RIXS intensity at fixed momentums, $I = I(\mathbf{q} = 0, \mathbf{k}_{\text{in}} = 0, \Delta\omega, \omega_{\text{in}})$ with the same Hamiltonian parameters as the panel (a), but $\Gamma = 1, 10$ for the green and purple colors, (c) shows $\int d\omega_{\text{in}} I$ versus $\Delta\omega$, (d) shows $\int d\Delta\omega I$ versus ω_{in}.

where $x = 0, 1, -1$, these are correlations that are accessible by the combination of RIXS and ARPES.

In the ground state of the local Hamiltonian, $\langle c_{m_1,\sigma_1} c_{m_1+c,\sigma_3} c^{\dagger}_{m_1+x,\sigma_2} c^{\dagger}_{m_1+c+x,\sigma_4} \rangle^{con}$ becomes much smaller when $|x| > 1$, so we can safely ignore those correlations under many cases, we will justify this point in every model we take as examples later. We approximately find all the two-fermion (four-point) connected correlations

$\langle c_{i\sigma_1} c_{j\sigma_2} c^\dagger_{k\sigma_3} c^\dagger_{l\sigma_4} \rangle$ for particle-conserved systems with time reversal and translational symmetry. There are still many constraints in terms of "all", we need time-reversal and translational symmetry, spin and particle conservation, also local Hamiltonian, however, many well-known condensed matter systems fulfill these conditions, thus in the following discussion, we will assume we know all the two-particle correlations while justifying this approximation is reasonable along the way.

3.3 Entanglement witness in fermionic states

RIXS spectra can measure a summation of two-particle correlations like $\sum_m \langle c_m c^\dagger_{m+x} c_{m+c} c^\dagger_{m+c+y} \rangle$, when considering the dispersion of core level, the site indices between creation and annihilation operators are separate apart, i.e. $x \neq 0, y \neq 0$. Even though it does not provide a full set of all correlations $\{\langle c_i c^\dagger_j c_k c^\dagger_l \rangle, i, j, k, l \in M\}$, the following reasons enable it to approximately fully characterize all the two-particle correlations: (1) most condensed matter systems are translational invariant, (2) the connected part of the correlation functions vanishes when i, j, k, l indices are separate farther apart for the ground state of local Hamiltonian. We show that with access to these two-particle correlations, a measurable entanglement witness can be constructed. We consider only systems with conserved particle numbers.

In a fermionic state, the wave function is antisymmetric and fermion particles are indistinguishable, the definition of entanglement [4, 15] is less straightforward than states with distinguishable particles, like spin systems. One approach is to use the notion of Slater rank and concurrence [21, 22, 53], they are accessible via two-particle correlations in a two-particle system, however, Slater rank becomes much more complicated to access via two-particle correlations and the concurrence is not enough to describe the entanglement in systems with more than two particles[22]. A similar concept like three tangles can describe entanglement in a three-particle system but is not accessible by just two-particle correlations[54]. Another approach is to construct an entanglement witness like $\mathrm{Tr}\,[W\rho]$. Naively, if we can find all states that are k-producible $\rho_{\text{k-prod}} \in \mathcal{S}_{\text{k-prod}}$, and access all correlations $\{\mathcal{O}_\alpha\} \in A$, where

A is the set of all fermion operators that conserve particle number in anti-normal order $\{c_{i_1}\cdots c_{i_n}c_{j_1}^\dagger\cdots c_{j_n}^\dagger, n=1,2,\cdots,N\}$(where N is the total particle number in the system), we can find the full set of correlations of product states $W_{\text{k-prod}} = \{\{\text{Tr}\left[\mathcal{O}_\alpha\rho_{\text{k-prod}}\right], \mathcal{O}_\alpha\in A\}, \rho_{\text{k-prod}}\in\mathcal{S}_{\text{k-prod}}\}$. A state ρ is at least k-particle entangled if $\{\text{Tr}\left[\mathcal{O}_\alpha\rho\right], \mathcal{O}_\alpha\in A\}\notin W_{\text{k-prod}}$.

In realistic experiments, only a subset of A can be accessed. Assuming with accessing to all the single-particle and two-particle correlations $\{c_ic_j^\dagger, c_ic_jc_k^\dagger c_l^\dagger\}$, and define this subset as A_2. The question now becomes whether we can design an entanglement witness for k-particle entangled states in the fermion system. The witness of biparticle entangled states has been discussed in [24], where they refer to it as pairing. In the following, we first define the multiparticle entanglement in fermionic systems considering its basis-independent properties, then we construct a multiparticle entanglement witness based on the correlations we have. Here we constrain the definition of witness in the pure state subset while discussing possible extensions to the mixed states in the conclusion section.

3.3.1 Multipartite entanglement in fermionic systems

The notions of k-producibility and multipartite entanglement adapt well in spin systems. The QFI is related to the lower bound of multipartite entanglement [20], and can be probed by measuring the dynamic susceptibility [7]. If we want to adopt a similar concept in fermionic systems, the fermion particles are indistinguishable, and the definition of particle entanglement should not depend on the choices of fermion operator basis, i.e., states of the Fermi sea should be unentangled no matter in real-space basis or momentum-space basis. Here we first introduce the definition of fermionic product states like [24], following a similar manner, we can define the multiparticle entangled fermionic states. The definition of entanglement is invariant under a unitary transformation of fermionic operators $c_a=\sum_b c_{ba}c_b'$. A pure fermionic state $|\psi_p\rangle$ is called an unentangled or product state, if there exists a unitary transformation

$c_k \mapsto c'_k$ such that

$$|\psi_p\rangle = \prod_{j=1}^{N} c'^{\dagger}_j |0\rangle . \tag{3.10}$$

A mixed state ρ_s is called unentangled, if it can be written as the convex combination of product states, i.e.

$$\rho_s = \sum_{p=1}^{K} \lambda_p \rho_p \tag{3.11}$$

where $\rho_p = |\psi_p\rangle \langle\psi_p|$ are product states, $\sum_{p=1}^{K} \lambda_p = 1$, $\lambda_p \leq 1$. All other states are said to have *Slater number larger than 1* and are called entangled.

Similarly, we can define a k-particle entangled fermion state. In Ref. [55], a definition of k-producible fermion states is given, but it is basis-dependent, here we show a basis-independent definition. Consider a set of fermionic modes M, with associated creation and annihilation operators $c_m^{\dagger}$ and c_m, labeled by $m \in M$. A k partition of the system is defined as a partition $M = M_1 \cup M_2 \cup \cdots \cup M_p$. A pure fermionic state $|\psi\rangle$ defined on the set of modes M with conserved particle number N is k particle entangled if there exist a unitary transformation $c_k \mapsto c'_k$ such that it can be decomposed as

$$|\psi_{\text{k-particle}}\rangle = C_1^* C_2^* \cdots C_p^* |\rangle \tag{3.12}$$

where the operator C_j^* is restricted to act on M_j, and there are n_j particles created by C_j^*, $\sum_j n_j = N$, $\max(n_1, n_2, \cdots, n_p) = k$, $|\rangle$ refers to a vacuum state. The operator $C_j^* |\rangle$ is a genuinely multipartite entangled (GME) state, meaning it cannot be written as a product in any possible bipartition of the state for any single-particle fermion basis we use. We thus call each C_j^* a GME block with modes M_j and particle number n_j. A GME block with two fermions is easy to describe, if performing Slater decomposition on C_j^*, the result is full rank, i.e. the rank number is equal to $|M_j|/2$. And we can divide modes in M_j as subgroups $M_j^1, M_j^2, \cdots, M_j^{|M_j|/2}$, each contains 2 modes. The C_j^* operator with 2 fermions in the Slater decomposition basis can be written as

$$C_j^* = \sum_{i=1}^{|M_j|/2} \phi_i^j \prod_{M_j^i = \{m_1, m_2\}} c_{m_1}^{\dagger} c_{m_2}^{\dagger} \tag{3.13}$$

where $\phi_i^j > 0$, $\sum_{i=1}^{|M_j|/2}(\phi_i^j)^2 = 1, M_j^{i_1} \cap M_j^{i_2} = \emptyset, i_1 \neq i_2$.

3.3.2 CRDM witness multiparticle entanglement

The multiparticle entanglement of fermionic states is basis-independent, this inspires us to find values that are invariant under basis change in the two-particle correlations, also named two-particle reduced density matrix (RDM) in some literature[56, 57, 58, 59, 60, 61, 62, 63, 64, 65, 66, 67], as the witness of entanglement, represented by a function $F(O)$. The two-particle RDM is a fourth-order tensor defined as $O_{ij}^{kl} = \mathrm{Tr}\left[\rho c_i c_j (c_k c_l)^\dagger\right]$, it is Hermitian and positive semidefinite, and has the symmetry that $O_{(ij)(kl)} = -O_{(ji)(kl)} = -O_{(ij)(lk)} = O^*_{(kl)(ij)}$. A change of basis $c_i^\dagger \mapsto \sum_k U_{ik} c_k^\dagger$ acts on $F(O)$ as

$$\begin{aligned} &F\left(O_{(ij),(kl)}\right) = \\ &\quad F\left((U\otimes U)_{(ij),(mn)} O^{(\rho)}_{(mn),(pq)} (U\otimes U)^\dagger_{(pq),(kl)}\right). \end{aligned} \tag{3.14}$$

According to Wick's theorem, for a Gaussian state, we have $\langle c_i c_j c_l^\dagger c_k^\dagger\rangle = \langle c_i c_k^\dagger\rangle \langle c_j c_l^\dagger\rangle - \langle c_i c_l^\dagger\rangle \langle c_j c_k^\dagger\rangle$. For a general state, we can define the connected two-particle correlations, also named cumulant 2RDM (2CRDM) O^{con} as

$$\begin{aligned} (O^{\mathrm{con}}_{(ij),(kl)})^{(\rho)} &= \mathrm{Tr}\left[\rho c_i c_j c_l^\dagger c_k^\dagger\right] \\ &- \mathrm{Tr}\left[\rho c_i c_k^\dagger\right] \mathrm{Tr}\left[\rho c_j c_l^\dagger\right] + \mathrm{Tr}\left[\rho c_i c_l^\dagger\right] \mathrm{Tr}\left[\rho c_j c_k^\dagger\right]. \end{aligned} \tag{3.15}$$

It has the same symmetry and unitary transformation as O, is Hermitian, but not positive semidefinite, and the function $F(O^{\mathrm{con}})$ should also remain unchanged when changing the basis of $c_i^\dagger$. Additionally, there is an important particle-hole symmetry for O^{con} [67], namely

$$\begin{aligned} (O^{\mathrm{con}}_{(ij),(kl)})^{(\rho)} &= \mathrm{Tr}\left[\rho c_k^\dagger c_l^\dagger c_j c_i\right] \\ &- \mathrm{Tr}\left[\rho c_k^\dagger c_i\right] \mathrm{Tr}\left[\rho c_l^\dagger c_j\right] + \mathrm{Tr}\left[\rho c_l^\dagger c_i\right] \mathrm{Tr}\left[\rho c_k^\dagger c_j\right]. \end{aligned} \tag{3.16}$$

Naively, if we can find the singular values of O, they are the invariant scalars

under such unitary transformation, however, a rank-four tensor does not always have a singular values decomposition form, and if we combine a pair of indices (ij) and view it as a matrix, the eigenvalues of its matrix form are obtained through unitary operations in an enlarged space, which is beyond $(U \otimes U)_{(ij),(mn)}$, part of the information is missing in the diagonalization. On the other hand, there are known irreducible basic invariants of fourth-order tensor O or O^{con} [68, 69, 70, 71]

$$\begin{aligned} &\lambda_\nu(O) = \text{Tr}(O^\nu),\ \nu = 1, 2, \cdots, N \\ &F(O) = \lambda_\nu(O) \end{aligned} \tag{3.17}$$

where $\text{Tr}(A) = \sum_{i,j} A_{ijij}$, the maximal value N is the dimension of single-particle Hilbert space and the dimension of the tensor O. Thus, we have N scalars $\text{Tr}(O^\nu)$, which carry all the basis-invariant information of the tensor O. Specially, $\text{Tr}(O^2) = \sum_{i,j,k,l} |O_{ijkl}|^2$ because of the symmetry property of O. In the following, we are going to focus on the connected part of the two-particle reduced density matrix O^{con}. The particle-hole symmetry of O^{con} implies that, if we perform a particle-hole transformation for the state, its invariants $\text{Tr}(O^\nu)$ will stay the same, so there is no difference whether we treat electrons or holes as aiming particles, in the following we use "particles" to refer to either electrons or holes.

With the framework of decomposing a pure fermion state into Eq. 3.12, if ρ is any pure state, and in the basis that has this decomposition, there a few cases for i, j, k, l indices in each $O^{\text{con}}_{(ij),(kl)}$,

1. $O^{\text{con}}_{(ij),(kl)} = 0, i, k \in M_{j_1}, j, l \in M_{j_2}, j_1 \neq j_2$
2. $O^{\text{con}}_{(ij),(kl)} = 0, i, l \in M_{j_1}, j, k \in M_{j_2}, j_1 \neq j_2$
3. $i, j, k, l \in M_{j_1}$
4. $O^{\text{con}}_{(ij),(kl)} = 0$, all other situations.

The first two cases are equivalent, so we focus on case 1, and we have $\langle c_i^\dagger c_j^\dagger c_k c_l \rangle = -\langle c_i^\dagger c_k \rangle \langle c_j^\dagger c_l \rangle$, $\langle c_i^\dagger c_l \rangle = 0, \langle c_j^\dagger c_k \rangle = 0$, so $O^{\text{con}}_{(ij),(kl)} = 0$. Similarly, for all other situations that the two pairs among four indices do not each belong to the same block state in

M_j, we have $O^{\text{disc}}_{(ij),(kl)} = 0$ because all the two-particle and one-particle correlations are zero. If we treat O^{con} as a block tensor, then the case 1, 2, 3 all refer to off-diagonal components of the block tensor

$$O^{\text{con}} = \bigotimes_{j=1,\cdots,p} O^{\text{con}}_{M_j}. \tag{3.18}$$

A conclusion is derived by summarizing the above definition, if we have a pure state ρ that can be decomposed as Eq. 3.12 in any basis, then for any irreducible basic invariant, we can decompose it into a summation of separable subsystems

$$\begin{aligned} \text{Tr}[(O^{\text{con}})^\nu] &= \text{Tr}\left[\Big(\bigotimes_{j=1,\cdots,p} O^{\text{con}}_{M_j}\Big)^\nu\right] \\ &= \sum_{j=1,\cdots,p} \text{Tr}\left[\Big(O^{\text{con}}_{M_j}\Big)^\nu\right]. \end{aligned} \tag{3.19}$$

Following the similar spirit as the upper boundary obtained in QFI, here if we can find the upper boundary of $\text{Tr}(O^\nu)$ for n-particle inseparable state, like $\text{Tr}(O^\nu_{\rho_n}) \leq F_n$, then for any system with conserved N fermions, if

$$\text{Tr}\left[(O^{\text{con}})^\nu\right] \leq \left[\frac{N}{n}\right] F_n^\nu + F^\nu_{N-\left[\frac{N}{n}\right]n} \tag{3.20}$$

the system is at least $n+1$-particle entangled, and this boundary will be tighter as ν increases, this is because for a fully connected (inseparable) states containing particle number n, $\text{Tr}\left[(O^{\text{con}})^\nu\right] \sim O(n^\nu)$, we will show this explicitly for $\nu = 1, 2$, and implies the relations for $\nu > 2$. Overall, $\text{Tr}[(O^{\text{con}})^\nu]$ is size extensive for separable states and follows polynomial relations for inseparable states, which makes it a valid multipartite entanglement witness.

We derive the upper boundary F_n^ν for $\nu = 1$, for a fermion state with n particles and in total mn modes. In the later content, we will refer $\text{Tr}\left[O^{\text{con}}\right]$ as the first-order witness and $\text{Tr}\left[(O^{\text{con}})^2\right]$ as the second order witness.

$$F_n^1(m) = \left(1 - \frac{1}{m}\right) n < F_n^1(\infty) = n \tag{3.21}$$

These upper boundaries correspond to generalized GHZ states in fermion systems, with n particles and nm modes, labeling the modes as $\{1, 2, \cdots, nm\}$, the GHZ type state is

$$\begin{aligned} |\mathrm{GHZ}\rangle = \frac{1}{\sqrt{m}}\Big(& |1, 2, \cdots, n\rangle + |n+1, n+2, \cdots, 2n\rangle \\ & + \cdots + |(m-1)n+1, (m-1)n+2, \cdots, mn\rangle \Big) \end{aligned} \tag{3.22}$$

and $|ab\cdots\rangle = c_a^\dagger c_b^\dagger \cdots |0\rangle$. For the $F_n^1(m)$, we prove the upper boundary in Appendix A.2.

For $F_n^2(m)$, the upper bounds are more tricky, however, we prove the cases for $n = 2$ in Appendix A.2, and derive

$$F_2^2(m) = 4\left(1 - \frac{1}{m^3}\right) < F_2^2(\infty) = 4. \tag{3.23}$$

For $n > 3$, and specially $m = 2$ when there are n particles that fill in $2n$ modes, we can prove that

$$\begin{aligned} F_n^1(2) &= \frac{n}{2} \\ F_2^2(2) &= \frac{7}{2} \\ F_3^2(2) &= \frac{104}{27} \\ F_n^2(2) &= \frac{2n^2 - n}{4}, \ n > 2 \end{aligned} \tag{3.24}$$

The bounds at $n = 1, 2$ work for all half-filling systems, while the second order witness bound for $n > 3$ is valid when double occupation on each site is not allowed for a spinful fermion system, such that the state can be represented as a n-qubit state. For $n = 3$, there are two inequivalent maximally entangled types, GHZ states and W states, we proved that the upper bound of the second-order witness at $n = 3$ actually refers to W states instead of the GHZ states. While for all $n \neq 3$, the upper bounds are achieved by the GHZ-type states. We numerically verify some upper bounds in Sec. 3.4.2.

For $m > 2$, we can infer that

$$
\begin{aligned}
F_n^1(m) &= \left(1 - \frac{1}{m}\right) n < F_n^1(\infty) = n \\
F_2^2(m) &= 4\left(1 - \frac{1}{m^3}\right) < F_2^2(\infty) = 4 \\
F_3^2(m) &= 4\left(1 - \frac{1}{(m+1)^3}\right) < F_3^2(\infty) = 4 \\
F_n^2(m) &= 2n^2\left(\frac{1}{m} - \frac{1}{m^2}\right) - 2n\left(\frac{1}{m} - \frac{2}{m^2} + \frac{1}{m^3}\right) \\
&\leq F_n^2(2) = \frac{2n^2 - n}{4},\ n > 3
\end{aligned}
$$

We can formally prove the bounds of $F_n^1(m), F_2^2(m), F_3^2(m)$ in Appendix. A.2, while the last bound $F_n^2(m), n > 3$ is a hypothesis, it refers to the n-particle generalized GHZ states. Even though it's not proved due to the high complexity of multiparticle fermion states, the exact upper bound can not be smaller than it and it exhibits a quadratic relation with particle number n.

There is no need to consider $m < 2$, because as we mentioned already, there is a particle-hole symmetry for CRDM O^{con}, and we can always treat the state as its particle-hole inversion, and in that case, we have $m > 2$. When using Eq. 3.20 to find the multiparticle entanglement bounds for a particle-conserved state, we always choose N to be the minimum value between electron and hole numbers. For $m \geq 2$ but m is not an integer, we don't provide an exact bound but we can reason that the bound is between $F_n^\nu([m])$ and $F_n^\nu([m]+1)$.

3.3.3 CRDM measure quantum correlations

Apart from being viewed as a multiparticle entanglement witness, there is another perspective to explain the scalar $\text{Tr}[(O^{\text{con}})^2]$, which is to view it as a measure of quantum correlations. As discussed in Sec. 2.2.1, the Slater determinant is an approximation people use to describe multi-fermion quantum states, however, most strongly correlated quantum states deviate significantly from it. If we can find a quantity that is zero for the Slater determinant state, and increase as the state deviates from the

Slater determinant form, then we can call this a measure of how the extent of error in the Slater determinant approximation for a particular state. We here name it as a measure of quantum correlations. We formalize that $\mathrm{Tr}[(O^{\mathrm{con}})^2]$ is a qualified measure of quantum correlations, due to the following properties it fulfills:

1. It is Invariant under a single-particle orbital unitary transformation.
2. It vanishes for all the Slater determinant wave functions (separable fermion states), in any orthogonal single-particle orbital basis.
3. The tensor $(O^{\mathrm{con}})^2$ is positive semidefinite, and $\mathrm{Tr}[(O^{\mathrm{con}})^2] = \sum_{ijkl} |O^{\mathrm{con}}_{ijkl}|^2$.

All properties have been verified in the previous discussion. We thus can define $\mathrm{Tr}[(O^{\mathrm{con}})^2]$ as a quantified measure as it vanishes for all Slater determinant (separate) states, no matter what orthogonal single-particle orbital basis we choose to observe the state; and there is no cancellation term due to the positive semidefinite property, so any state that can not be written in the Slater determinant form must have a non-zero $\mathrm{Tr}[(O^{\mathrm{con}})^2]$. We can not yet call it a measure of entanglement, as it requires the monotonicity under local operations and classical communication (LOCC), we defer this to future studies.

3.4 Examples

As examples, we turn to illustrate the first and second-order trace of the 2CRDM in the ground states of a Hubbard model and k-particle entangled states uniformly sampled in a subspace.

3.4.1 Extended Hubbard model and entanglement entropy

We test our witness and quantum correlation measure on the extended Hubbard model as described in Sec. A.3 at half and quarter fillings. Because the results via exact diagonalization at small system size show a strong finite-size effect as shown in Appendix A.3, we apply density matrix renormalization group (DMRG) algorithm

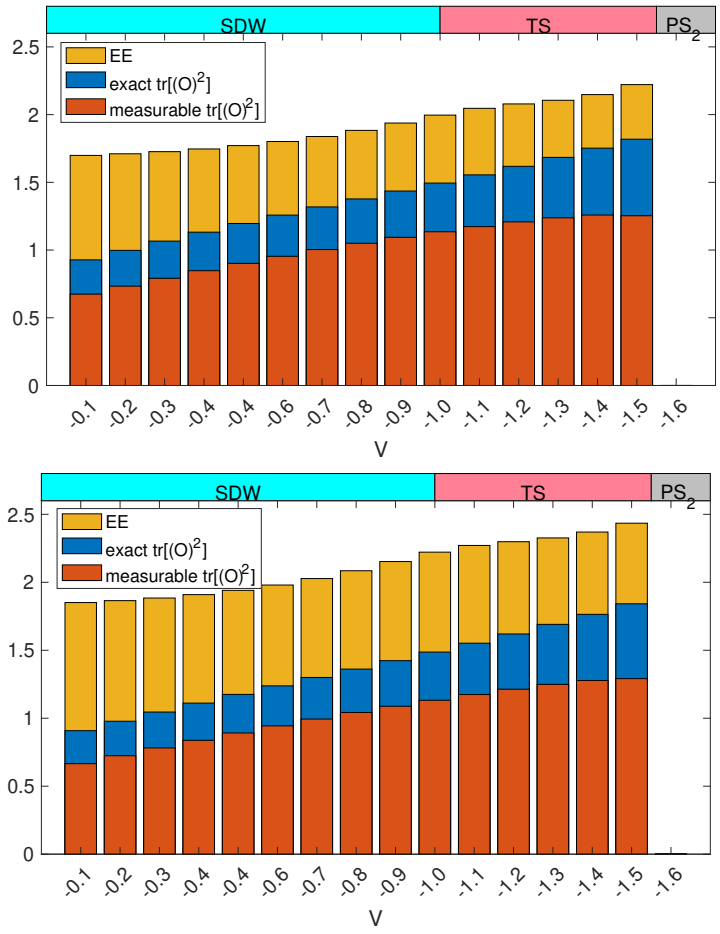

Figure 3-4: DMRG results of EHM at half filling with open boundary condition. Top: N=64, Bottom: N=128. Only the central 12 orbitals are counted for $\mathrm{Tr}\left[(O^{\mathrm{con}})^2\right]$. $U = 1.6$, $t = 1$ are fixed, and nearest neighbor interaction V changes in the x-axis. The exact and measurable values of $\mathrm{Tr}\left[(O^{\mathrm{con}})^2\right]$ and the entanglement entropy(EE) are shown.

with closed boundary conditions to calculate larger system size when there are $N = 64, 128$ sites. When measuring the correlations, we select 12 sites in the center of the 1D chain, the witness is calculated only on the subspace of these 12 sites, so it actually acts on a reduced mixed state by tracing out other sites except the 12 central sites, while our derivation of the upper bound of the witness only works in pure states. Here we neglect the effect of the bond dimension cut at the edge of these 12 sites and apply the same bound as derived in pure states. The entanglement entropy is measured by cutting the system into halves from the center site among N sites, the reduced density matrix from the left to the center site is $\rho_A = \mathrm{Tr}_B \rho_{AB}$, while A and B

represents the Hilbert space of left half and right half, and the entanglement entropy $S(\rho_A) = -\mathrm{Tr}(\rho_A \log \rho_A)$, the entanglement entropy is an intensive quantity as we approach the thermodynamics limit, as it is relative to the bond dimension between two subsystems and does not increase with the size of the system. While the witness is an extensive quantity that increases with the size, here we choose 12 central sites, if we increase the range of correlations, the witness also increases.

Fig. 3-4 shows the second-order witness and entanglement entropy(EE) at half filling, the measurable $\mathrm{Tr}\left[(O)^2\right]$ only sums over the connected correlations that are accessible by RIXS as discussed in Eq. 3.9, other inaccessible connected correlations are set to zero. The measurable $\mathrm{Tr}\left[(O)^2\right]$ is always smaller or equal to the exact value, they are both nonzero, indicating the system is entangled, otherwise, the witness should be zero as analyzed in Sec. 3.3. However, neither of the witnesses exceeds the upper bound of bi-particle entanglement($\frac{12}{2}F_2^2(2)$) or tri-particle entanglement($\frac{12}{3}F_3^2(2)$) for systems with 12 particles at half filling, so we can only detect bi-particle entanglement here. Nevertheless, we can also view $\mathrm{Tr}\left[(O)^2\right]$ as a measure of quantum correlations at the two-particle level, and we compare it with the entanglement entropy, they follow the same increasing trend when the system undergoes a phase transition from the SDW phase to TS(spin-triplet) phase, indicating an increase of the quantum correlations and the entanglement. $\mathrm{Tr}\left[(O)^2\right]$ does not change dramatically across the phase transition point, this can be explained as it serves a similar property here as the entanglement entropy, which means that it may only exhibit discontinuous behaviors across the phase transition, at the thermodynamic limit.

3.4.2 Random States

Because the proof of upper bounds in Eq. 3.24 is tedious as attached in the appendix, in order to get an impression of the strength of the criteria, here we numerically examine those upper bounds by sampling k-particle entangled random states in rep-

resentative subspace. The states in the figure are defined as

$$
\begin{aligned}
|\mathrm{N}_2\rangle =& x_1 |12\rangle + x_2 |34\rangle \\
|\mathrm{GHZ}_3\rangle =& x_1 |123\rangle + x_2 |456\rangle \\
|\mathrm{SPIN}_3\rangle =& x_1 |123\rangle + x_2 |1\overline{23}\rangle + x_3 |\overline{1}2\overline{3}\rangle + x_4 |\overline{12}3\rangle \\
=& x_1 |123\rangle + x_2 |156\rangle + x_3 |426\rangle + x_4 |453\rangle \\
|\mathrm{GHZ}_4\rangle =& x_1 |1234\rangle + x_2 |5678\rangle \\
|\mathrm{SPIN}_4\rangle =& x_1 |1234\rangle + x_2 |12\overline{34}\rangle + x_3 |1\overline{2}3\overline{4}\rangle + x_4 |1\overline{23}4\rangle \\
&+ x_5 |\overline{1}23\overline{4}\rangle + x_6 |\overline{1}2\overline{3}4\rangle + x_7 |\overline{12}34\rangle + x_8 |\overline{1234}\rangle \\
=& x_1 |1234\rangle + x_2 |1278\rangle + x_3 |1638\rangle + x_4 |1674\rangle \\
&+ x_5 |5238\rangle + x_6 |5274\rangle + x_7 |5634\rangle + x_8 |5678\rangle \\
|\mathrm{GHZ}_5\rangle =& x_1 |12345\rangle + x_2 |6789(10)\rangle
\end{aligned}
\tag{3.25}
$$

where $|ij\cdots\rangle = c_i^\dagger c_j^\dagger \cdots |\rangle$. Here $|\mathrm{GHZ}_n\rangle$ does not indicate the state is an exact GHZ state($x_1 = x_2$), but refers to the state with a similar form as the GHZ state, and x_1 not necessarily equals to x_2. In states $|\mathrm{SPIN}_3\rangle$, we label the later half indices with an overline, $\{\overline{1}, \overline{2}, \overline{3}\} \to \{4, 5, 6\}$, and similarly in $|\mathrm{SPIN}_4\rangle$. With this notation, we can transform a subset of k particle entangled states into k-qubit states. Because the phase factors of the coefficients do not matter in $\mathrm{Tr}\,[O^{\mathrm{con}}]$ and $\mathrm{Tr}\,[(O^{\mathrm{con}})^2]$, we sample random parameters $\{x_1, \cdots\}$ with a constraint $\sum_{i=1}^{p} x_i^2 = 1$ distributed uniformly on a sphere in a p-dimensional space

$$
\begin{aligned}
(x_1, \cdots, x_p) = \big(&\cos(\alpha_1), \sin(\alpha_1)\cos(\alpha_2), \cdots, \\
&\sin(\alpha_1)\cdots\cos(\alpha_{p-2}), \sin(\alpha_1)\cdots\sin(\alpha_{p-2})\sin(\alpha_{p-1})\big)
\end{aligned}
\tag{3.26}
$$

In Fig. 3-5, the upper bounds of the first-order witness(top) and second-order witness(bottom) of k-particle entangled states are shown, and the witness of sampled random states are represented as violin plots. All sampled states in their type have some instances that reach the corresponded upper bounds and do not exceed, which demonstrate the validness of the criteria, except for $|\mathrm{GHZ}_3\rangle$, which does not reach

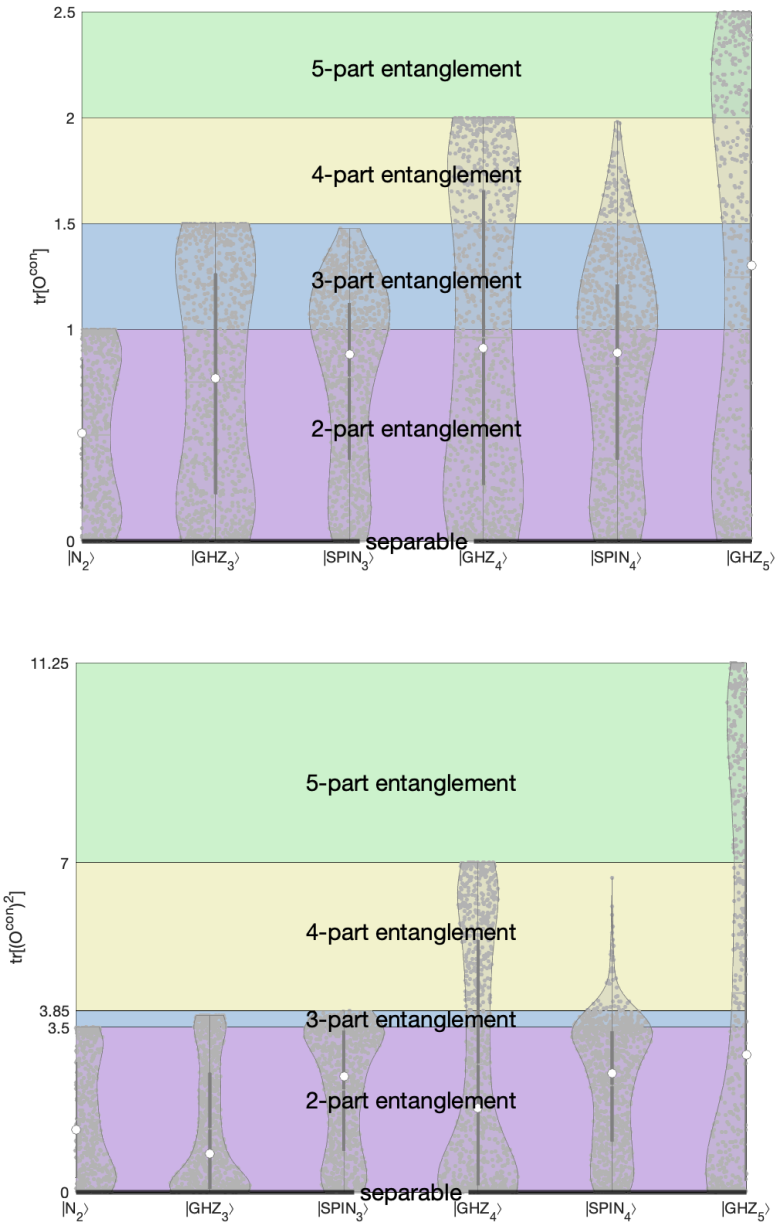

Figure 3-5: Top: Upper bound of the first-order witness Tr $[O^{\text{con}}]$ and sampled states. Bottom: Upper bound of the second-order witness Tr $[(O^{\text{con}})^2]$ and the sampled states.

the 3-particle entangled bound for the second-order witness. This is because the state that reaches this upper bound is the W state, which is not included in the $|\text{GHZ}_3\rangle$ but included in $|\text{SPIN}_3\rangle$. The W state in $|\text{SPIN}_3\rangle$ appears when $x_1 = x_2 = x_3, x_4 = 0$(or any one of the parameters is zero and others are equal), while $x_1 = x_2 = x_3 = x_4$ is equivalent to an exact GHZ state under basis transformation, see Appendix A.2.

3.5 Discussion

In this work, we propose extracting 4-point (2-particle) correlations, denoted as $\langle c_i c_j^\dagger c_k c_l^\dagger \rangle$, with high precision from RIXS spectra. By performing Fourier transformation in the incident-photon momentum, we can distinguish the perturbation part from the leading term in the spectra. The perturbation term corresponds to the dispersion of the core level and leads to the 4-point correlations, while the leading term gives rise to the spin-spin (charge-charge) correlations. The connected part of these correlations can be obtained by analyzing the difference between RIXS and ARPES spectra. Assuming access to all connected 4-point correlations, we propose fermionic basis-invariant multi-particle entanglement witnesses. We derive upper bounds for the k-particle entangled states using two of these witnesses. To examine our criteria, we investigate a 1D extended Hubbard chain undergoing a phase transition and randomly sample k-particle entangled states.

The precision of the correlations derived from RIXS spectra is influenced by the core-hole lifetime, the core-level dispersion, and the excitation spectra of the valance band. Since the 4-point correlations originate from the perturbation term of the Hamiltonian in the order of $O(\frac{t^2}{4\Gamma^4})$, the accuracy of RIXS spectra becomes crucial to capture the perturbation term, which varies with the incoming photon momentum. Improving the precision of RIXS measurements would allow us to capture higher-order perturbations and derive a complete set of 4-point correlations that surpass the nearest-neighbor constraint imposed by first-order perturbation. Alternatively, exploring materials with higher orbital as the core level could enhance core-hole mobility and increase the magnitude of the perturbation term. Unlike previous works[11] that derive the spin and charge dynamic susceptibilities from RIXS using UCL approximation at the resonance peak energy, our derivation involves integrating over the entire nonzero range of incoming photon energy. This is necessary as the 4-point correlations typically arise from higher-order excitations in the Hamiltonian energy levels, its spectra covering a wide range of incoming photon frequencies. Neglecting the RIXS intensity solely at the resonance peak leads to significant systematic errors,

as we have verified numerically.

Extracting information about quantum states from correlation functions has been a longstanding question. Rosina's theorem[72] establishes a one-to-one mapping between the energetically nondegenerate ground state two-particle reduced density matrix (2RDM) and the many-electron wave function for quantum systems with only two-particle (Coulomb) interactions. This suggests that the 2RDM, or equivalently the 4-point correlations, are sufficient to reconstruct the ground state wave function. However, the challenge lies in determining the specific approach for achieving this. Although the problem is mathematically intricate and falls under the realm of N-representability, we address a related aspect by linking it to multiparticle entanglement. We investigate whether the 2RDM can be employed to construct witnesses for k-particle entangled states, which provides a coarse-grained classification of fermionic states. Among the proposed witnesses, the second-order witness $\mathrm{Tr}\left[(O^{\mathrm{con}})^2\right]$ naturally serves as an entanglement measure due to its size extensivity and quadratic relationship with the depth of multi-particle entanglement. This witness can detect genuine multi-particle entanglement blocks in large systems. There are other invariants of the 2CRDM $O^{\mathrm{con}}_{(ij)(kl)}$ that potentially serve as entanglement witnesses, such as the eigenvalue spectra of the matrix. Naively, the largest eigenvalue is bounded as demonstrated in Appendix. A.2, thereby serving as an additional entanglement witness. However, a comprehensive analysis of the eigenvalues necessitates further investigation, which we defer to future studies.

Chapter 4

Local probes for quantum Hall ferroelectrics and nematics

Part of the work described in this chapter is published as Ref. [73].

Scanning tunneling microscopy (STM) is an effective technique utilized in the measurement of two-dimensional materials. It measures the local density of states (LDOS), as explained in Chapter 1. Given its spatial resolution, STM possesses the potential to directly visualize local features that reflect the system's symmetry. In instances where translational symmetry is broken, these features manifest prominently as charge orders observable through the nonuniform density profile obtained from STM. However, in most other scenarios involving symmetry breaking, the LDOS remains uniform, and no discernible local characteristics emerge. Nonetheless, impurities can play a crucial role in targeting a bound state that reflects the symmetry breaking and is also visualizable through STM.

In this chapter, we will explore the two-dimensional multi-valley electronic systems in which the dispersion of individual pockets has low symmetry, giving rise to quantum Hall ferroelectric and nematic states in the presence of strong quantizing magnetic fields. While the detection of valley symmetry-breaking has primarily relied on macroscopic transport or optical properties, certain experiments have successfully enabled the direct visualization of Landau orbitals' shape in the vicinity of impurities [74, 75]. This progress paves the way for directly imaging the order parameter –

dipole moment near impurities. We investigate local signatures of these states arising near impurities that can be probed via Scanning Tunnelling Microscopy (STM) spectroscopy. For quantum Hall ferroelectrics, we demonstrate a direct relation between the dipole moment measured at impurity-bound states and the ideal bulk dipole moment obtained from the modern theory of polarisation. We also study the many-body problem with a single impurity via exact diagonalization and find that nearing strong impurities non-trivial excitonic states can form with specific features that can be easily identified via STM spectroscopy.

4.1 Introduction

Recently we have witnessed an explosion of high-quality two-dimensional electronic systems with strongly anisotropic dispersions that can be driven into the quantum Hall regime in the presence of strong magnetic fields [76, 77], such as (111) surface of Bismuth [74, 75, 78, 79], AlAs heterostructures [80, 81], PbTe(111) quantum wells [82] and (001) surface of the topological crystalline insulator (TCI) like $Sn_{1-x}Pb_x$(Te,Se) [83]. In these systems, at integer fillings of the Landau levels, Coulomb interaction tends to spontaneously break symmetry by forming valley-polarized states [76, 84, 85, 86], which can be generally divided into nematic or ferrolectric states according to whether or not the Fermi surface of individual valley preserves inversion (or two-fold rotation) symmetry [76]. Advances in STM have made it possible to directly image the shape of Landau orbitals near impurities [74, 75, 78, 87], providing an exciting window into these correlated states. Evidence of the quantum Hall ferroelectrics has been reported in Bismuth (111) [75]. The surface of SnPb(Te,Se) based TCI's is another promising platform to realize these states [88, 89, 90, 91, 92].

In this chapter, we investigate the behaviour of quantum Hall ferroelectrics and nematics near short-range impurities. One of our goals is to elaborate on how to measure an "order parameter" for the quantum Hall ferroelectricity. In trivial insulators in which the bulk and the boundary are simultaneously gapped a natural order parameter is the ferroelectric dipole moment, which can be computed from the

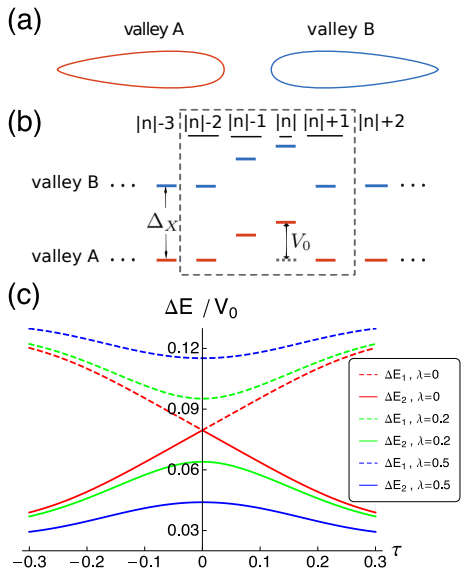

FIG. 4-1: (a) Simplistic illustration of a quantum Hall ferroelectric system. The Fermi surface consists of two valleys related by a two-fold rotation, while individual valley breaks (preserves) two-fold rotation symmetry for the ferroelectric (nematic) state. (b) Schematic of single orbit spectra, for the n^{th} Dirac Landau level: upon hybridization only 2 states are perturbed in energy by a delta-function impurity V_0 B. The exchange splitting Δ_X favors valley polarization. (c) Energies, ΔE_1 and ΔE_2, of the two impurity states for the $n = \pm 1$ Dirac Landau level, as a function of the tilt (τ) and mass (λ) of the Dirac cone.

Berry-phase-based approach in the modern theory of polarization [93, 94]. In quantum Hall ferroelectrics, although such polarization is well defined in an ideal setting subjected to periodic boundary conditions, it is unclear how to directly measure it due to screening at metallic boundaries. This issue can be resolved by studying states bound to impurities. Indeed, the ideal dipole moment defined by the modern theory of polarization can be related to that of impurity-bound states, as we will demonstrate for the case of tilted Dirac cones relevant to the surface of SnPb(Te,Se) based TCI's.

We also study numerically the many-body problem of states near short-range impurities by exact diagonalization. As previously discussed [74, 75] the impurities can shift the energy of the occupied state that has a finite amplitude at the impurity location. We have found a new many-body regime where the impurity potential exceeds the exchange energy that attempts to keep the Landau level (LL) completely

filled. For repulsive short-range impurities, once the impurity potential overcomes this threshold, a state with a quasi-hole bound to the impurity becomes the ground state of the system, and one of the lowest-lying excited states corresponds to a non-trivial inter-valley excitonic state, in which an electron is added to another valley. We will discuss how these new many-body states have clear signatures in STM measurements.

4.2 Impurity states for Dirac cones

Here we consider a model that is relevant to the (001) surface of SnPb(Te,Se) based TCI's. In these materials, at temperatures below a ferroelectric transition, their surface states comprise four Dirac cones, two of which are massive and two massless. Each of the massive/massless pair is degenerate in the presence of time-reversal symmetry [92], but under a background magnetic field, the degeneracy of the massive pair is no longer protected. The degeneracy of the massless pair will however remain protected by the product of time reversal and a mirror symmetry (see Supplement B). Here we focus on the latter two degenerate valleys. The dispersions generally have a tilt in momentum [95, 90], which is essential to the ferroelectricity that we describe below. We thus consider the following effective Hamiltonian for the Dirac cone at $\pm\bar{\Lambda}$ (near $\bar{X}$):

$$H = v_x\sigma_x p_x - v_y\sigma_y p_y \pm \delta v_x p_x + \Delta\sigma_z, \tag{4.1}$$

where σ_i are Pauli matrices and δv_x represents the tilt of the Dirac cone. For generality we have added a mass term, $\Delta\sigma_z$, to the originally massless Dirac cones which is allowed in magnetic fields due to the Zeeman effect, however, in TCI's this coupling has been seen to be negligibly small [83]. In the presence of external magnetic fields Landau levels will form, and we consider a partial filling $\nu = 1$ for the resulting 2-fold degenerate valley doublet. The quantum Hall ferroelectric (nematic) state forms when the electrons spontaneously polarize into a single one of these valleys due to interactions [76]. Figure 4-1(a) and (b) provide simplistic illustrations of this model. Inspired by recent STM experiments [74, 75], we study states near short-range

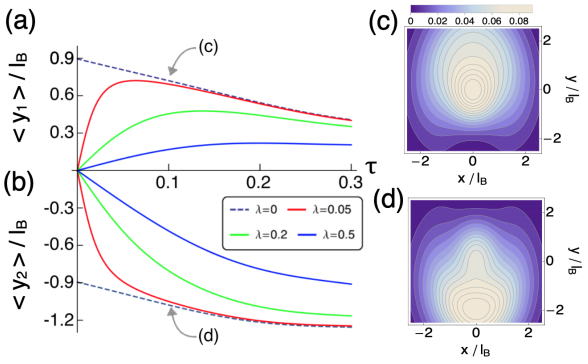

Figure 4-2: (a), (b): Average position, measured from the impurity site, of the impurity states from the $n = -1$ Dirac LL, as a function of the tilt (τ) and mass (λ) of the Dirac cone. (c), (d): Spatial probability distribution of the impurity states (for TCI parameters $\tau = 0.1$, $\lambda = 0$ and $v_x/v_y = 1.6$), which can be probed by the tunneling differential conductance in STM.

impurities modelled as delta-function potentials [96]:

$$H_{imp} = V_0 l_B^2 \, \delta(\mathbf{r}), \tag{4.2}$$

where $l_B = \sqrt{\hbar c/eB}$ is the magnetic length. Assuming that the impurity potential (V_0) is smaller than the Landau level spacing, we project the Hamiltonian to the Landau level of interest. Only states with a finite probability at the origin will be affected by the impurity potential. For a parabolic dispersion, there would be a single state per Landau level with non-zero probability at the origin, as demonstrated in the Bismuth experiments [74]. However, the situation is richer for Dirac Landau levels due to the two-component nature. Some distinctions between the conventional and Dirac Landau levels have been revealed in STM experiments on the surface of topological insulators [97], and here we discuss another distinction regarding the impurity state. The wavefunction of the n^{th} Dirac Landau level in the massless and un-tilted limit (for the general case see the Supplement B) is:

$$\psi_{n,m} = \frac{1}{\sqrt{Z_n}} \begin{pmatrix} \phi_{|n|,m} \\ s_n \phi_{|n|-1,m} \end{pmatrix}, \tag{4.3}$$

where $n \in \mathbb{Z}$, $s_n = \mathrm{sgn}(n)$ (with $s_0 = 0$), $Z_n = 2^{|s_n|}$, and $\phi_{|n|,m}$ is the wavefunction for a parabolic Landau level in the symmetric gauge with angular momentum $m - |n|$. For the $n = 0$ LL only the $m = 0$ state would have probability at the origin, however, for $n \neq 0$, two states with $m = |n|$ and $m = |n| - 1$ would have probability at the origin and opposite pseudospins [98, 99]. These two states are exactly degenerate for a massless and un-tilted dispersion, but either of these perturbations produces an energy splitting as illustrated in Fig. 4-1. Thus the impurity states are generically resolvable in STM measurements. In Supplement B we demonstrate that these perturbations do not produce extra impurity states, and therefore, only these two states are split from the bulk Landau level and bound to the impurity. Let us introduce dimensionless parameters to characterise the tilt $\tau \equiv \delta v_x/(2v_x)$ and the mass $\lambda \equiv \Delta l_B/(\sqrt{2v_x v_y})$. In $Sn_{1-x}Pb_x$(Te,Se) these are approximately $\tau = 0.1$, $\lambda = 0$ (neglecting Zeeman effect) and $v_x/v_y = 1.6$ B. It is therefore justified to use perturbation theory in τ. The splitting of the two impurity states from the bulk $n = \pm 1$ Landau level to leading order in τ, are then estimated to be: $\Delta E_1 \approx 0.10 V_0$, $\Delta E_2 \approx 0.06 V_0$. Figure 4-2 displays the spatial profile of these two states.

4.3 Ferroelectric dipole moments

In the modern theory of electric polarization [93, 94], the dipole moment of an insulator is computed by adopting periodic boundary conditions. The dipole is computed from the change of the electronic position while varying the Hamiltonian along an adiabatic path in which the bulk gap remains open and starts from an inversion symmetric reference state. Following this principle, a dipole moment for the ferroelectric quantum Hall state was introduced in Ref. [76]. For tilted Dirac cones, this dipole moment per particle to leading order in the tilt is:

$$\mathbf{D}_n = \tilde{s}_n \sqrt{2}\, \tau\, e\, l_B \left(\frac{2\lambda^2 + 3|n|}{\sqrt{\lambda^2 + |n|}} \right) \sqrt{\frac{v_y}{v_x}} \hat{\mathbf{y}}, \tag{4.4}$$

here $\tilde{s}_n = \mathrm{sgn}(n)$ (with $\tilde{s}_0 = 1$). Notice that the dipole along the tilt (x-axis) vanishes [76]. The limitation of this definition is that one assumes the charge that flows through the bulk will appear intact at the surface, providing a net electric polarization. However, in an insulating topological phase with a metallic boundary, the latter assumption is unjustified since the surface charge can flow and lead to vanishing macroscopic polarization. Hence it is important to devise alternative diagnostics of inversion asymmetry in topological phases such as the quantum Hall ferroelectrics.

Impurity states, which can be locally probed by STM, offer a resolution. For any given impurity state one can define a dipole moment as the expectation value of the position measured relative to the center of the impurity potential. If the impurity potential is inversion symmetric, this dipole moment serves to characterize the inversion asymmetry of the host state. Figure 4-2(a) and (b) display the average position of the impurity states in tilted Dirac cones as a function of their mass and tilt. Interestingly, the average position is non-analytic, as evidenced by the fact that the limits of $\tau \to 0$, $\lambda \to 0$ do not commute in Fig. 4-2. This is a consequence of the fact that in this limit both impurity states are degenerate and hence the expectation values on individual states become ambiguous. However, the sum of the average positions in both impurity states is free from ambiguities and vanishes as $\tau \to 0$, $\lambda \to 0$. We, therefore, introduce the notion of the *impurity dipole moment*, $\mathbf{D}^{\mathrm{imp}}$, as the sum of the average position of impurity states ψ_i [1]:

$$\mathbf{D}^{\mathrm{imp}} = e \sum_i \langle \psi_i | \mathbf{r} | \psi_i \rangle. \tag{4.5}$$

To leading order in the tilt (τ) and mass (λ) of the Dirac cone, we obtained the following relation between the adiabatic bulk dipole moment, in Eq. (4.4), and the impurity dipole moment:

$$\mathbf{D}_n^{\mathrm{imp}} = \frac{2|n|}{3|n| + 2\lambda^2} \mathbf{D}_n, \tag{4.6}$$

[1] This average coincides with the minus of dipole moment weighted by the charge distribution of the hole that is left in Landau level which can also be directly accessed by STM measurements.

for the n^{th} Dirac Landau level in a Dirac cone of mass λ (derivation is presented in the Supplement B). This formula summarizes one of the key messages of our study: local measurement of the impurity dipole moment, $\mathbf{D}^{\text{imp}}$, combined with the knowledge of the electronic structure, can be used to probe the bulk adiabatic dipole moment following from the modern theory of polarisation, $\mathbf{D}$, in a quantum Hall ferroelectric state.

In the massless limit, i.e. $\lambda \ll \sqrt{|n|}$, the two dipole moments have a simple proportionality relation, $\mathbf{D}_n^{\text{imp}} = (2/3)\mathbf{D}_n$. However, a notable difference between these two notions appears in the large mass limit, i.e. $\lambda \gg \sqrt{|n|}$, for which the adiabatic dipole grows linearly with the mass, $|\mathbf{D}_n| \propto \lambda$, whereas $|\mathbf{D}_n^{\text{imp}}| \propto 1/\lambda$. This markedly different behavior is a consequence of the approach to the parabolic mass limit as we explain in the Supplement B.

4.4 Many-body physics near impurities

So far we have largely ignored the role of electron-electron interactions by imagining a large self-consistent exchange field has set in to select a single valley. Next, we will study the many-body problem in the presence of the impurity potential from Eq. (4.2) by means of exact diagonalization on a torus. We concentrate here on the ferroelectric states where two valleys are described by the tilted massless Dirac cone with the same axis orientation and velocity ratio but opposite tilt. We expect the states at Landau level $n = +3$ to essentially carry over to the case of Bismuth Surfaces [74, 75, 78, 79]. In the Supplement B, we also present a nematic model of two valleys with anisotropic masses whose principal axes are rotated by $\pi/2$, as in AlAs quantum wells [80, 81], which gives a simpler picture of what we find.

In the absence of impurity ($V_0 = 0$) at the $n = +3$ Dirac LL and partial filling $\nu = 1$, the ground state of the system sponaneously polarizes into a single valley and an exchange splitting, Δ_X, between the two valleys develops [76, 85, 86]. This is schematically depicted in Fig. 4-1(a) and (b). In the forthcoming discussion, we

choose the chemical potential to lie exactly in the middle of the charge gap, namely, we add a single particle term to the Hamiltonian so that far away from the impurity the energy to add one electron equals the energy to add one hole. In STM spectra this is satisfied when the two peaks corresponding to the occupied and empty valleys in the Landau level are located symmetrically away from zero bias with no impurity, as illustrated in Fig. 4-3. We assume a sufficiently strong tilt so that the lowest-energy charged excitations are not skyrmions [76].

We denote the valley polarization of states by a vector $(N_{\rm A}, N_{\rm B})$, where N_i is the number of electrons in valley i ($i = $ A, B). The ground state at $\nu = 1$ in the absence of the impurity, therefore, has polarization $(N_\phi, 0)$. The number of orbits in a single valley is taken to be $N_\phi = 40$. STM is customarily viewed as a probe of the density of states of the single particle charged excitations because it requires the removal or injection of electrons from the sample. As we will see, however, near strong impurities, it is possible to use STM to probe excitonic states. For a weak impurity, $V_0 \ll \Delta_X$, as the STM tip is brought near the impurity one expects simply a shift of the spectrum by an energy $\sim V_0$, reflecting the local change of energy to remove/add particles as illustrated by peaks A, B in Fig. 4-3. In this regime, one encounters excitonic states inside the gap. However, they are *invisible* in the STM spectrum because they are *neutral* and hence orthogonal to states with added/removed electrons relative to the ground state.

Interestingly, when the impurity potential exceeds a threshold on the order of exchange splitting, the ground state of the system is no longer the fully valley-polarized state, $(N_\phi, 0)$, but rather a quasihole state with polarization $(N_\phi - 1, 0)$ [2], as described in Fig. 4-3(a). This is essentially the local doping of the ground state by removing one electron. Importantly, there appear then two energetically close excited states with quantum numbers $(N_\phi, 0)$ and $(N_\phi - 1, 1)$. These two lowest excited states differ from the ground state by *adding* a single electron, and hence will appear as two peaks

[2]Here we describe the behavior for repulsive impurities $V_0 > 0$, but equivalent statements hold for attractive impurities after performing a particle-hole conjugation $(N_{\rm A}, N_{\rm B}) \to (N_\phi - N_{\rm B}, N_\phi - N_{\rm A})$. Particularly, the quasihole state in the repulsive case is replaced by a quasi-particle state in the attractive case.

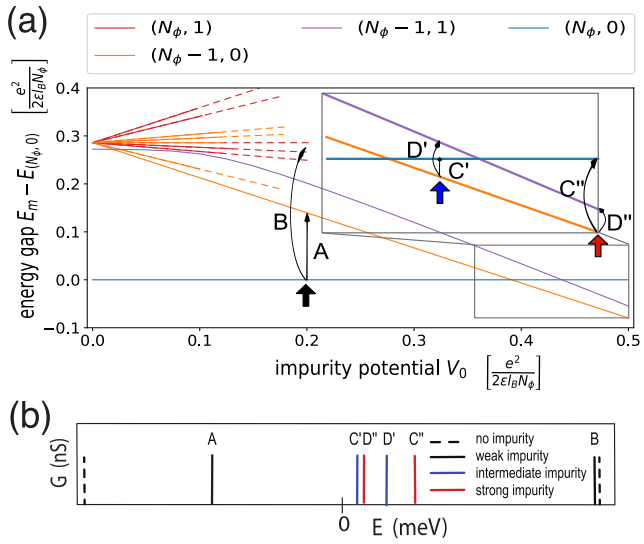

Figure 4-3: (a) Spectra with increasing impurity potential: $(N_\mathrm{A}, N_\mathrm{B})$ labels the state with N_A electrons in valley A and N_B electrons in valley B. Energy is measured relative to that of $(N_\phi, 0)$. Notice that the ground state is changed from $(N_\phi, 0)$ to $(N_\phi - 1, 0)$ as the repulsive impurity becomes stronger. Here we use $N_\phi = 40$, $\tau = 0.1$, $v_x/v_y = 5$ and $\lambda = 0$. (b) Illustration of tunneling peaks measured via STM. The peaks are labeled in correspondence with the tunneling processes indicated in the upper panel. For simplicity in (b) we only show one of the two impurity levels that split from the bulk Landau level. The other is visible in panel (a) as a solid-dashed orange line.

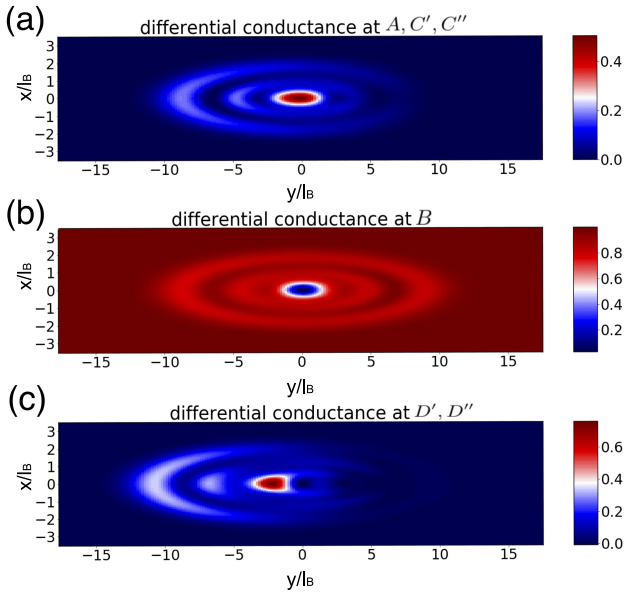

Figure 4-4: The local density of states at energy levels A, B, C', D', C'', D'', which is proportional to the differential conductance obtained by STM measurements. The unit of length is set to be l_B. The tilt $\tau = 0.1$ and velocity ratio $v_x/v_y = 5$ are used.

(C and D) at positive bias in the STM spectrum, as shown in Fig. 4-3(b). These two peaks shift sides as V_0 increases, when the energy of $(N_\phi, 0)$ exceeds $(N_\phi - 1, 1)$. Experimentally these peaks can be distinguished by probing the respective spatial differential conductance, as detailed in Fig. 4-4.

The $(N_\phi - 1, 1)$ state can be viewed as an excitonic state bound to the impurity. Since it differs from the local ground state by one electron its wavefunction can be imaged by STM. The differential conductance of adding an electron in STM is given by the local density of state (LDOS) at energy ε:

$$G(\mathbf{r}) \propto \sum_m |\langle \phi_m | \sum_j \left(c^\dagger_{\mathrm{A},j} \phi^*_{\mathrm{A},j}(\mathbf{r}) + c^\dagger_{\mathrm{B},j} \phi^*_{\mathrm{B},j}(\mathbf{r}) \right) |\phi_0\rangle|^2, \tag{4.7}$$

where $|\phi_0\rangle$ is the lowest energy state. For a weak impurity below the threshold, $|\phi_0\rangle = |N_\phi, 0\rangle$. Above the threshold, $|\phi_0\rangle = |N_\phi - 1, 0\rangle$, which is the hole state created by the impurity. $c^\dagger_{i,j}$ and $\phi_{i,j}$ are the creation operator and single electron wavefunction for an orbit j on valley i. $\langle \phi_m|$ is the state with energy ε, the sum over m is taken for all degeneracy. The case of removing an electron follows from Eq. (4.7) by replacing $c^\dagger_{i,j}$ and $\phi^*_{i,j}$ with $c_{i,j}$ and $\phi_{i,j}$ respectively.

Figure 4-4 depicts the expected shape of the differential conductance in STM at the energy and impurity indicated in Fig. 4-3. The B peak in the spectroscopy includes multiple nearly degenerate states, here in Fig. 4-4 we treat them as degenerate at energy ε and average over them. The first two panels of Fig. 4-4 depict tunneling between a single-hole or electron state and the fully polarized state, which only involves single-body physics; while the last panel is the tunneling between the hole state and the excitonic state, though only reflects the LDOS of valley B with one electron, its shape is modified via the interaction with the hole in valley A. The significant difference between Fig. 4-4(a) and (c) allows for distinguishing this non-trivial excitonic state in STM.

Chapter 5

Charge order in twisted transition metal dichalcogenide bilayers

Part of the work described in this chapter is published as Ref. [100].

In this chapter, we will explore the charge orders that emerge due to the spontaneous symmetry breaking induced by the long-range Coulomb interaction in transition metal dichalcogenide (TMD) bilayers. Experimentally, the charge-ordered insulating states at fractional fillings can be probed by optical anisotropy experiments[101, 102], and the density profile of charge orders can be observed directly from the STM images[64], which is the most direct evidence. The real-space imaging of charge orders is accomplished through the combination of high spatial resolution in advanced STM techniques, and the expanded moiré lattice resulting from moiré heterostructure effects. While the primary focus of this chapter centers around theoretical modeling to predict and understand these charge orders, it serves as an example of how the combination of spectroscopic observations and theoretical modeling advances our understanding of novel materials.

Moiré superlattices of TMD bilayers have been shown to host correlated electronic states, which arise from the interplay of long wavelength moiré potential and long-range Coulomb interaction. Here we theoretically investigate structural relaxation and single-particle electronic structure of twisted TMD homobilayer. From the large-scale density functional theory calculation and continuum model with layer degrees

of freedom, we find that the out-of-plane gating field creates a tunable charge transfer gap at the Dirac point between the first and second moiré valence bands. We further study the charge orders at the fractional band fillings. In the flat band limit, we find from Monte Carlo simulations a series of charge-ordered insulating states at various fillings $n = 1/4, 1/3, 1/2, 2/3, 1$. We predict that the gating field induces a phase transition between different electron crystals at fixed filling $n = 1/2$ or $2/3$. At half-filling $n = 1$, the ground state is a Mott insulator with electronically driven ferroelectricity. Our work demonstrates that transition metal dichalcogenide homobilayer provides a powerful platform for the investigation of tunable charge transfer insulators and charge orders.

5.1 Introduction

Moiré superlattices are a fruitful platform for realizing and controlling correlated electron states, as evidenced by the remarkable success in twisted bilayer graphene (TBG) [103, 104, 105, 106, 107, 108, 109, 110, 111, 112, 113, 114] and trilayer graphene-hBN heterostructure[115, 116, 117, 118]. Recently a new family of moiré materials based on transition metal dichalcogenides (TMD) [119, 120, 121, 122, 123, 124, 125, 126, 127, 128, 129, 130, 131] have attracted great interest. They host an abundance of correlated insulating states at a series of fractional fillings [132, 133, 134, 135, 101].

In TMD bilayers, moiré bands are formed from parabolic bands of individual layers. In twisted TMD homobilayers, the moiré bandwidth can be made arbitrarily small by reducing the twist angle, which gives rise to a strong correlation without fine-tuning. Electrons or holes in these moiré bands are tightly localized in high-symmetry stacking regions, which can be well described by a simple effective tight-binding model. This description offers a convenient starting point for investigating interaction-induced states at finite density. Despite the conceptual simplicity, quantitative modeling of moiré bands in TMD is highly nontrivial. For example, the moiré bandwidth of TMD heterobilayer WSe_2/WS_2 is only on the order of 10 meV, and depends highly on the lattice relaxation [132, 133, 136, 137].

In this work, using the large-scale density functional theory, continuum model approach, and Monte Carlo simulation, we study the effect of structural relaxation and electric field on the moiré band structure in twisted TMD homobilayers and predict novel charge orders at fractional fillings in the strong-coupling regime. We focus on the moiré valence bands originating from the Γ pocket [138, 139, 140, 141, 142]. Due to interlayer tunneling and lattice relaxation, these moiré bands are derived from localized orbitals in MX and XM stacking regions that form a honeycomb lattice. We find a pair of massless Dirac fermions at K, K' points of the mini Brillouin zone (BZ), which is protected by the D_3 point group symmetry of the moiré superlattice. Applying an out-of-plane electric field breaks the sublattice symmetry of the honeycomb lattice and opens a tunable gap Δ at the Dirac point. We introduce a new continuum model for twisted TMD homobilayers, which captures the layer degrees of freedom and the electrically tunable gap.

We further use an extended Hubbard model on the honeycomb lattice and perform Monte Carlo simulations to study the insulating electron crystals in the flat band limit. We find a distinctive set of charge orders at hole fillings $n = 1/4, 1/3, 1/2, 2/3, 1$ on the honeycomb lattice. Interestingly, the charge orders at $n = 1/2$ and $2/3$ both break the rotational symmetry and differ from the proposed states in the WSe_2/WS_2 heterobilayer. And the $n = 1$ insulating state has a spontaneous out-of-plane ferroelectric polarization, which can be switched by the electric field. These symmetry breaking charge orders can be directly probed by the optical anisotropy experiments [101, 102]. Moreover, we predict that phase transitions between distinct charge-ordered states at the same filling can be induced by the electric field, which tunes the charge-transfer gap Δ. Our work shows that twisted homobilayer MoS_2 provides an ideal platform for investigating electrically tunable charge transfer gap and charge orders.

5.2 Structure and lattice relaxation in untwisted homobilayer

We study TMD homobilayers with a small twist angle starting from AA stacking, where every metal (M) or chalcogen (X) atom on the top layer is aligned with the same type of atom on the bottom layer [1]. Within a local region of a twisted bilayer, the atom configuration is identical to that of an untwisted bilayer, where one layer is laterally shifted relative to the other layer by a corresponding displacement vector $\boldsymbol{d}_0$. For this reason, the moiré band structures of twisted TMD bilayers can be constructed from a family of untwisted bilayers at various $\boldsymbol{d}_0$, all having 1×1 unit cell. Our analysis thus starts from untwisted bilayers [143].

In particular, $\boldsymbol{d}_0 = 0, -(\boldsymbol{a}_1 + \boldsymbol{a}_2)/3, (\boldsymbol{a}_1 + \boldsymbol{a}_2)/3$, where $\boldsymbol{a}_{1,2}$ is the primitive lattice vector for untwisted bilayers, correspond to three high-symmetry stacking configurations of untwisted TMD bilayers, which we refer to as MM, XM, MX. In MM (MX) stacking, the M atom on the top layer is locally aligned with the M (X) atom on the bottom layer, see Fig. 5-1a. Likewise for XM. The bilayer structure in these stacking configurations is invariant under three-fold rotation around the z axis.

In homobilayer TMD, the spin degenerate Γ pockets in the valence band arise from electron tunneling between the two layers. The $k \cdot p$ Hamiltonian takes the form:

$$\mathcal{H}(\boldsymbol{d}_0) = \begin{pmatrix} -\frac{\hbar^2 k^2}{2m^*} + \epsilon_b(\boldsymbol{d}_0) & \Delta_T(\boldsymbol{d}_0) \\ \Delta_T^\dagger(\boldsymbol{d}_0) & -\frac{\hbar^2 k^2}{2m^*} + \epsilon_t(\boldsymbol{d}_0) \end{pmatrix}. \tag{5.1}$$

Here $m^* = 1.07 m_e$ is the effective mass for the valence band. $\Delta_T(\boldsymbol{d}_0)$ is the interlayer tunneling amplitude which depends on the in-plane displacement between the two layers. In contrast to the complex tunneling amplitude for the K pockets [144], here the time-reversal symmetry at Γ pocket enforces $\Delta_T(\boldsymbol{d}_0)$ to be real. The potential term $\epsilon_{b,t}(\boldsymbol{d}_0)$ denotes the energy of the valence band maximum in the absence of tunneling, which arises from the unequal layer weight of the wavefunction at MX and XM stacking configuration.

[1] AB stacking can be viewed as a 180° rotation of top layer

We expand $\Delta_T(\boldsymbol{d}_0)$ in Fourier components up to the second harmonic term:

$$\Delta_T(\boldsymbol{d}_0) = w_0 + 2w_1 \sum_{j=1}^{3} \cos(\boldsymbol{G}_j \cdot \boldsymbol{d}_0) + 2w_2 \sum_{j=1}^{3} \cos(\boldsymbol{2G}_j \cdot \boldsymbol{d}_0), \tag{5.2}$$

where $G_i (i = 1, 2, 3)$ are the three reciprocal lattice vectors in monolayer TMD. Due to three-fold rotational symmetry, Δ_T is a local extremum for MM, MX, and MX stackings, with $\Delta_T = w_0 + 6w_1 + 6w_2$ for d_0=0 (MM) and $w_0 - 3w_1 - 3w_2$ for $d_0 = \pm(\boldsymbol{a}_1 + \boldsymbol{a}_2)/3$ (MX or XM). The zero-momentum-transfer tunneling term w_0 is responsible for the large bonding and antibonding energy splitting for all d_0, while w_1, w_2 capture the variation of the tunneling amplitude at different lateral displacements.

The interlayer tunneling strength depends significantly on the layer spacing d. From the DFT calculation, we find the equilibrium layer spacing of untwisted TMD bilayers in MM, MX, and XM stackings: $d_{MM} = 6.63$ Angstroms and $d_{MX} = d_{XM} =$ 5.97 Angstroms. The 10% variation of layer spacing is comparable with that in bilayer graphene [145] and strongly impacts the energy splitting of Γ pockets.

By calculating the work function, we plot in Fig. 5-1 the band structure of MM and MX-stacked bilayers, with reference energy $E = 0$ chosen to be the absolute vacuum level. Using the relaxed layer spacings, we find the energy splitting in MX (or XM) stacking to be stronger than in MM, as a result of its smaller layer distance. From the different energy splitting at Fig. 5-1c, we obtain the tunneling parameters as $w_0 = 338$ meV, $w1 + w2 = -18$ meV. If the same layer spacing were used for both MX and MM bilayers, the opposite (and incorrect) conclusion about the energy splitting would be found, see Fig.5-1b. Thus lattice relaxation is crucial for obtaining the correct moiré band structure.

5.3 Moiré superlattice and effective continuum model

The structure of twisted TMD homobilayers can be described by a lateral shift $\boldsymbol{d}_0$ that varies slowly in space: $\boldsymbol{d}_0 = \theta\hat{z} \times \boldsymbol{r}$. Therefore we construct the following continuum

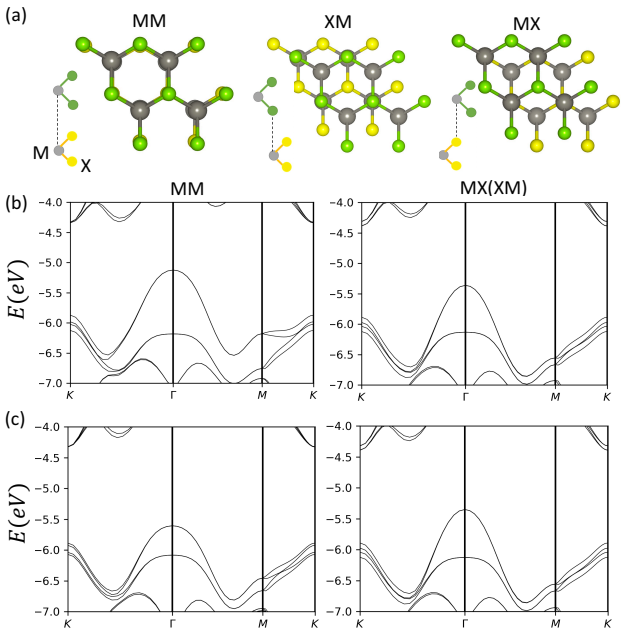

Figure 5-1: (a) Lattice structure of MM, MX, XM spots for AA stacking heterobilayer, M stands for metal atom and X stands for chalcogen atom (Green for the top layer, yellow for the bottom layer). DFT band structures of MM and MX(XM) stacking homobilayer in (b) MoS_2/MoS_2 with identical layer spacing; (c) MoS_2/MoS_2 with relaxed layer spacing.

Hamiltonian for the moiré bands from Γ pocket two-band kp model:

$$\mathcal{H} = \begin{pmatrix} -\frac{\hbar^2 k^2}{2m^*} + \epsilon_b(r) & \Delta_T(r) \\ \Delta_T^\dagger(r) & -\frac{\hbar^2 k^2}{2m^*} + \epsilon_t(r) \end{pmatrix} \tag{5.3}$$

The position-dependent tunneling term is obtained by replacing $\boldsymbol{d}_0$ with $\theta\hat{z} \times \boldsymbol{r}$ in Eq.(5.2):

$$\Delta_T(\boldsymbol{r}) = w_0 + 2w_1 \sum_{j=1}^{3} \cos(\boldsymbol{G_j^m} \cdot \boldsymbol{r}) + 2w_2 \sum_{j=1}^{3} \cos(\boldsymbol{2G_j^m} \cdot \boldsymbol{r}) \tag{5.4}$$

Where $\boldsymbol{G_i^m} = \boldsymbol{G_i}\theta \times \hat{z}(i = 1, 2, 3)$ are the three reciprocal lattice vectors in moiré superlattice. Likewise, the intralayer potential $\epsilon_{t,b}$ (t, b stand for top and bottom layer, respectively) can be expressed as the first order Fourier expansion over moiré

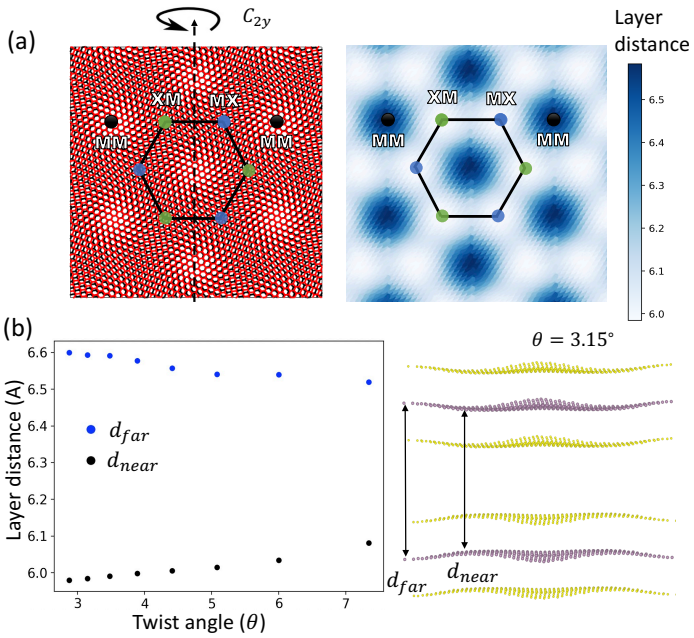

Figure 5-2: (a) Real-space moiré pattern of heterobilayer TMD heterobilayer, where MM, MX, XM spots within one supercell are labeled, and the diagram for spacial dependent layer distance (in the unit of Angstrom) in the moiré superlattice; (b) Twist-angle dependent layer spacing for d_{far} and d_{near}, and out of plane corrugation.

reciprocal lattice vector:

$$\epsilon_{t,b}(\boldsymbol{r}) = 2V_0 \sum_{j=1,2,3} \cos\left(\boldsymbol{G_j^m} \cdot \boldsymbol{r} \pm \phi\right) \tag{5.5}$$

The sign of phase factor ϕ changes under layer exchange, enforced by C_{2y} symmetry as shown in Fig. 5-2a. The potential term is crucial for the later modeling with out-of-plane gating field.

We now compare the band structure from the continuum model with the large-scale density functional theory. The moiré superlattice is fully relaxed with van der Waals correction incorporated by the vdW-DF (optB86) functionals [146] as implemented in the Vienna Ab *initio* Simulation Package[147]. We plot the twist-angle dependent layer distance, d_{far} at MM region, and d_{near} in MX (XM) region, in Fig. 5-2b. At small twist angle $\theta \sim 0$, the two layers are corrugated, and the layer distance of MM, MX, or XM stacking region approaches to that of the untwisted structure.

The interlayer tunneling amplitude is maximum at MX and XM regions, which are related by C_{2y} symmetry. As a result, low-energy moiré bands are formed from layer-hybridized orbitals in MX and XM regions, which form a honeycomb lattice with identical on-site potential.

We perform the large-scale DFT simulation to calculate the band structures for various twist angles, shown in Fig. 5-3. We find that above a small moiré period $L_m \sim$ 4.7 nm with twist angle $\theta = 3.89°$, the two topmost moiré s bands are well separated from the remaining bands. Similar band structures are also found in large-scale DFT calculation with fully relaxed lattice structure for homobilayer MoS_2[138, 139] and WS_2[140]. Fitting the DFT moiré band structure to the continuum model, we obtain the parameters as $w_0 = 338$ meV, $w_1 = -16$ meV, and $w_2 = -2$ meV, $V_0 = 6$ meV, $\phi = 121°$ at twist angle $\theta = 2.876°$. These values are consistent with the estimation from untwisted structures.

As shown in Fig. 5-3(a,c), the moiré bands exhibit Dirac points at K and K' points of the moiré Brillouin zone. These Dirac points are protected by the D_3 point group of twisted TMD homobilayer: the doublet at K or K' form a two-dimensional E representation. The bandwidth of Dirac bands changes monotonously from 250 meV to 10 meV when twist angle θ ranges from 6° to 2° as shown in Fig. 5-3b. This provides an ideal platform to study the tunable correlation physics of Dirac electrons at the filling of $n = 2$ per moiré unit cell.

In the case of twisted bilayer graphene [148], the low energy Dirac fermion is protected by the C_{2z} symmetry, which can not be broken by the out-of-plane field. However, in MX and XM regions of the twisted homobilayer MoS_2, the wavefunctions have unequal layer weights as indicated by the untwisted calculation. Thus the out-of-plane gating field breaks the C_{2y} symmetry and gaps out the Dirac fermion. A simplified continuum model targeting at antibonding orbitals well captures the topmost moiré bands, but can not describe the band structure and charge distribution involving layer degrees of freedom.

We further calculate the band structure of the fully relaxed moiré superlattice of homobilayer MoS_2 with the applied gating field. As shown in Fig. 5-3d, an out-of-

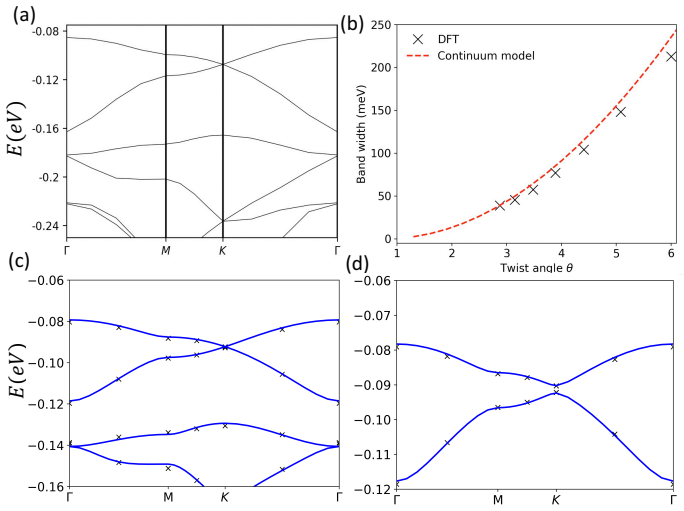

Figure 5-3: (a)DFT Band structure for $\theta = 3.89°$; (b)Twist angle dependent bandwidth for the first two moiré bands (top two valence bands in (a)) of the honeycomb lattice. DFT (black cross) and continuum model(blue line) band structures for (c) $\theta = 2.876°$; (d) $\theta = 2.876°$ with 0.5 V/nm out of plane gating field.

plane gating field 0.5 V/nm creates a 2.4 meV gap at K point, while the bandwidth of the first energy-separable moiré band is 12 meV. At K point of the band edge, the wavefunction of the first band is localized at MX region, while the second band is at XM region. For small twist angle $\theta = 2°$ with wavelength $L_m = 9.1$ nm, the gating field $E_d = 1V/nm$ induces a charge transfer gap Δ up to 5 meV, even larger than the bandwidth of the topmost moiré band (see supplementary material). A larger field-induced Δ can be achieved in twisted TMD homobilayers with reduced interlayer tunneling (which competes with the layer potential asymmetry). This can be realized by inserting an hBN layer in between the top and bottom TMD layers [126].

5.4 Tunable charge order in honeycomb lattice

In the TMD superlattice, the local minimums of the periodic moiré potential can be viewed as the effective moiré atoms to host charge. Under the harmonic approximation, the size of the Wannier orbital for the topmost moiré band is given

by $\xi = \sqrt{\frac{\hbar}{m^*\omega}} = 2\,(\pi)^{-\frac{1}{2}}\,\sqrt{L_m}(\frac{\hbar^2}{m^* V_m})^{\frac{1}{4}}$ [136](V_m is the moiré potential integrated to antibonding orbitals). In homobilayer system without lattice mismatch, the kinetic energy over nearest neighbor interaction (t/V_1) can be tuned arbitrarily small, so that the classical model is well justified at a sufficiently small twist angle. The effective extended Hubbard model without kinetic energy is given by:

$$H_0 \;= \sum_{j\in B} \Delta n_j + \sum_i U n_{i\uparrow} n_{i\downarrow} + \;\; \frac{1}{2}\sum_{i\neq j} V_{ij} n_i n_j \tag{5.6}$$

Here Δ is the charge transfer gap between two sublattice sites A and B, and V_{ij} is the extended interaction between i and j sites.

In twisted homobilayer MoS_2, the gating field introduces a charge transfer gap Δ. We first discuss the situation with large Δ. At filling $n < 1$, the effective tight-binding model reduces to a triangular lattice model, as in the case of WSe_2/WS_2, and exhibits similar charge orders. Various insulating states have been observed at fractional fillings $n = 1/4, 1/3, 2/5, 1/2, 3/5, 2/3$[134, 132, 133]. Due to the strong on-site Coulomb repulsion $U >> \Delta$, the system at $n = 1$ should be regarded as a charge transfer insulator [136]. When doped to a higher filling $n > 1$, additional charges transfer to the other sublattice/layer.

Here we further study the charge orders of honeycomb lattice with small Δ including $\Delta = 0$ in flat band limit. We perform classical Monte Carlo simulation up to 120×120 sites with periodic boundary conditions for the extended Hubbard model with different gate distances from $d = L_m/2$ to $d = 10L_m$. The distance-dependent interaction strength is plotted in Fig. S2 up to V_{100}, and the interaction cutoff is chosen as $0.1\%V_1$. We identify a series of charge orders at $n = 1/4, 1/3, 1/2, 2/3, 1$. For $n < 1/2$, moiré electrons are all filled to one sublattice, exhibiting similar charge orders (or generalized Wigner crystals) as observed in WSe_2/WS_2 heterobilayer [44, 132, 149].

Interestingly, for small Δ, we find that charge transfer involving two sublattices already takes place for filling $n \geq 1/2$, leading to new charge-ordered states beyond those found in WSe_2/WS_2. At filling factor $n = 1/2$, we find an emerging rectangular

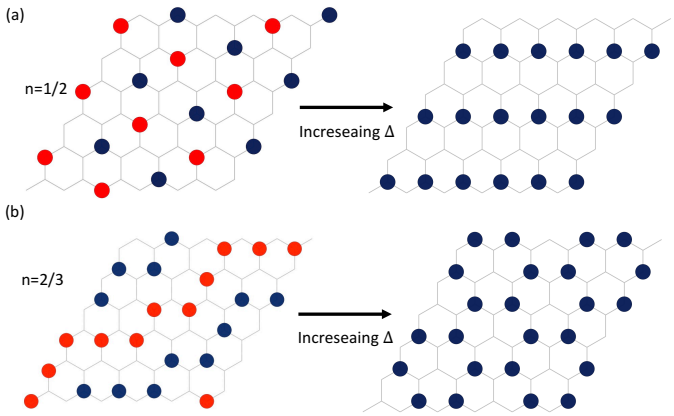

Figure 5-4: Ground state charge order at filling (a) n=1/2 with increasing charge transfer gap Δ, (b) n=2/3 with increasing charge transfer gap Δ.

lattice with $\sqrt{3} \times 2$ periodicity. This state breaks the three-fold rotational symmetry and can be viewed as the combination of the stripe states on both sublattices, each at 1/4 filling. This rectangular electron crystal is energetically favorable compared to the enlarged 2×2 honeycomb crystal at all gate screening distances. In contrast, at large Δ, the ground state becomes a simple stripe state on the triangular sublattice with lower on-site potential, as shown in Fig. 5-4. We find the critical charge transfer gap is $\Delta_c = 2(V_2 - V_3 - V_4 + 2V_6 - V_9 + V_{12} + ...)$. For $d = L_m = 9.1$ nm, $\Delta_c = 0.12\frac{e^2}{\epsilon L_m} \sim 3.8$ meV can be reached by realistic gating field. We note the critical Δ_c can be further lowered by increasing moiré wavelength.

At filling factor $n = 2/3$, the charges form a zigzag stripe order with 6×6 periodicity breaking the C_3 rotational symmetry. This zigzag-type charge configuration is energetically favored compared to a linear stripe at screening distances from $d = 1/2L_m$ to $d = 10L_m$. As Δ increases, the zigzag charge stripe transitions to the $\sqrt{3} \times \sqrt{3}$ crystal that occupies one sublattice site only, as shown in Fig. 5-4. We find the critical charge transfer gap is $\Delta_c = V_2 - V_3 - \frac{10}{3}V_4 + \frac{14}{3}V_5.... = 0.04\frac{e^2}{\epsilon L_m} \sim 1.3$ meV at $d = L_m = 9.1$ nm.

The transition between distinct electron crystals at the same filling is first-order. This should lead to a kink in the sublattice/layer charge imbalance as a function of the gating field. This prediction, which is a main result of our work, can be tested

in $MoSe_2$/hBN/$MoSe_2$ heterostructure [126], where the gating field induced charge transfer between the top and bottom layers has already been observed at relatively high temperature.

For $n = 1$, we find that even at $\Delta = 0$, the ground state is a fully sublattice polarized Mott insulating state, which spontaneously breaks the honeycomb lattice symmetry. As the two sublattice sites MX and XM have different layer weights, the Mott insulating state at n=1 develops a finite out-of-plane ferroelectric polarization, which can be switched by the electric field. The ferroelectricity driven by the Mott physics in TMD moiré systems goes beyond the conventional ferroelectricity and enables fast switching due to electronic origin [150]. For filling $n > 1$, the charge-2e trimer can be the lowest energy excitation when tuning the charge transfer gap Δ, providing a platform to design unconventional superconductivity [151].

In homobilayer WSe_2, the valence band maximum is located at K with weak interlayer tunneling amplitude and intralayer potential both on the order of 10 meV. The complex tunneling term between two layers brings further complications for the theoretical and experimental investigation of the insulating states [144, 128, 130].

In conclusion, we present a combined study of lattice relaxation, single-particle electronic structure, and ground state charge orders on the twisted homobilayer MoS_2. Unlike the previous moiré charge transfer insulator in $WSe2_2/WS_2$ heterobilayer, here out-of-plane gating field breaks C_{2y} symmetry and induces a controllable charge transfer gap. With Monte Carlo simulation, we predict additional stripe-type charge orders at fillings $n = 1/2, 2/3$ in the emergent honeycomb lattice with $\Delta = 0$. When increasing Δ, these electron crystals transit to fully sublattice polarized states. We further predict the ferroelectricity at the $n = 1$ Mott insulating state, which enables the ultrafast switching of electronic polarization. Our work demonstrates that the interplay between two moiré regions leads to the charge transfer insulator [152, 136] and serves as a platform for creating novel correlated states, such as unconventional density wave [153, 154], charge stripes [101], spin superfluid[155] and superconductivity[151].

Chapter 6

Machine learning magnetism classifiers from atomic coordinates

Part of the work described in this chapter is published as Ref. [156].

The atomic structures of materials inherently contain the necessary information for reconstructing their magnetic structures. This is because the magnetic structures arise from spontaneous symmetry breaking induced by the Coulomb interaction, wherein the atomic structures play a significant role in determining the magnitude of this interaction. However, the theoretical determination of magnetic structures is often impeded by computational resource limitations, and some existing efficient methods may lack accuracy. Nonetheless, DFT-based methods have facilitated high-throughput calculations for over 10,000 materials, creating an ideal platform for the application of machine learning techniques.

A crucial step in applying machine learning methods to materials science is finding an appropriate descriptor capable of encoding atomic structure information. Atomic structures can be simplified as a three-dimensional ball-and-stick model. To represent materials at the thermodynamic limit, a large ball-and-stick model is unnecessary. This is because materials often exhibit spatial symmetries such as translational, rotational, and inversion symmetries. By leveraging these symmetries, simplification can be achieved. If we can encode the atomic structures not only in a graph neural network (NN) but also incorporate symmetry, such that the NN model can readily

recognize the equivalence of two inputs under spatial transformations, it would provide significant benefits. This approach allows us to represent the same structure with a less complex descriptor and aids in training the model without needing augmented data to teach it about the equivalence of structures through spatial transformations.

In this chapter, we present a machine-learning model that aims to classify the magnetic structure by inputting atomic coordinates containing transition metal and rare-earth elements. By building a Euclidean equivariant neural network that preserves the crystallographic symmetry, the magnetic structure (ferromagnetic, antiferromagnetic, and non-magnetic) and magnetic propagation vector (zero or non-zero) can be predicted with an average accuracy of 77.8% and 73.6%. In particular, a 91% accuracy is reached when predicting no magnetic ordering even if the structure contains magnetic element(s). Our work represents one step forward to solving the grand challenge of full magnetic structure determination.

6.1 Introduction

As one of the most prominent quantum phenomena, the magnetism of materials encompasses a large portion of functional applications such as data storage [157], high-resolution imaging [158], spintronic devices [159], high-energy scientific instruments [160, 161], and quantum computing [162, 163]. Particular types of magnetism are also believed to be associated with unconventional quantum phases such as high-T_c and topological superconductivity [164]. Unlike small molecules where magnetic structures contain only several high-spin and low-spin configurations, spatial correlations between magnetic moments in sizeable materials constitute vast possibilities of different magnetic configurations. With infinite combinations of wavevectors, moments, and correlations lengths, magnetic materials can form a variety of structures such as antiferromagnetism [165], non-collinear magnetism, skyrmions [166], spin glass [167], and quantum spin liquids [168, 169]. Therefore, the determination of magnetic structures, either experimentally or theoretically, is crucial for materials discovery and technological progress in general.

Experimentally, the state-of-the-art neutron scattering [170] and more recently resonant X-ray scattering [171] have enabled the characterization of magnetic structures with atomic-scale resolution. However, these measurements require large-scale neutron sources or synchrotron X-ray radiation and are highly limited by capacity and beamtime availability. According to the most comprehensive database, only $\sim 1,500$ materials' magnetic structures have been identified through these experimental spectra since the 1950s [172, 173]. Therefore, without order-of-magnitude improvements of these facilities' capacity, a pure experimental exploration of magnetic materials is yet to catch up with the rapidly rising demand for materials discovery of new magnetic materials.

Theoretically, *ab initio* simulations with advanced quantum chemistry and physics methods have been successfully applied to the prediction of magnetism of small molecules [174]. However, the computational complexity of these accurate methods increases exponentially with the system size, which makes it impractical to be extended to sizeable materials beyond the nanoscale. The first-principles DFT simulations and the associated corrections provide an efficient compromise between accuracy and scalability. Although the delocalization error and the lack of static correlation may underestimate the magnetic moment and correlations [175, 176], DFT-based methods have enabled high-throughput calculations over ∼10,000 materials [177], allowing for preliminary statistical predictions of materials' properties. Even with substantial acceleration compared to experiments and wavefunction-based methods, the computational complexity of DFT calculations is still non-negligible and hinders the discovery in a huge, possibly infinitely large, parameter space of chemical compositions. Moreover, since electronic structure theory evaluates the energy for a specific electronic configuration, including the magnetic structure, the standard simulation requires traversing all configurations for a single atomic structure and determining the ground-state magnetic configuration. Thus the large number of possible magnetic configurations forms a "guessing-computing" duo; that is, guessing many possible configurations and computing them one by one. Consequently, most computational efforts are spent on irrelevant magnetic excited states rather than the true ground

states. A reliable prediction of the ground-state magnetic structure would greatly accelerate high-throughput calculation and bring us closer to achieving simulation-free materials discovery.

Given the challenges in magnetic structure determination from experiments and calculations, significant research effort has recently been dedicated to using machine learning to enhance magnetic structure determination. Some recent works combine DFT calculations with machine learning [178, 179, 180, 181], in some of which the "guessing" step in the guessing-calculating procedure is obtained with machine-learned models. For instance, machine learning has been implemented to reduce the search space of possible magnetic configurations in the "guessing" step. With this approach, the main calculation task is still carried out by the standard first-principles DFT calculations. Some other works are based on model Hamiltonians [182, 183], mostly classical spin models, and use machine learning methods to fit the free parameters in such a model, such as from experimental data that contain the spin information. Even so, the direct prediction of magnetic structure from the more direct atomic structure, aka replacing the "computing" step, is still challenging.

A full description of magnetism[184] can be nontrivial. In this work, we focus on two different descriptions that use relatively few variables: magnetic order labels and propagation vectors. Magnetic ordering labels (e.g. ferromagnetic (FM) and antiferromagnetic (AFM)) are helpful because they summarize the complexity of magnetic structures into simple classes that are application relevant. A propagation vector is a vector in reciprocal space that describes symmetry breaking due to the presence of magnetic order. A non-zero propagation vector is one indicator for a more involved magnetic structure beyond the FM, AFM, and NM ternary classification. While these descriptions are expressive, they are not comprehensive and we leave more complex descriptions of magnetic order to future work.

We build an ML-based classifier that predicts the magnetic order under a ternary classification (FM/FiM: ferromagnetic/ferrimagnetic, AFM: antiferromagnetic, NM: non-magnetic), and also outputs whether the propagation vector is zero or non-zero. We choose these two in our prediction as a start, in doing so, we acquire partial but

valuable information that may accelerate full magnetic structure determination. Our work differs from some prior efforts in that, after training, the predictive model can directly output the magnetic order and propagation vector with only atomic structure as the input, without requiring any further first-principles calculations. This is realized by applying the Euclidean neural network (E(3)NN), which preserves 3D rotation, inversion, and translation symmetry in the atomic structures so that high accuracy is reached without data augmentation [13]. The accuracy in the test set is about 78% for magnetic order prediction and about 74% for propagation vector prediction. The accuracy varies when the material of interest contains different elements or belongs to different space groups, as we will elaborate in the results section. Since the magnetic order and propagation vector represent two different pieces of magnetic structure information, they are trained separately with different neural network architectures and training data from the Materials Project and MAGNDATA [172, 173] databases, respectively. The atomic structure inputs for magnetic order classifiers are from Materials Project, magnetic order labels are obtained using pymatgen's magnetism analyzer given structures with atoms decorated with DFT calculated magnetic moments as inputs. Both structures and propagation vectors for propagation vector classifiers are from MAGNDATA.

6.2 Methodology

6.2.1 Data assembly

In order to train the magnetism classifier, we assemble a dataset containing both structure and magnetic order information from the Materials Project [177]. We query structures that contain at least one magnetic element, including transition metals (Sc, Ti, V, Cr, Mn, Fe, Co, Ni, Cu, Y, Nb, Mo, Ru, Rh, Re, Os, Ir, Pt), lanthanides (Ce, Pr, Nd, Sm, Eu, Gd, Tb, Dy, Ho, Er, Tm, Yb), and/or actinides (Th, U, Np, Pu); however, a material containing a magnetic element does not necessarily host magnetic order. Our search is restricted to calculations using the generalized gradient

approximation with Hubbard interaction (GGA+U), which is suitable for magnetic structure calculations and leads to a total of 34,856 structures[1], among which 30,584 are FiM/FM, 1,790 are AFM and 2,482 are NM. The magnetic order labels are derived using the Python-based pymatgen analysis code [185] and through the use of a CollinearMagneticStructureAnalyzer class. The CollinearMagneticStructureAnalyzer class uses the DFT calculated magnetic moments and total magnetization (the absolute value of the sum of individual magnetic moments) to assign one of the following labels: FM if the total magnetization is greater than zero and all magnetic moments have the same sign, FiM if the total magnetization is greater than zero, AFM if total magnetic moment is zero and max absolute magnetic moment greater than zero, or NM magnetic order if total and max magnetic moment is zero. We then train 20 classifiers with different initial weights, each optimized on a randomly selected subset of 6,086 structures with a AFM:FM:NM ratio of 5:6:6. The size of each class is kept comparable in each selected subset to mitigate the training bias toward nonmagnetic examples, since there is a substantially larger fraction of FM/FiM structures in the total dataset and only 1,790 AFM examples. Each subset of 6,086 materials is divided among training, validation, and test sets with a ratio of 0.8:0.1:0.1. Note that we find this further improves our model's ability to differentiate between AFM and FM/FiM classes, and the smaller data size helps reduce the overall training time.

Magnetic materials may host more complex magnetic structures beyond AFM/FiM which are described by other non-zero magnetic propagation vectors. In order to capture this complexity, we further train a binary classifier of the propagation vector magnitude (zero or non-zero). The zero propagation vector represents the prototypical FM order, while the non-zero propagation vector represents AFM/FiM orders and beyond. We obtain the structure and magnetic propagation vector information from the MAGNDATA database [172, 173], which to date contains the comprehensive experimentally-determined magnetic structures of 1,562 compounds. The data used in this study were restricted to commensurate magnetic structures, as incommen-

[1]Due to recent updates in the Materials Project, if querying in the latest pymatgen version with the same magnetic elements, the number of total structures may change. Our models are trained and tested based on pymatgen version 2022.0.8, with 34,856 total structures after querying.

surate magnetic structures always have non-zero propagation vectors. This yielded 1,134 total structures, of which 552 (582) have zero (non-zero) propagation vectors. We again train 20 classifiers with different initial weights, independently dividing the 1,134 total structures at random among training, validation, and test sets with a ratio of 0.8:0.1:0.1 for each model. To link the propagation vector classification with that of magnetic order, we show the statistics of structures appearing in the propagation vector classification datasets in Fig. 6-1. Some structures' magnetic orders are unknown to pymatgen's magnetism analyzer which we use for determining magnetic order, so those are not included in the figure. Most structures with nonzero propagation vectors are AFM, some are FiM, and none are FM or NM, as expected. The propagation vector classifier can further divide AFM and FiM classes into subclasses with zero/nonzero propagation vectors, giving us more information about the magnetic structure of a material.

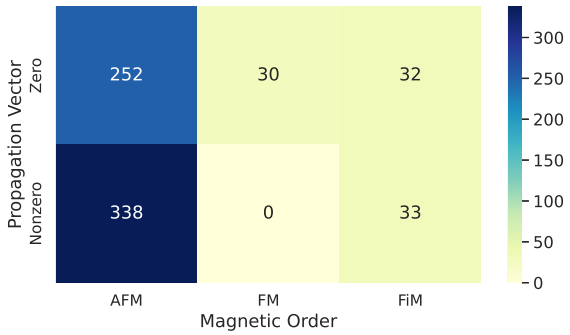

Figure 6-1: Number of examples with zero and nonzero propagation vector in each magnetic ordering class.

6.2.2 Model architecture

The architecture of both classifiers is based on Euclidean Neural Networks (E(3)NNs) [13], a class of 3D Euclidean group (E(3))-equivariant neural networks. Any space group that describes the crystal geometric symmetries in three dimensions is a subgroup of E(3), and thus E(3)NNs preserve all geometric symmetries of the crystal structure, which removes the need for extensive data augmentation needed to consider arbitrary translations or rotations of the input structures. The neural network

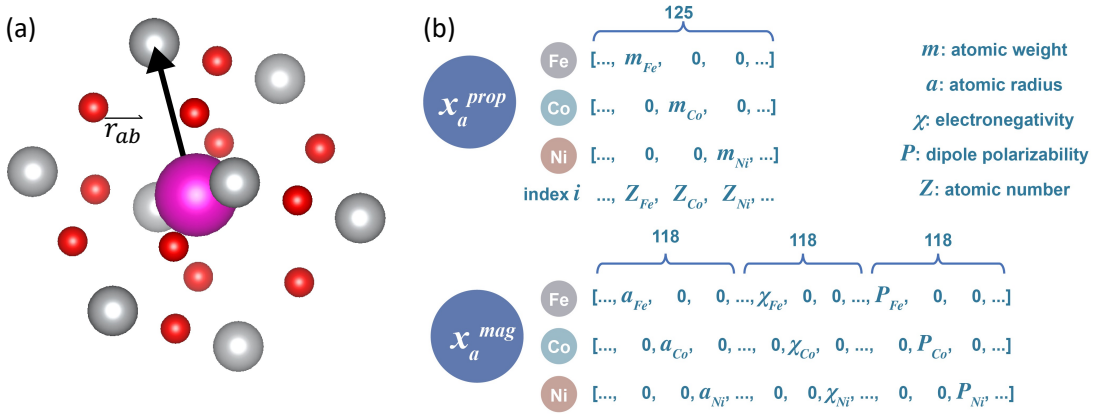

Figure 6-2: **Illustration of input data structures.** (a) A representative periodic graph constructed from the crystal structure in the neighborhood of a given atom. Each atom (node) carries a feature vector x_a, and each edge connecting node a to a neighboring node b is characterized by the relative distance vector $\vec{r}_{ab}$. (b) Each atom is represented by a node in the periodic graph, and the atom type is expressed by a property-weighted one-hot feature vector. The top row shows a set of representative feature vectors used for the propagation vector classifier. Each is an array of 125 scalars, with the Z-th scalar being the atomic mass in amu (atomic mass unit), where Z denotes the atomic number. The bottom row shows a set of representative feature vectors used for the magnetism classifier. Each is an array of 3×118 scalars, formed by concatenating three arrays of 118 scalars which encode the atomic radius(pm), electronegativity on a Pauling scale, and dipole polarizability(a.u.) of a given atom employing the same property-weighted one-hot encoding scheme used for the propagation vector classifier input.

inputs consist of a material's crystal structure and one or more descriptors of each constituent atom. Specifically, the unit cell of each example is first converted into a periodic graph, where each node a represents an atom described by a feature vector x_a. A single convolutional layer operates on the input x_a and the radial distance vectors $\vec{r}_{ab}$ between atoms a and b in the neighborhood of a up to a radial cutoff $r_{\max} = 5$Å, as shown in Fig. 6-2a. The feature vector x_a associated with each node is constructed by a property-weighted one-hot encoding of selected atomic properties, illustrated in Fig. 6-2b. For the propagation vector classifier, each feature vector is an array of 125 scalars, with the Z-th scalar being the atomic mass in amu (atomic mass units), where Z denotes the atomic number. Additional properties can be considered by simple concatenation of several such feature vectors, each weighted by the

appropriate value of the property of interest. For example, each of the input feature vectors used for the magnetism classifier is an array of 3×118 scalars, formed by concatenating three arrays of 118 scalars that encode the atomic radius (pm), electronegativity on a Pauling scale, and dipole polarizability (a.u.). The architecture of both classifiers consists of three principal parts, as shown in Fig. 6-3. First, the input feature vectors are passed to an embedding layer for dimensionality reduction. The E(3)NN layers are then applied to the resulting hidden state and consist of alternating convolution and gated block operations (dashed rounded rectangle). The convolution signifies the tensor product between input feature vectors and symmetry-constrained convolutional kernels. The convolution step is implemented as:

$$f'_a = \frac{1}{\sqrt{z}} \sum_{b;|\vec{r}_{ab}|<r_{max}} f_b \otimes(h(\|\vec{r}_{ab}\|))\, Y(\vec{r}_{ab}/\|\vec{r}_{ab}\|)$$

where the node f'_a is the output node for the atom a. The output node is the sum of the tensor product between the input node of a neighborhood atom f_b and the neural network h. Y is the spherical harmonics, which serve as basis functions that enable the mapping of the relative distances to the weights of the tensor product. z is the average degree of the nodes, that is the number of atoms surrounding the center atom. The prefactor $1/\sqrt{z}$ adjusts the different number of neighborhoods. The gated block step denotes a gated rotation-equivariant nonlinearity as described in Ref. [186]. The gate activation is a direct sum of two sets of irreducible representations. Mathematically, this can be written as:

$$\left(\bigoplus_i \phi_i(x_i)\right) \oplus \left(\bigoplus_{l,m} \phi_j(g_{lm}) y_j\right)$$

The first set of the irreducible representation is the scalars x_i passing through activation functions ϕ_i. The second set is the gated scalars g_{lm} passing through activation functions ϕ_j and multiplied by the scalars y_j. The number of functions in the list should match the number of irrep groups in irreps gates.

Finally, the E(3)NN output is converted to a class label by first adding together

the output vectors for all atoms in a given material, and then applying a final non-linear activation. For the propagation vector classifier, the output is a sigmoid-activated scalar, while for the magnetism classifier, it is a softmax-activated array of three scalars giving the probability of exhibiting one of three magnetic orders (AFM, FM/FiM, NM).

6.3 Results Analysis

To quantify the consistency of predictions made by the magnetism and propagation vector classifiers, we independently train 20 models for each task using randomly drawn data subsets as described in Section 6.2.1 above. For the magnetic order classification, we show the test set accuracies of the 20 models in the left panel of Fig. 6.3, which range from 73.8% to 80.7% and have a mean accuracy of 77.8%. For the propagation vector classification, the test accuracies obtained from 20 models are displayed in the right panel, ranging from 68.1% to 85.0% with a mean of 73.6%, the thresholds of this binary classification are chosen separately for each model to guarantee maximal accuracy. In Table 6.3 and 6.3, we summarize the averaged precision, recall, and F1 scores over all trained models for the two tasks, respectively. We note that the larger spread of accuracies in propagation vector classification can possibly be attributed to fewer training examples (1,134 total structures taken 907 at a time for training), which are not sufficient for our model to learn all complex connections between crystal structures and propagation vectors. Besides, it may also suggest that the propagation vector contains a rich strong correlation effect that cannot be fully characterized by only atomic structures. More details about the performance of both classifiers are apparent in the confusion matrices (CM) shown in Fig. 6-4. For the magnetic order classifier, we observe an excellent separation of the NM class from the two magnetic classes (Fig. 6-4(a)). Since all calculations are performed at $T = 0$K, we believe that this non-magnetic separation is important in rapidly screening and excluding materials that do not host any magnetism, without having to experimentally cool down to the lowest measurable temperature. More ambiguities appear between classifications

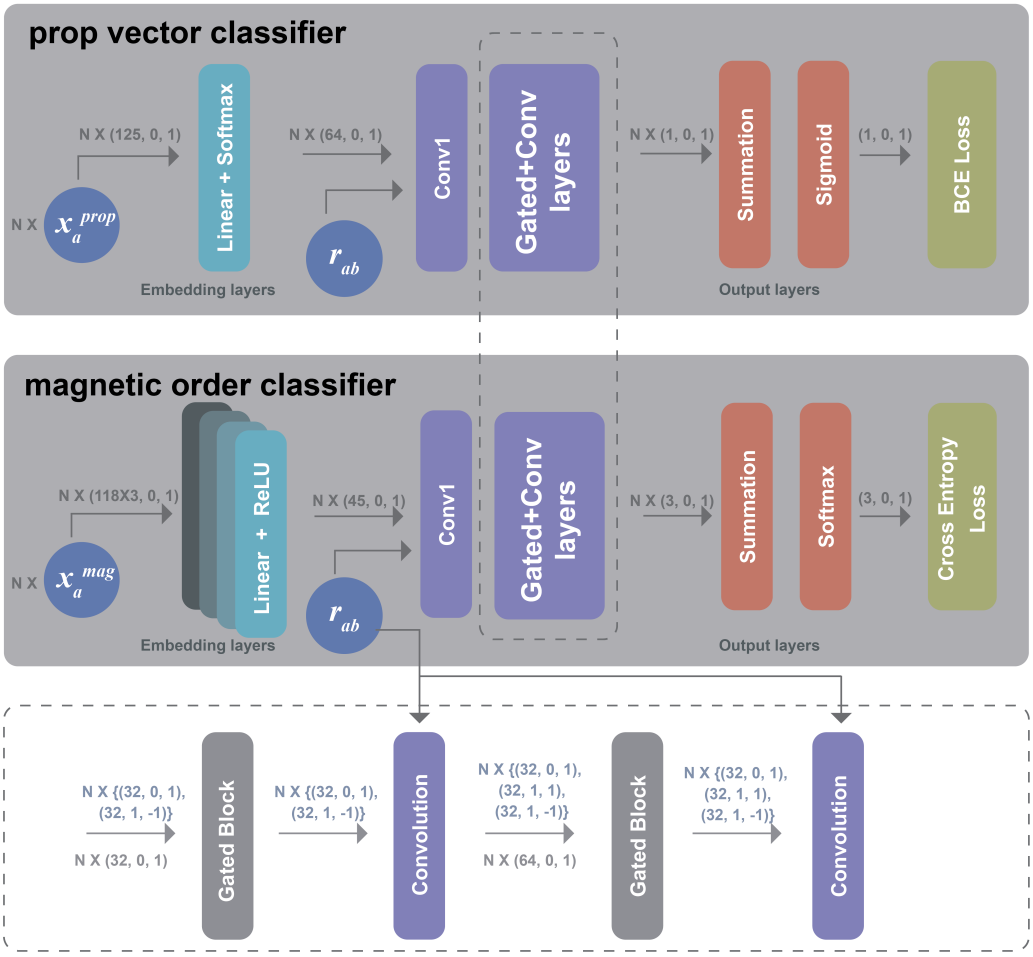

Figure 6-3: **Illustration of the neural network architectures for propagation vector (top block) and magnetic order classification (middle block)**. The models each consist of three principal layers: embedding layers, convolution and gated layers based on E(3)NN, and the output layers which generate the predicted classes. The convolution and gated layers of both models share the same architecture (detailed architecture shown in the bottom block). Even though the loss functions and embedding layers are optimized separately, by adopting this approach, one atomic structure can lead to a simultaneous prediction of both magnetic order and propagation vector.

of the AFM and FM/FiM classes, where magnetic orders exist in both classes but in different formats. This is possibly due to the difficulty of distinguishing between FiM and AFM from atomic structures, and the energy difference between magnetic structures with AFM and FM/FiM orders can be small. The overall CM suggests a

good capability of recognizing potential magnetic orders but a slightly weaker ability to identify the exact class. Fig. 6-4(b) depicts the CM for the propagation vector classifier. Although the overall performance is hard to be considered satisfactory, as already mentioned above, the model has better precision versus the recall for the non-zero propagation vector.

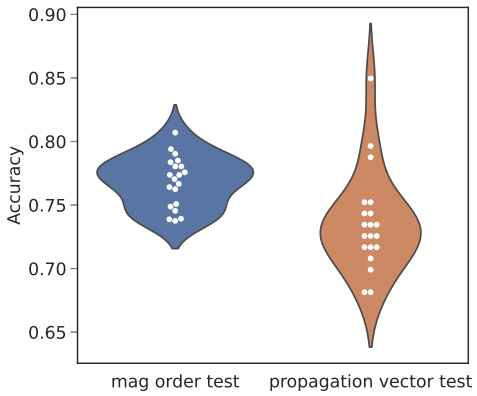

figurePrediction accuracies in test sets for magnetic orders (left) and propagation vectors (right) collected from 20 independently trained models.

class	precision	recall	f1-score
NM	0.91	0.92	0.91
AFM	0.70	0.68	0.69
FM	0.68	0.70	0.69

tableAveraged metrics of the 20 magnetic order classification models in test sets.

class	precision	recall	f1-score
Zero	0.70	0.83	0.76
Non-zero	0.79	0.64	0.71

tableAveraged metrics of the 20 propagation vector classification models in test sets.

To analyze the performance of the magnetism classifier in more detail, we visualize the element-specific test set accuracies in Fig. 6-5(a). We observe the highest classification accuracy on examples containing elements commonly found in ferromagnetic materials, such as Fe, Co, and Ni, with accuracies exceeding 76%. In addition, materials containing certain rare earth elements such as Tb, Dy, and Ho are classified with similar levels of accuracy.

To further understand varying accuracies across different elements from the aspect of data abundances, we show the appearance frequency of each element inside the training set in Figs. 6-5(b). The correlations between high accuracies of some elements and large numbers of training samples containing those elements, including Mn, Fe, Co, Ni and Cu, can be readily found. On the other hand, the elements with lower prediction accuracies are typically less common, such as Ga, Lu, Re, and Sm.

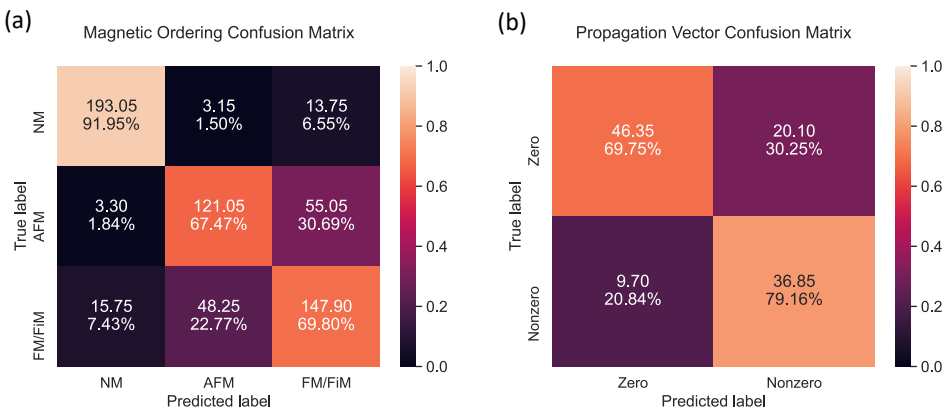

Figure 6-4: Confusion matrices for prediction results on test sets of (a) magnetic orders and (b) propagation vectors. The values are averaged over 20 models, the color represents the percentage.

However, it is worth highlighting the great performance of some rare earth elements (e.g. Tb, Dy, and Ho) given the small number of training samples, this is because they usually coexist with other abundant elements, for example, 65.9% of structures that contain Tb, Dy and Ho also contain elements Mn, Fe, Mo, Co, Ni.

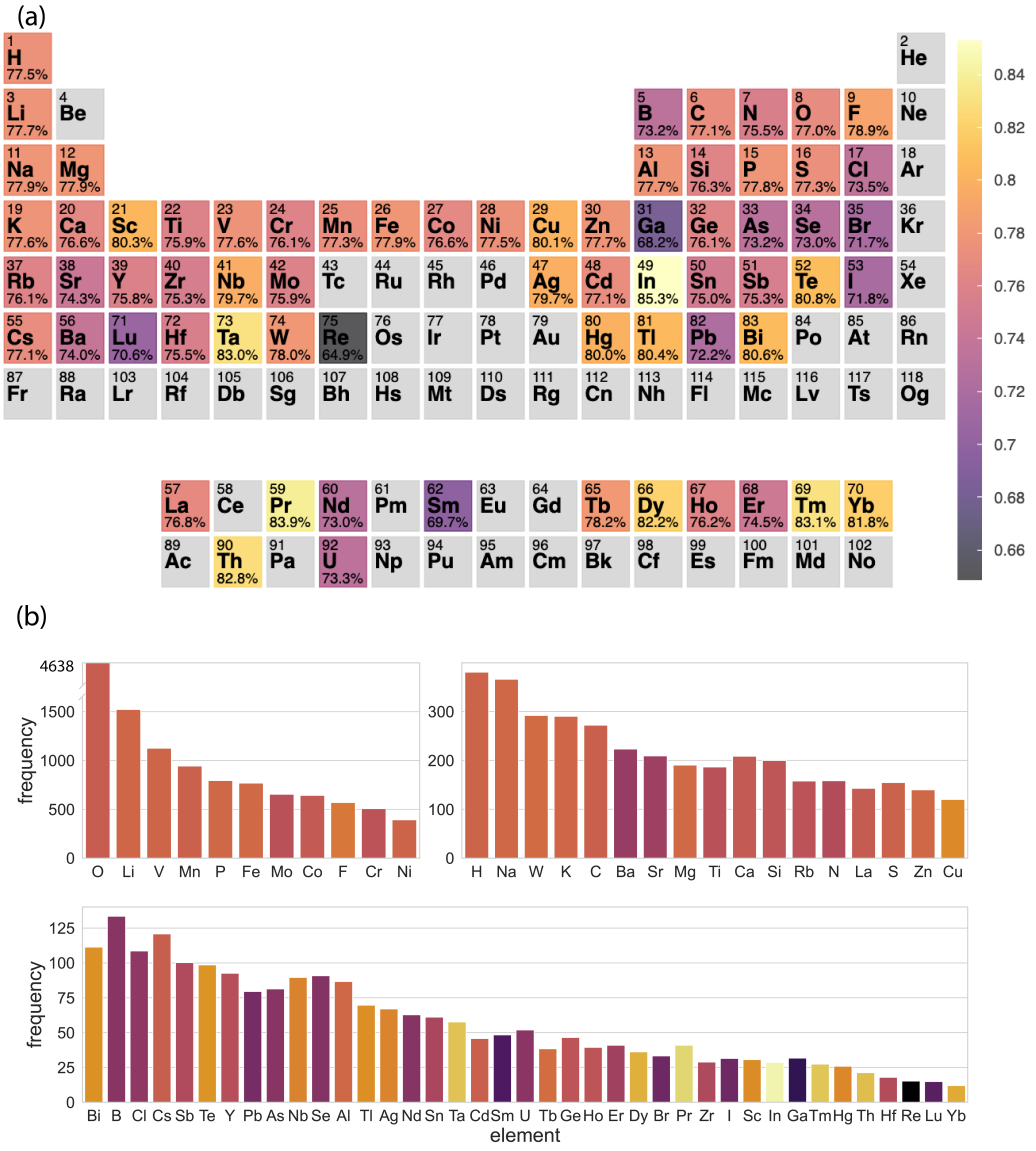

Figure 6-5: Performance on the testing set and sample statistics of the training set for the magnetic order predictions. (a) The testing accuracy of magnetic order classification per element shown in a color map on a periodic table, grey color indicates the element is absent or insufficient (mean frequency less than 1) in testing sets. (b) Histogram of frequency each element appears in the training sets. The following elements are greyed out due to their absences or insufficiency in test compounds: Pd, Th, Re, Yb, Ce, Eu, Os, Ir, Pt, Rh, Ru, and Np.

Similar connections between the classification accuracy and the number of training

samples can be made for different crystal systems. In Fig. 6-6(a), we show the number of examples of each magnetic order class as a function of the crystal system of the corresponding structure. Fig. 6-6(b) indicates that higher appearance frequency in training data in general leads to higher classification accuracy in test data. Such relationships suggest that the predictions made by our model is based on not only the atomic species but also their coordinates and the crystal structure.

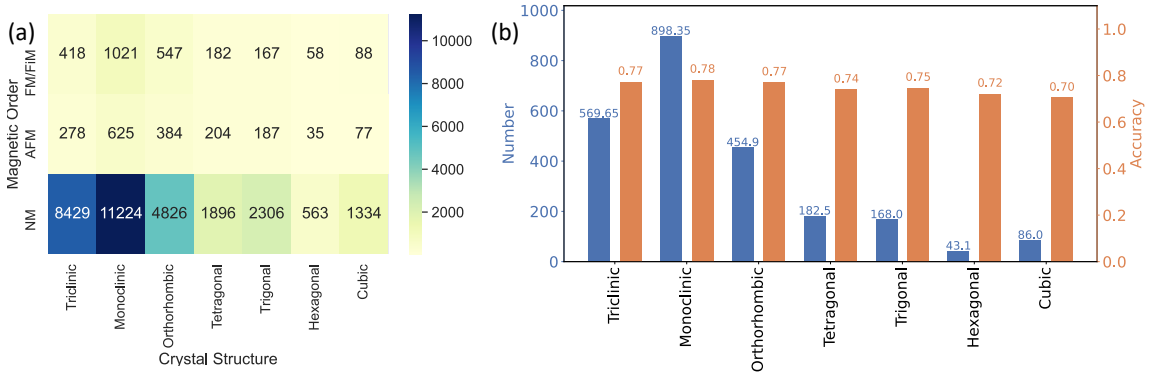

Figure 6-6: (a) Number of examples in each magnetic order class as a function of the crystal system. (b) Comparison between the number of training samples and testing classification accuracy for each crystal system, the values are averaged over 20 independent models.

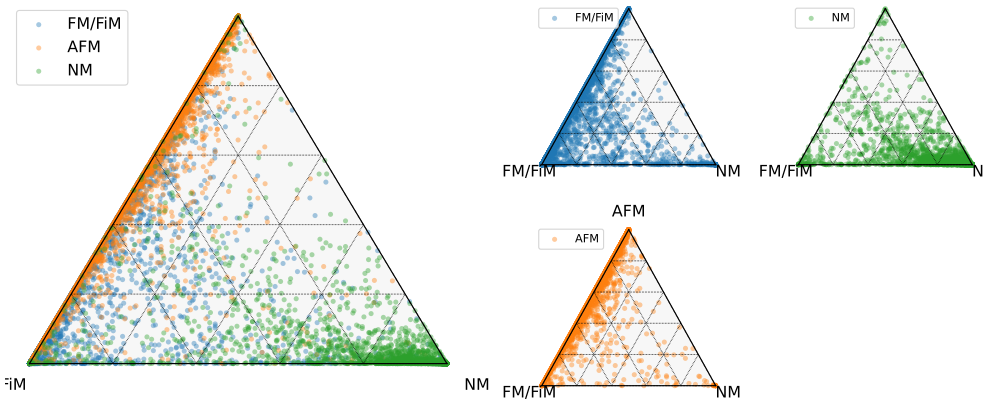

Figure 6-7: outputs of the neural network with testing data as inputs shown in ternary plots, points represent 3-element vector outputs and are colored by their true label: FM/FiM, AFM and NM.

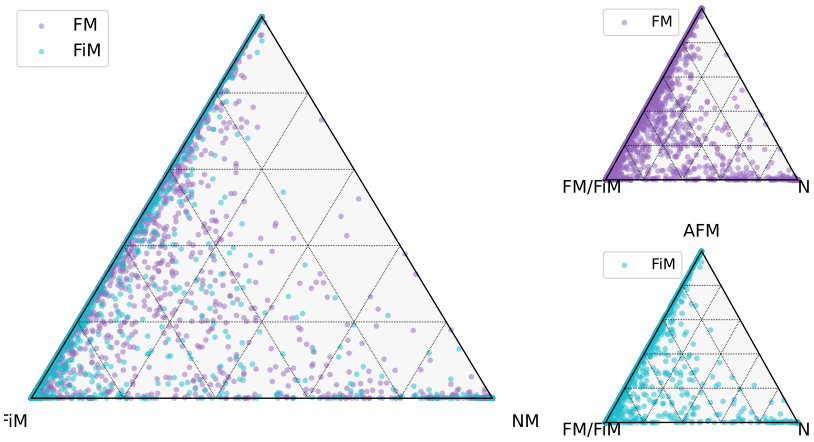

Figure 6-8: outputs of the neural network with testing data as inputs shown in ternary plots, points represent 3-element vector outputs and are colored by their true label: FM and FiM data.

As mentioned above, our magnetic order classifiers show excellent separation between magnetic (including FM/FiM and AFM) and non-magnetic orders, but more ambiguities between the classification of the AFM and FM/FiM classes. To discuss this further, particularly to see whether the FiM is preferably assigned to the FM or AFM class, Fig. 6-7 and 6-8 shows the 3-element-vector outputs of the neural network before taking argmax function in a ternary form, with testing data as inputs. The closer a point is to a corner of the triangle, the more likely the predicted label is the corresponding class of that corner. We color the points with their true label to show the distinction. Fig. 6-7 explains that the testing outputs with true labels of AFM and FM/FiM distribute along the edge connecting AFM and FM/FiM classes and do not distinctly separate from each other, which causes ambiguities in the classification. The data with the true label of NM stay close to the NM corner and away from the other two classes. Fig. 6-8 suggests that our choice to consider FM and FiM order jointly in the class FM/FiM is reasonable, since the distribution of FM and FiM in the ternary plots is similar, and our classifiers treat atomic structures with FM and FiM orders similarly.

6.4 Discussion and Future Directions

In this chapter, we present a machine-learning-based magnetism classifier that takes crystal structure as input and basic magnetic structure information as output. Despite extensive training, it seems that the prediction of magnetism hits a performance barrier, except for the non-magnetic class. There are two potential factors contributing to this barrier. Firstly, the magnetic orders represent a coarse-grained classification of magnetic structures. Utilizing them as label vectors for the neural network model may not provide sufficient information for effective learning, as the E(3)NN structures possess the potential to employ complete magnetic structures (including magnetic moments of each atom) as label vectors during training, even though we can still focus solely on predicting magnetic orders determined by the net magnetic moments in the end. Secondly, the input feature vectors encompass the crystal structures and certain atomic properties, which may not be comprehensive enough. This brings up the fundamental query on magnetic representation: besides the atomic species, the interatomic bonding, and the crystal symmetries, there might be some additional information still at large that can capture the essence of magnetism. We anticipate that finding proper magnetic representation can significantly boost the machine learning on magnetic materials research and shed light on strongly correlated electronic materials in general.

Except for the limitation in our magnetic classification models, the E(3)NN itself is a powerful tool for machine learning tasks in materials science. Nevertheless, the current configuration of E(3)NN lacks the ability to represent quantum effects. In a graph neural network, each node corresponds to a vector that can encode atomic properties or classical magnetic moments, resembling the structure of a classical magnetic model. However, the E(3)NN model cannot adequately capture the superposition states present in quantum magnetism, exceeding its encoding capacity. Future developments that enable the representation or approximation of quantum states within the framework of E(3)NN would be a significant advancement. This integration would combine the benefits of symmetry equivalence and the ability to represent

quantum states within the same model, leading to a general machine-learning model to study quantum many-body systems. Furthermore, this development would play a crucial role in utilizing machine learning techniques to probe entanglement and detect symmetry-breaking orders, this chapter serves as a primary example of this overarching objective.

Chapter 7

Conclusions and future work

In this thesis, we discussed various topics regarding using spectroscopies and machine learning as tools, to probe entanglement and symmetry breaking orders in many-body quantum systems. This chapter aims to summarize the presented work and provide insights into potential future efforts.

In Chapter. 3, we proposed a new X-ray technique to measure four-point two-particle correlations. The proposed method is based on resonant inelastic X-ray scattering (RIXS), and requires either one of the two conditions in addition to the current RIXS standard, the first is the high accuracy of RIXS intensities and precise resolution in the wave vector of incoming and outgoing X-ray photons, that allows to capture the minor term in RIXS cross-section which depends on the incoming photon momentum. The second condition is to find materials with valid core levels of higher orbitals, that have a relatively large hopping term in core levels, indicating high mobility of the core hole. It induces a larger contribution of four-point correlations in RIXS intensities to be captured within current RIXS precision. The proposal suggests the great potential of advanced X-ray techniques and provides motivations for future upgrades in RIXS beamlines.

Theoretically, we define measurable quantities based on the full set of four-point two-particle correlations and aim to probe and quantify quantum correlations and entanglement within the accessibility of spectroscopies. Most spectroscopies can only measure correlation functions with few particles and few indices (points), and entan-

glement is hard to be quantified with limited access to correlations. The quantities we define contain only one-particle and two-particle correlations, which are potentially accessible through spectroscopies, and we have shown that using the RIXS techniques we presented, combined with the spin-resolved ARPES, we can almost measure the defined quantities. The quantities we define have two explanations, (1) It is a measure of quantum correlations, measuring how much the system deviates from the Slater determinant approximation; (2) It is a multiparticle entanglement witness, we can derive a series of upper bounds for n-particle entangled states, and when the quantities exceeding those upper bounds, they witness $n+1$-particle entanglement. We summarize the future theoretical directions as follows: (1) We have shown the upper bounds of $\mathrm{Tr}[O^2]$ for a n-particle entangled system growing quadratically with n. There are some states carrying long-range entanglement, that remain inseparable even at thermodynamic limits, like the Kitaev model. It will be interesting to test whether $\mathrm{Tr}[O^2]$ grows quadratically with system size in the solvable Kitaev model, and this quadratic relation with system size can potentially serve as a signature of long-range entangled states. (2) The bigger theoretical question is to quantify entanglement with limited access to correlations, and the limitation originates from the accessibility of spectroscopies, we can only expect to measure few-body few-point correlations using spectroscopies, the term "few" refers to values that do not increase with the system size. Future theoretical studies are required to provide a formal pathway to define entanglement measures that only contain n-particle correlations, with a finite integer number n.

Lastly, there are other spectroscopic methods carrying the potential to measure higher-order correlations considering higher perturbation in their cross section, one example is neutron scattering. In the following, we show some preliminary results.

The cross section of neutron scattering is

$$\omega = \frac{2\pi}{\hbar} \sum_{\mathbf{f}} \left| \langle \mathbf{f}| \, H' \, |\mathbf{i}\rangle + \sum_{\mathbf{n}} \frac{\langle \mathbf{f}| \, H' \, |\mathbf{n}\rangle \, \langle \mathbf{n}| \, H' \, |\mathbf{i}\rangle}{E_{\mathbf{i}} - E_{\mathbf{n}}} \right|^2 \delta(E_{\mathbf{f}} - E_{\mathbf{i}}). \tag{7.1}$$

It is based on Fermi's golden rule, and we here include the second-order term that

contributes to the transition rate of this process. This second-order term refers to the process of the neutron scattering twice with the probed system, most previous literature only considers the first-order term, referring to the neutron scattering a single time with the system. Within the formula, H' is the interaction Hamiltonian between the system and the neutron, the initial state $|\mathbf{i}\rangle = |i, k_i, \sigma_i\rangle$, the intermediate states $|\mathbf{n}\rangle = |n, k_n, \sigma_n\rangle$, and the final states $|\mathbf{f}\rangle = |f, k_f, \sigma_f\rangle$, the initial and final energies include both the system energies and the neutron energies $E_\mathbf{i} = E_i + \omega_{k_i}, E_\mathbf{n} = E_n + \omega_{k_n}, E_\mathbf{f} = E_f + \omega_{k_f}$. The summation of $\mathbf{f}$ here is actually only over f, σ_f, because k_f is fixed here, but for $\mathbf{n}$, it also sums over k_n. The leading order except the linear order is the crossing term between linear order and second order, thus leading to a three-mode correlation.We denote this part as ω_{12}

$$\omega_{12} = \frac{4\pi}{\hbar} \sum_{\mathbf{f}} \sum_{\mathbf{n}} \left| \langle \mathbf{i}| H' |\mathbf{f}\rangle \frac{\langle \mathbf{f}| H' |\mathbf{n}\rangle \langle \mathbf{n}| H' |\mathbf{i}\rangle}{E_\mathbf{i} - E_\mathbf{n}} \right| \delta(E_\mathbf{f} - E_\mathbf{i}) \tag{7.2}$$

where

$$\langle \mathbf{f}| H' |\mathbf{i}\rangle = \langle f, k_f, \sigma_f| H' |i, k_i, \sigma_i\rangle = -\frac{8\pi\gamma\mu_B\mu_N}{L^3} \langle \sigma_f, f| \vec{\sigma}_N \cdot \vec{M}_\perp(Q) |\sigma_i, i\rangle \tag{7.3}$$

where $Q = k_i - k_f$ and $M_\perp(Q) = M(Q) - \frac{(Q \cdot M(Q))Q}{Q^2}, M(Q) = \sum_j e^{iQ\cdot r_j}(s_j + \frac{i}{Q^2}(k_{e,j} \times Q))$. If assuming unpolarized neutron, $p(\sigma_i) = 1/2, \sigma_i \in \{[1,0]^T, [0,1]^T\}$, and assuming the detector can not distinguish between σ_f, so we need to take a sum of σ_f, then ω_{12} is

$$\begin{aligned}
\omega_{12} &= \frac{2\pi}{\hbar} \sum_{\mathbf{f}} \sum_{\mathbf{n}} (\langle \mathbf{i}| H' |\mathbf{f}\rangle \frac{\langle \mathbf{f}| H' |\mathbf{n}\rangle \langle \mathbf{n}| H' |\mathbf{i}\rangle}{E_\mathbf{i} - E_\mathbf{n}} + \frac{\langle \mathbf{i}| H' |\mathbf{n}\rangle \langle \mathbf{n}| H' |\mathbf{f}\rangle}{E_\mathbf{i} - E_\mathbf{n}^\dagger} \langle \mathbf{f}| H' |\mathbf{i}\rangle) \delta(E_\mathbf{f} - E_\mathbf{i}) \\
&= \frac{2\pi}{\hbar} \sum_{\sigma_i} \sum_{a,b,c,d=1}^{3} p(\sigma_i) \langle \sigma_i| \sigma^a \sigma^b \sigma^c |\sigma_i\rangle \\
&\times \sum_f \sum_n \sum_{k_n} (\langle i| M_\perp^a(-Q) |f\rangle \frac{\langle f| M_\perp^b(k_n - k_f) |n\rangle \langle n| M_\perp^c(k_i - k_n) |i\rangle}{E_\mathbf{i} - E_\mathbf{n}} \\
&+ \frac{\langle i| M_\perp^a(k_n - k_i) |n\rangle \langle n| M_\perp^b(k_f - k_n) |f\rangle}{E_\mathbf{i} - E_\mathbf{n}^\dagger} \langle f| M_\perp^c(Q) |i\rangle) \delta(E_\mathbf{f} - E_\mathbf{i})
\end{aligned} \tag{7.4}$$

To get a nonzero $\sum_{\sigma_i} p(\sigma_i) \langle\sigma_i| \sigma^a\sigma^b\sigma^c |\sigma_i\rangle$, we need to have $\sigma^a\sigma^b\sigma^c \propto \sigma^0$, the only possibilities are when a, b, c are in some arrangement of $1, 2, 3$, we have $\sigma^a\sigma^b\sigma^c = i\epsilon_{abc}$ and $\epsilon_{abc}A^aB^bC^c = A \cdot (B \times C)$. Finally, we derived

$$\omega_{12} = \frac{4\pi}{\hbar} \sum_f \sum_n \sum_{k_n} |\frac{\vec{M}_{if}(-Q) \cdot (\vec{M}_{fn}(k_n - k_f) \times \vec{M}_{ni}(k_i - k_n))}{E_i - E_n - i\Gamma_n + \omega_i - \omega_n}|\delta(E_f - E_i + \omega_f - \omega_i) \tag{7.5}$$

where $M_{mn} = \langle m| M |n\rangle$.

We have derived that the next perturbation term of high-order neutron scattering refers to three-spin correlations. If the system has time-reversal symmetry, $\mathcal{T}\vec{M}\mathcal{T}^{-1} = -\vec{M}$, but the odd term does not cancel here due to the absolute norms in the expression of transition rate, so this term remains nonzero. The application of high-order neutron scattering is another promising direction in advanced spectral techniques.

In Chapter. 4 and 5, we predicted symmetry breaking orders in two-dimensional materials and targeted identified observable characteristics that can be directly visualized through STM. The core idea is that while order parameters are typically connected to measurable correlations through spectroscopy and we can target the symmetry breaking orders by analyzing correlation functions, here we aim to directly visualize symmetry breaking orders via STM density profiles, avoiding further data analysis. To achieve this direct visualization of symmetry breaking orders, specific conditions are necessary, and we present two examples. In Chapter. 4, the ferroelectric and nematic states originated from valley symmetry breaking become observable due to the localized bound states near defects. In Chapter. 5, the enlarged superlattice in TMD moiré systems has lattice vectors on the order of 10 angstroms, enabling the direct observation of charge orders on the lattice scale within STM's spatial resolution. These examples underscore how defects facilitate local probing of symmetry-breaking orders, and how the twisted bilayer systems can be both highly tunable and enable spatial observations that are challenging in conventional two-dimensional materials.

In Chapter. 6, we trained a machine-learning-based magnetism classifier that takes crystal structure as input and basic magnetic structure information as out-

put. We have discussed the potential direction of representing variational quantum states within the framework of E(3)NN in Sec. 6.4.

Appendix A

Appendices of Chapter 3

A.1 Perturbation of mobile core-hole

We provide details about how Eq. 3.5 is derived. Expand the intermediate state following the expansion in Eq. 3.3 as

$$\begin{aligned}\int d\Delta\omega\ I\left(k_{\text{in}}, k_s, \omega_{\text{in}}, \Delta\omega\right) &= \sum_f \left|\langle\Psi|f\rangle\right|^2 \\ =&\frac{1}{N^2}\sum_{m_1,m_2,m_3,m_4}\sum_{N_1,N_2} e^{ik_s\cdot(r_{m_2}-r_{m_3})-ik_{\text{in}}\cdot(r_{m_1}-r_{m_4})}\left\langle\Psi_0\right| D^\dagger_{m_1,e_i}\left|N_1\right\rangle\left(\frac{1}{\Delta-E^{(0)}_{N_1}}+\frac{E^{(1)}_{N_1}}{(\Delta-E^{(0)}_{N_1})^2}\right) \\ &\times\left\langle N_1\right| D_{m_2,e_f} D^\dagger_{m_3,e_f}\left|N_2\right\rangle\left(\frac{1}{\Delta-E^{(0)}_{N_2}}+\frac{E^{(1)}_{N_2}}{(\Delta-E^{(0)}_{N_2})^2}\right)\left\langle N_2\right| D_{m_4,e_i}\left|\Psi_0\right\rangle.\end{aligned} \tag{A.1}$$

Further integrating over ω_{in} and in the ultrashort core-hole lifetime condition, because $\Gamma \gg E_N^{(0)}$, we take the approximation that $E_{N_1}^{(0)} - E_{N_2}^{(0)} + 2\Gamma i \simeq 2\Gamma i$ in the denominators

$$
\begin{aligned}
&I(k_{\text{in}}, k_s) = \int d\omega_{\text{in}} \int d\Delta\omega I(k_{\text{in}}, k_s, \omega_{\text{in}}, \Delta\omega) \\
=&\frac{1}{N^2} \sum_{m_1,m_2,m_3,m_4} \sum_{N_1,N_2} e^{ik_s\cdot(r_{m_2}-r_{m_3})-ik_{\text{in}}\cdot(r_{m_1}-r_{m_4})} \left\langle \Psi_0 \right| D^\dagger_{m_1,e_i} \left| N_1 \right\rangle \left\langle N_1 \right| D_{m_2,e_f} D^\dagger_{m_3,e_f} \left| N_2 \right\rangle \\
&\left\langle N_2 \right| D_{m_4,e_i} \left| \Psi_0 \right\rangle \times \left[\frac{2\pi i}{E_{N_1}^{(0)} - E_{N_2}^{(0)} + 2\Gamma i} - \frac{4\pi i E_{N_2}^{(1)} E_{N_2}^{(1)}}{\left(E_{N_1}^{(0)} - E_{N_2}^{(0)} + 2\Gamma i \right)^3} \right] \\
\simeq&\frac{1}{N^2} \sum_{m_1,m_2,m_3,m_4} e^{ik_s\cdot(r_{m_2}-r_{m_3})-ik_{\text{in}}\cdot(r_{m_1}-r_{m_4})} \left[\frac{\pi}{\Gamma} \delta_{m_1,m_2}\delta_{m_3,m_4} \left\langle \Psi_0 \right| D^\dagger_{m_1,e_i} D_{m_2,e_f} D^\dagger_{m_3,e_f} D_{m_4,e_i} \left| \Psi_0 \right\rangle \right. \\
&\left. + \sum_{N_1,N_2} \frac{\pi E_{N_1}^{(1)} E_{N_2}^{(1)}}{2\Gamma^3} \left\langle \Psi_0 \right| D^\dagger_{m_1,e_i} \left| N_1 \right\rangle \left\langle N_1 \right| D_{m_2,e_f} D^\dagger_{m_3,e_f} \left| N_2 \right\rangle \left\langle N_2 \right| D_{m_4,e_i} \left| \Psi_0 \right\rangle \right] \\
\simeq&\frac{1}{N^2} \sum_{m_1,m_2,m_3,m_4} e^{ik_s\cdot(r_{m_2}-r_{m_3})-ik_{\text{in}}\cdot(r_{m_1}-r_{m_4})} \left[\frac{\pi}{\Gamma} \left\langle \Psi_0 \right| D^\dagger_{m_1,e_i} D_{m_2,e_f} D^\dagger_{m_3,e_f} D_{m_4,e_i} \left| \Psi_0 \right\rangle \right. \\
&\left. + \sum_{k_1,k_2} \frac{\pi t^2 \cos(k_1 a)\cos(k_2 a)}{2\Gamma^3} \left\langle \Psi_0 \right| D^\dagger_{m_1,e_i} \sum_{\sigma_1} \left| k_1,\sigma_1 \right\rangle \left\langle k_1,\sigma_1 \right| D_{m_2,e_f} D^\dagger_{m_3,e_f} \sum_{\sigma_2} \left| k_2,\sigma_2 \right\rangle \left\langle k_2,\sigma_2 \right| D_{m_4,e_i} \left| \Psi_0 \right\rangle \right.
\end{aligned}
\tag{A.2}
$$

The δ function in the 0^{th} order expansion comes from the fact that without the effect of $\mathcal{H}_c$, the core-hole is immobile. In the last step, we use $\sum_N \left| N \right\rangle E_N^{(1)} \left\langle N \right| = \sum_{k,\sigma} \left| k,\sigma \right\rangle E_k \left\langle k,\sigma \right|$, because the first-order perturbation $E_N^{(1)} = \left\langle n \right| \mathcal{H}_c \left| n \right\rangle$, where $\{\left| n \right\rangle\}$ are the eigenstates of $\mathcal{H}_0$ before the perturbation. We can replace the basis by the eigenstates of $\mathcal{H}_c$, which is $\{\left| k,\sigma \right\rangle\}$, and the eigenenergies $E_k = t\cos(ka)$ following Eq. 3.4.

To derive the correlation function that only contain operators in the valence band, we need to substitute the dipole operator $\mathcal{D}_{m,e}$ with the corresponding valence band and core level operators, and use $\left| \Psi^0 \right\rangle = \left| \Psi_0^v \right\rangle \otimes \left| \Psi_0^c \right\rangle, \left| k,\sigma \right\rangle = \frac{1}{\sqrt{N}} \sum_i e^{ikr_i} p_{i,\sigma} \left| \Psi_0^c \right\rangle$. In

the SC channel, $M_{e_i} = M_{e_f} = \begin{pmatrix} 1 & 0 \\ 0 & 1 \end{pmatrix}$, $\mathcal{D}_{m,e_i} = \mathcal{D}_{m,e_f} = \sum_\sigma d^\dagger_{m,\sigma} p_{m,\sigma}$,

$$I(k_{\rm in}, k_s) \simeq \frac{1}{N^2} \sum_{m_1,m_2,m_3,m_4} e^{ik_s\cdot(r_{m_2}-r_{m_3})-ik_{\rm in}\cdot(r_{m_1}-r_{m_4})} \langle\Psi_0^v| \sum_{\sigma_1} d_{m_1,\sigma_1} d^\dagger_{m_2,\sigma_1} \sum_{\sigma_2} d_{m_3\sigma_2} d^\dagger_{m_4\sigma_2} |\Psi_0^v\rangle \times \left[\delta_{m_1,m_2}\delta_{m_3,m_4}\frac{\pi}{\Gamma} + (\delta_{m_1,m_2+1}+\delta_{m_1,m_2-1})(\delta_{m_3,m_4+1}+\delta_{m_3,m_4-1})\frac{\pi t^2}{8\Gamma^3}\right]. \tag{A.3}$$

Similarly, we can derive in the three NSC channels, they correspond to $M_{e_i} = \sigma^0$, $M_{e_f} = \sigma^x, \sigma^y, \sigma^z$, $\mathcal{D}_{m,e_i} = \sum_\sigma d^\dagger_{m,\sigma} p_{m,\sigma}$, $\mathcal{D}_{m,e_f} = \sum_{\sigma,\overline{\sigma}} d^\dagger_{m,\overline{\sigma}} \sigma^\alpha p_{m,\sigma}$, $\alpha = 0,1,2,3$, substitute it back and the results replace the correlation part in Eq. A.3 with $\langle\Psi_0^v| \sum_{\sigma_1,\overline{\sigma_1}} \sigma^\alpha_{\sigma_1,\overline{\sigma_1}} d_{m_1,\sigma_1} d^\dagger_{m_2,\overline{\sigma_1}} \sum_{\sigma_2,\overline{\sigma_2}} d_{m_3\sigma_2} \sigma^\alpha_{\sigma_2,\overline{\sigma_2}} d^\dagger_{m_4\overline{\sigma_2}} |\Psi_0^v\rangle$. Combining SC and NSC channels, we obtained Eq. 3.5.

The integration over $\omega_{\rm in}$ requires measuring RIXS spectra at different $\omega_{\rm in}$, instead, we can take the resonance peak position of X-ray absorption where $\omega_{\rm in}^{\rm peak} = E_0$ (or $\omega_{\rm in}^{\rm peak} = E_0 - U_c$ if considering core-hole potential), so that $\Delta = i\Gamma$ in Eq. A.1. In the numerical test, the resonance peak is set at the maximal intensity of XAS spectra. Under the ultrashort core-hole lifetime condition,

$$\begin{aligned}
&\int d\Delta\omega\ I\left(k_{\rm in}, k_s, \omega_{\rm in}^{\rm peak}, \Delta\omega\right) \\
&\simeq \frac{1}{N^2} \sum_{m_1,m_2,m_3,m_4} e^{ik_s\cdot(r_{m_2}-r_{m_3})-ik_{\rm in}\cdot(r_{m_1}-r_{m_4})} \langle\Psi_0^v| \sum_{\sigma_1} d_{m_1,\sigma_1} d^\dagger_{m_2,\sigma_1} \sum_{\sigma_2} d_{m_3\sigma_2} d^\dagger_{m_4\sigma_2} |\Psi_0^v\rangle \\
&\times \left[\delta_{m_1,m_2}\delta_{m_3,m_4}\frac{1}{\Gamma^2} + (\delta_{m_1,m_2+1}+\delta_{m_1,m_2-1})(\delta_{m_3,m_4+1}+\delta_{m_3,m_4-1})\frac{t^2}{4\Gamma^4}\right] \\
\simeq &\frac{1}{N^2} \sum_{m_1,m_3} e^{iq(r_{m_1}-r_{m_3})} \left[\frac{1}{\Gamma^2} I_{\{0,0\}} + \frac{t^2}{4\Gamma^4}(e^{i(2k_{\rm in}+q)\cdot a} I_{\{1,1\}} + e^{iqa} I_{\{1,-1\}}\right. \\
&\left. + e^{-iqa} I_{\{-1,1\}} + e^{-i(q+2k_{\rm in})a} I_{\{-1,-1\}})\right],
\end{aligned} \tag{A.4}$$

$$I_{\{x,y\}} = \langle \Psi_0^v | \sum_{\sigma_1} d_{m_1,\sigma_1} d^\dagger_{m_1+x,\sigma_1'} \sum_{\sigma_2} d_{m_3\sigma_2} d^\dagger_{m_3+y,\sigma_2'} | \Psi_0^v \rangle .$$

The spatial correlation can be obtained by integrating over both k_{in} and q

$$I(k_{\text{in}},k_s) = \int d\omega_{\text{in}} \int d\Delta\omega \; I\left(k_{\text{in}}, k_s, \omega_{\text{in}}, \Delta\omega\right) \simeq \frac{1}{N^2} \sum_{m_1,m_3} e^{iq(r_{m_1}-r_{m_3})}$$
$$\left[\frac{\pi}{\Gamma} I_{\{0,0\}} + \frac{\pi t^2}{8\Gamma^3} (e^{i(2k_{\text{in}}+q)\cdot a} I_{\{1,1\}} + e^{iqa} I_{\{1,-1\}} + e^{-iqa} I_{\{-1,1\}} + e^{-i(q+2k_{\text{in}})a} I_{\{-1,-1\}}) \right], \tag{A.5}$$

$$I_{\{x,y\}} = \langle \Psi_0^v | \sum_{\sigma_1} d_{m_1,\sigma_1} d^\dagger_{m_1+x,\sigma_1'} \sum_{\sigma_2} d_{m_3\sigma_2} d^\dagger_{m_3+y,\sigma_2'} | \Psi_0^v \rangle ,$$

$$\begin{aligned} \sum_q e^{iq(r_c-a)} \sum_{k_{\text{in}}} e^{-i2k_{\text{in}}a} I\left(k_{\text{in}}, k_s\right) =& \frac{1}{N} \sum_{m_1} \frac{\pi t^2}{8\Gamma^3} \langle \Psi_0^v | \sum_{\sigma_1} d_{m_1,\sigma_1} d^\dagger_{m_1+1,\sigma_1'} \sum_{\sigma_2} d_{m_1+c,\sigma_2} d^\dagger_{m_1+c+1,\sigma_2'} | \Psi_0^v \rangle \\ =& \frac{\pi t^2}{8\Gamma^3} \langle \Psi_0^v | \sum_{\sigma_1} d_{m_1,\sigma_1} d^\dagger_{m_1+1,\sigma_1'} \sum_{\sigma_2} d_{m_1+c,\sigma_2} d^\dagger_{m_1+c+1,\sigma_2'} | \Psi_0^v \rangle . \end{aligned} \tag{A.6}$$

Although the RIXS spectra at the resonance peak can provide an approximation of the correlations using a different normalization factor, our numerical test indicates that such an approach leads to significant errors. This is primarily due to the wide range of incoming photon frequencies in which the RIXS intensities are non-zero.

A.2 Upper trace boundary of RDM

We can prove that for any state with n particles and $M = mn$ modes, there is an upper boundary for $\text{Tr}\left(O^{\text{con}}\right)$, because the electron or hole representations are equivalent

for $\mathrm{Tr}\,(O^{\mathrm{con}})$. Here we assume the n particles are holes, and $\langle n_i\rangle = \langle c_i c_i^\dagger\rangle$ as

$$\begin{aligned}
\mathrm{Tr}\,(O^{\mathrm{con}}) &= \sum_{i,j,i\neq j}\Big(\langle c_i c_j c_j^\dagger c_i^\dagger\rangle - \langle c_i c_i^\dagger\rangle\langle c_j c_j^\dagger\rangle + \langle c_i c_j^\dagger\rangle\langle c_j c_i^\dagger\rangle\Big) \\
&= n(n-1) - \sum_{i\neq j}\Big(\langle c_i c_i^\dagger\rangle\langle c_j c_j^\dagger\rangle + |\langle c_i c_j^\dagger\rangle|^2\Big) \\
&\geq n(n-1) - \sum_i \langle c_i c_i^\dagger\rangle \sum_j \langle c_j c_j^\dagger\rangle + \sum_i \Big|\langle c_i c_i^\dagger\rangle\Big|^2 \qquad \text{(A.7)} \\
&\geq -n + \sum_i n_i^2 \\
&\geq -n\left(1-\frac{1}{m}\right).
\end{aligned}$$

The last inequality is obtained from minimizing $\sum_i^{mn} n_i^2$ when given $\sum_i^{mn} n_i = n$. The state reaches this upper bound is the GHZ state as defined in Eq. 3.22.

In the natural spin oribitals (NSO), the basis is the eigenvector of single-particle reduced density matrix, so $\langle c_i c_j^\dagger\rangle = n_i\delta_{i,j}$. We can also prove the following inequality

$$\mathrm{Tr}\,(O^{\mathrm{con}}) = \sum_{i,j,i\neq j}\Big(\langle c_i c_j c_j^\dagger c_i^\dagger\rangle - \langle c_i c_i^\dagger\rangle\langle c_j c_j^\dagger\rangle\Big) = n(n-1) - \sum_i \langle c_i c_i^\dagger\rangle)^2 + \sum_i \langle c_i c_i^\dagger\rangle^2 \leq n(n-1) - n^2 + n = 0. \qquad \text{(A.8)}$$

The last inequality is because $\langle c_i c_i^\dagger\rangle \leq 1$ and $\sum_i \langle c_i c_i^\dagger\rangle = n$, the largest $\sum_i \langle c_i c_i^\dagger\rangle^2$ appears when $\langle c_i c_i^\dagger\rangle = 1, i = 1, 2, \cdots, n$ and the others are zero. In summary, we have

$$-n\left(1-\frac{1}{m}\right) \leq \mathrm{Tr}\,(O^{\mathrm{con}}) \leq 0. \qquad \text{(A.9)}$$

To prove the inequality for $\mathrm{Tr}\,[(O^{\mathrm{con}})^2]$, we need to show that the generalized GHZ states take the upper boundary of $\mathrm{Tr}\,[(O^{\mathrm{con}})^2]$. Because it is invariant in different basis, we choose an NSO basis, where the off-diagonal elements of the one-particle reduced density matrix are always zero, i.e. $\langle c_i c_j^\dagger\rangle = \delta_{i,j} n_i$. We prove the upper boundary for n-particle state in $n = 2, 3, 4$.

A.2.1 n=2

When there are two particles in the system, we can always write the state as a sum of elementary Slater determinants where each single-particle basis state occurs at most in one term. The general state vector is

$$|\omega\rangle = \sum_{i,j=1}^{N} \omega_{ij} c_i^\dagger c_j^\dagger |0\rangle\,,\ \omega \mapsto U\omega U^T = \mathrm{diag}\left[Z_1, \cdots, Z_r, Z_0\right] \tag{A.10}$$

where $Z_i = \begin{bmatrix} 0 & z_i/2 \\ -z_i/2 & 0 \end{bmatrix}$, $z_i > 0$, $\sum_i z_i^2 = 1$, and Z_0 is the $(N-2r)\times(N-2r)$ null matrix. In this representation, we can derive that

$$\begin{aligned} \mathrm{Tr}\left[(O^{\mathrm{con}})^2\right] &= 4\sum_{i=1}^{r}\left(z_i^2 - z_i^4\right)^2 + 8\sum_{\langle i,j\rangle} z_i^2 z_j^2 + 16\sum_{\langle i,j\rangle} z_i^4 z_j^4 \\ &= 4\left(\left(\sum_i z_i^2\right)^2 + \sum_i z_i^8 - 2\sum_i z_i^6 + 4\sum_{\langle i,j\rangle} z_i^4 z_j^4\right) \\ &= 4\left(1 + \sum_i z_i^8 - 2\sum_i z_i^6 + 4\sum_{\langle i,j\rangle} z_i^4 z_j^4\right) \end{aligned} \tag{A.11}$$

where $\langle i,j\rangle$ indicates all pairs of i,j indices with $i \neq j$, all z_i are totally symmetric in the function, i.e. exchanging them in any order does not affect the function. Now to find the upper bound of $\mathrm{Tr}\left[(O^{\mathrm{con}})^2\right]$, this is an optimization subject to an equality constraint, we use the Lagrange multiplier method to solve the equivalent problem where $x_i = z_i^2$, $f(\{x_i\}) = \mathrm{Tr}\left[(O^{\mathrm{con}})^2\right]/4$

$$\begin{aligned} f\left(\{x_i\}\right) &= \sum_i x_i^4 - 2\sum_i x_i^3 + 4\sum_{\langle i,j\rangle} x_i^2 x_j^2 \\ g(\{x_i\}) &= \sum_i x_i - 1 = 0 \\ \frac{\partial f}{\partial x_j} + \lambda\frac{\partial g}{\partial x_j} &= -4x_j^3 - 6x_j^2 + 8x_j\left(\sum_i x_i^2\right) + \lambda = 0 \end{aligned} \tag{A.12}$$

so all $\{x_i\}$ at the saddle point fulfills the same equation of x_j, the equation has at most two solutions in the range of $0 \leq x_j \leq 1$, therefore, there is at most one solution refers to the local maximum because we can not have two local maxima without a local minimum. Finally, the only possible solution refers to a local maximum is when all x_i are equal, substitute this condition back to the equation, we derive the maximal value of $\mathrm{Tr}\left[(O^{\mathrm{con}})^2\right]$ for a general fermion state with two particles and Slater rank r

$$\mathrm{Tr}\left[(O^{\mathrm{con}})^2\right] \leq 4\left(1 - \frac{1}{r^3}\right). \tag{A.13}$$

The equality is satisfied when the state fulfills $z_1 = z_2 = \cdots = z_r = \frac{1}{\sqrt{r}}$, we call these kind of states, general GHZ state, and $\mathrm{Tr}\left[(O^{\mathrm{con}})^2\right]$ increases as the Slater rank r increases, when $r \to \infty$, $\mathrm{Tr}\left[(O^{\mathrm{con}})^2\right] = 4$.

A.2.2 n=3

The general form of a three-fermion state is

$$|\omega\rangle = \sum_{i,j,k=1}^{N} \omega_{ijk} c_i^\dagger c_j^\dagger c_k^\dagger |0\rangle\,, \ \sum_{ijk} \omega_{ijk}^* \omega_{ijk} = \frac{1}{6} \tag{A.14}$$

where ω is completely antisymmetric. While it can not be transformed into a sum of Slater determinants [22], we can still simplify it in the natural spin orbital (NSO) basis. To start with, let us consider a special case when the total mode number $N = 2n = 6$, there are $\binom{6}{3} = 20$ parameters in the antisymmetric tensor ω_{ijk}.

a general state in NSO basis can be written as

$$|\omega\rangle = \left(\omega_{123} c_1^\dagger c_2^\dagger c_3^\dagger + \omega_{156} c_1^\dagger c_5^\dagger c_6^\dagger + \omega_{264} c_2^\dagger c_6^\dagger c_4^\dagger + \omega_{345} c_3^\dagger c_4^\dagger c_5^\dagger\right) |0\rangle \tag{A.15}$$

where now we only have 4 parameters. This is because in the NSO basis, each index can only appear twice, for example, index 1 only appears in ω_{123}, ω_{156}, adding any other term containing 1 will cause off-diagonal term in the one-particle reduced den-

sity matrix. Therefore, only $N \times 2/n = 4$ terms are allowed. Eq. A.15 is not the only possible NSO basis representation, however, other representation is equivalent under a fermion basis transformation, for example, $|\omega\rangle = \left(\omega_{123}c_1^\dagger c_2^\dagger c_3^\dagger + \omega_{145}c_1^\dagger c_4^\dagger c_5^\dagger + \omega_{246}c_2^\dagger c_4^\dagger c_6^\dagger + \omega_{356}c_3^\dagger c_5^\dagger c_6^\dagger\right)|0\rangle$ is another NSO basis representation and by exchanging indices 4 and 6, we recover Eq. A.15.

Assuming $\{\omega_{123}, \omega_{156}, \omega_{264}, \omega_{345}\} = \{z_1, z_2, z_3, z_4\}$, we derive

$$\begin{aligned}\mathrm{Tr}\left[(O^{\mathrm{con}})^2\right] = {} & h(z_1, \{z_2, z_3, z_4\}) + h(z_2, \{z_1, z_3, z_4\}) + h(z_3, \{z_1, z_2, z_4\}) + h(z_4, \{z_1, z_2, z_3\}) \\ & + \sum_{\langle z_i, z_j\rangle} h(z_i, z_j) + h(z_1, z_2, z_3, z_4)\end{aligned} \tag{A.16}$$

where

$$\begin{aligned}h(a, \{b, c, d\}) = {} & 4\left(a^2 - \left(a^2 + b^2\right)\left(a^2 + c^2\right)\right)^2 + 4\left(a^2 - (a^2 + b^2)(a^2 + d^2)\right)^2 \\ & + 4\left(a^2 - (a^2 + c^2)(a^2 + d^2)\right)^2 \\ h(a, b) = {} & 8a^2b^2 \\ h(z_1, z_2, z_3, z_4) = {} & 4\left(-(z_1^2 + z_2^2)(z_3^2 + z_4^2)\right)^2 + 4\left(-(z_1^2 + z_3^2)(z_2^2 + z_4^2)\right)^2 + 4\left(-(z_1^2 + z_4^2)(z_2^2 + z_3^2)\right)^2.\end{aligned}$$

z_1, z_2, z_3, z_4 are totally symmetric in $\mathrm{Tr}\left[(O^{\mathrm{con}})^2\right]$. Again, we can substitute $x_i = z_i^2$ and use the Lagrange multiplier method, $f\left(\{x_i\}\right) = \mathrm{Tr}\left[(O^{\mathrm{con}})^2\right]/4$, $g(\{x_i\}) = \sum_i x_i - 1 = 0$,

$$\frac{\partial f}{\partial x_j} + \lambda\frac{\partial g}{\partial x_j} = 8 + \lambda - 16s_2 + 16s_3 + 16s_2' + (4 + 24s_2)\, x_j - 32x_j^2 = 0 \tag{A.17}$$

where $s_2 = \sum_i x_i^2$, $s_3 = \sum_i x_i^3$, $s_2' = \sum_{\langle i,i'\rangle} x_i x_{i'}$, if we treat them as constants, then at the saddle point, every x_j is the solution of the same equation. The equation has at most two solutions because it is quadratic to x_j, thus similarly to the previous case, there is only one solution that refers to the local maximum. We derive again that the local maximum solution only appears when some of x_i can be zero, and all the rest are equal. It turns out that, when $z_1 = z_2 = z_3 = z_4 = \pm\frac{1}{2}$, $\mathrm{Tr}\left[(O^{\mathrm{con}})^2\right] = \frac{15}{4}$. And when $z_1 = z_2 = z_3 = \pm\frac{1}{\sqrt{3}}, z_4 = z_0$, $\mathrm{Tr}\left[(O^{\mathrm{con}})^2\right] = \frac{104}{27} > \frac{15}{4}$. Thus especially at

$n = 3$, the upper bound does not appear at a GHZ-type state, as we will discuss in more detail in the next paragraph.

The state with $z_1 = z_2 = z_3 = \pm\frac{1}{\sqrt{3}}, z_4 = z_0$ that reaches this upper boundary can be transformed into a W-type state by performing a basis transformation. And the state with $z_1 = z_2 = z_3 = z_4 = \pm\frac{1}{2}$ can be transformed into a GHZ-type state. The W and GHZ states are two inequivalent maximally entangled states, here the W state reaches the upper bound. To show the transformation, we relabel $\{1, 2, 3, 4, 5, 6\}$ as $\{1, 2, 3, \dot{1}, \dot{2}, \dot{3}\}$, and relabel some of the fermion states into equivalent spin states, as

$$\begin{aligned}&\left(|123\rangle, |12\dot{3}\rangle, |1\dot{2}3\rangle, |\dot{1}23\rangle, |1\dot{2}\dot{3}\rangle, |\dot{1}2\dot{3}\rangle, |\dot{1}\dot{2}3\rangle, |\dot{1}\dot{2}\dot{3}\rangle\right)\\ &= \left(|000\rangle, |001\rangle, |010\rangle, |100\rangle, |011\rangle, |101\rangle, |110\rangle, |111\rangle\right)\end{aligned} \tag{A.18}$$

With this relabeling, we perform a basis transformation on both cases to show how they are actually W and GHZ types of states,

$$\begin{aligned}|\omega_1\rangle =& \left(\frac{1}{\sqrt{3}}c_1^\dagger c_2^\dagger c_3^\dagger + \frac{1}{\sqrt{3}}c_1^\dagger c_5^\dagger c_6^\dagger + \frac{1}{\sqrt{3}}c_2^\dagger c_6^\dagger c_4^\dagger\right)|0\rangle\\ =& \left(\frac{1}{\sqrt{3}}|000\rangle + \frac{1}{\sqrt{3}}|011\rangle + \frac{1}{\sqrt{3}}|101\rangle\right)\\ =& (I\otimes I\otimes X)\frac{1}{\sqrt{3}}\left(|001\rangle + |010\rangle + |100\rangle\right)\\ =& (I\otimes I\otimes X)|\mathrm{W}\rangle\end{aligned} \tag{A.19}$$

$$\begin{aligned}|\omega_2\rangle =& \left(\frac{1}{2}c_1^\dagger c_2^\dagger c_3^\dagger + \frac{1}{2}c_1^\dagger c_5^\dagger c_6^\dagger + \frac{1}{2}c_2^\dagger c_6^\dagger c_4^\dagger + \frac{1}{2}c_3^\dagger c_4^\dagger c_5^\dagger\right)|0\rangle\\ =& \frac{1}{2}\left(|000\rangle + |011\rangle + |101\rangle + |110\rangle\right)\\ =& (H\otimes H\otimes H)\left(\frac{1}{\sqrt{2}}|000\rangle + \frac{1}{\sqrt{2}}|111\rangle\right)\\ =& (H\otimes H\otimes H)|\mathrm{GHZ}\rangle\end{aligned} \tag{A.20}$$

Now we move forward to consider a more general case when the total mode number $N = 3m$ and m is an integer value. The key idea is that we want to show any general

state can be represented in a symmetric form such that every nonzero coefficient ω_{ijk} is a symmetric variable in the function $\mathrm{Tr}\left[(O^{\mathrm{con}})^2\right]$. If we perform the Lagrange multiplier method to find the saddle point, then the differential equation for each ω_{ijk} is exactly the same. By estimating the number of solution for the Lagrange multiplier equation, we want to show that the maximal solution only appears at the boundary or when all nonzero ω_{ijk} are the same in our symmetric state representation, and that state refers to the generalized GHZ state in a different basis. It turns out we can find such a symmetric representation in the NSO basis, the rules are:

- (NSO) between any two nonzero $\omega_{ijk}, \omega_{i'j'k'}$, they share at most one common index.

- (complete) the basis should include as many as nonzero coefficients as possible, adding any extra coefficient will violate the NSO condition.

- (symmetric) each mode index i appears the same number of times in all nonzero coefficients $\{\omega_{ijk}\}$.

Combining the three conditions together, we can calculate the largest number of nonzero coefficients. From the NSO condition we learn that any pair of indices only appears once in all nonzero coefficients, there are in total $\frac{3m(3m-1)}{2}$ pairs, so we have at most $\frac{3m(3m-1)}{6}$ nonzero coefficients. For example, when $m = 3$, we have $\{123, 145, 167, 189, 256, 278, 249, 347, 358, 369, 468, 579\}$. For $m = 2$, we only have 4 nonzero coefficients, the reason is that there are in total $3m = 6$ indices, so each index can only appear twice by combing with the rest 5 indices, which is an odd number, so each index can only appears $\left[\frac{3m-1}{2}\right]$ times, formally we have at most $m\left[\frac{3m-1}{2}\right]$ nonzero coefficients.

A.3 Model Hamiltonian and numerical methods

To demonstrate this protocol of witnessing entanglement by RIXS, we exploit a 1D extended Hubbard model (EHM) with attractive interaction, whose phase diagram is

explicitly obtained in Ref. [187]. The Hamiltonian of the EHM reads as

$$\begin{aligned}\mathcal{H} =& -t\sum_{i\sigma}\left[c^{\dagger}_{i\sigma}c_{i+1,\sigma}+\text{h.c.}\right]+U\sum_{i}n_{i\uparrow}n_{i\downarrow}\\ &+V\sum_{i,\sigma,\sigma'}n_{i\sigma}n_{i+1,\sigma'}+\mathcal{H}_{c}.\end{aligned} \tag{A.21}$$

We fix $t = 1$ as a reference value for other parameters. In the spectra simulation and the comparison with the exact correlations, We conduct exact diagonalization (ED) in a finite system size of $N = 12$ respectively, where N is the number of sites in the 1D chain, and calculate the RIXS spectra with core Hamiltonian defined in Eq. 3.4 to compare the RIXS derived correlations with the exact ones. The corresponding spectra depend on both k_{in} and q as we discussed. In the RIXS spectra calculation, we set the core-hole lifetime $\Gamma = 10$, the range of ω_{in} is $[-50, 50]$ with the spacing 0.5, and $\Delta\omega \in [-6, 15]$ with the spacing being 0.05. As discussed in the second subsection of Sec. 3.2, experimentally, we can derive four-point correlations with all possible combinations of spin indices from one SC channels and three NSC channels corresponding to the polarization of photons. While numerically, we directly calculate the four-point correlations with different spin indices. In Fig. 3-3, the true values are obtained from directly calculating the correlations using ED, and the $\Gamma = 10$ values are obtained from first numerically calculate the RIXS intensities over ω_{in}, $\Delta\omega$, q, k_{in}, and do the summation with phase factor as described in Sec. 3.2.

Before the DMRG calculations, we first conduct exact diagonalization in small system sizes with a periodic boundary condition where $N = 12, 14, 16$; N is the number of sites in the 1D chain. At half filling, as shown in Fig. A-1, we detect at most 4-particle entanglement at $N = 16$, however, the finite system size is not excluded so larger system size can lead to different results, and the largest entanglement appears at the PS2(phase separation) region, while the TS(spin-triplet) phase is expected to be more entangled. As mentioned in Sec. 3.2, our proposed RIXS techniques can only measure the connected four-point correlations with a nearest neighbor constrain, the measurable results in Fig. A-1 correspond to the approximated $\text{Tr}\left[(O^{\text{con}})^2\right]$ by setting all connected correlation inaccessible to RIXS as zeros, and the approximated value

is always smaller than the accurate values because $\mathrm{Tr}\left[(O^{\mathrm{con}})^2\right]$ is equivalent to the Frobenius norm of O^{con} which always increases with absolute value of each element. We show that, even though the measurable $\mathrm{Tr}\left[(O^{\mathrm{con}})^2\right]$ is much smaller than the exact one for states with small multiparticle entanglement, they are closer for large multipartite entangled states and the measurable one also reaches the upper bound for $n = 4$ thus detects the $n = 4$ multipartite entanglement.

In Sec. 3.4 A, we conduct DMRG on the same model with a larger system size, and measure the correlations directly. While in the main text we focus on the results at half filling, here we attach the results at quarter filling, as shown in Fig. A-3.

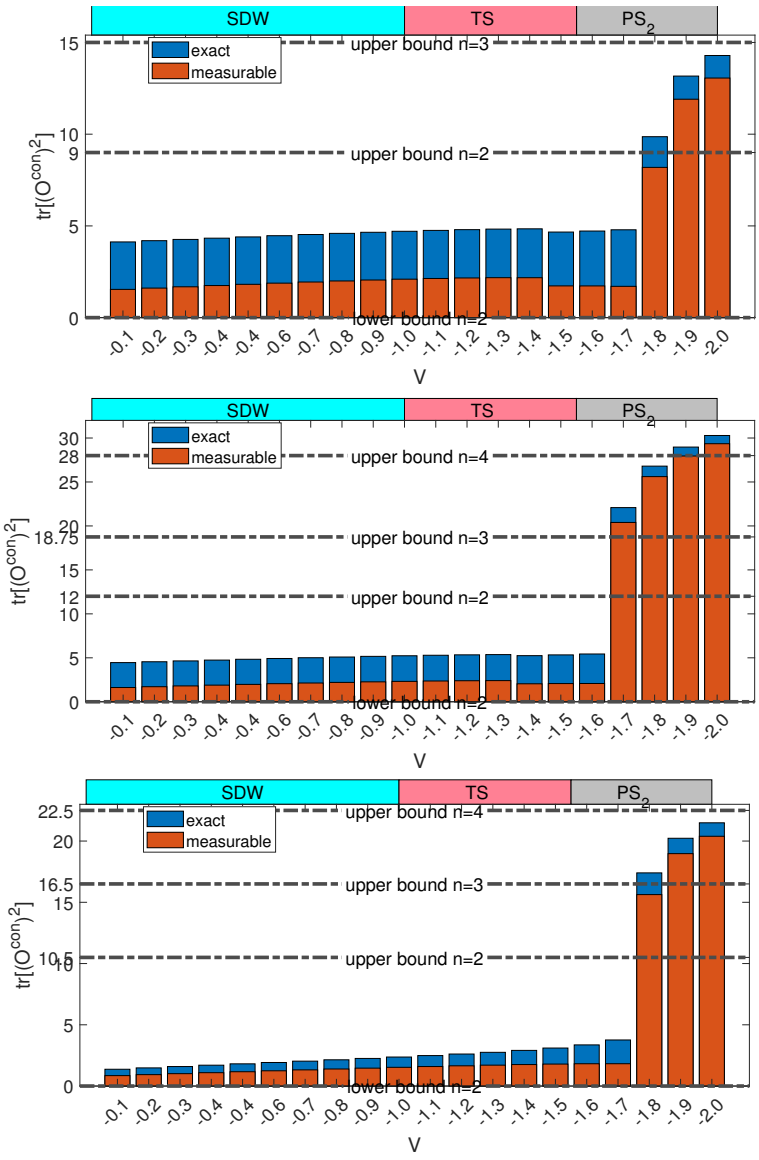

Figure A-1: (top) N=12, M=24; (middle) N=14, M=28; (bottom) N=16, M=32. $\mathrm{Tr}\left[(O^{\mathrm{con}})^2\right]$ results in EHM at half filling, with $U = 1.6$, $t = 1$ and nearest neighbor interaction V shows in the x-axis. Both exact values and measurable ones that are achievable by our proposed RIXS method are shown. The upper boundaries are derived from Eq. 3.20 for different system size N. The lower boundary of $n = 2$ is always zero based on our definition.

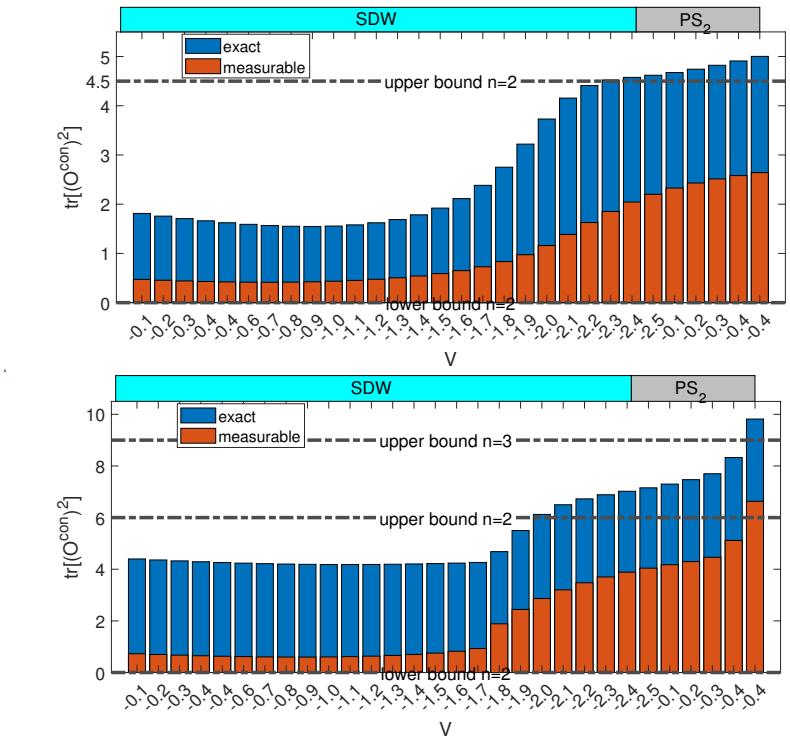

Figure A-2: (top) N=6, M=24; (bottom) N=8, M=32. Tr $[(O^{\text{con}})^2]$ results in EHM at quarter filling, with $U = 4$, $t = 1$ and nearest neighbor interaction V shows in the x-axis.

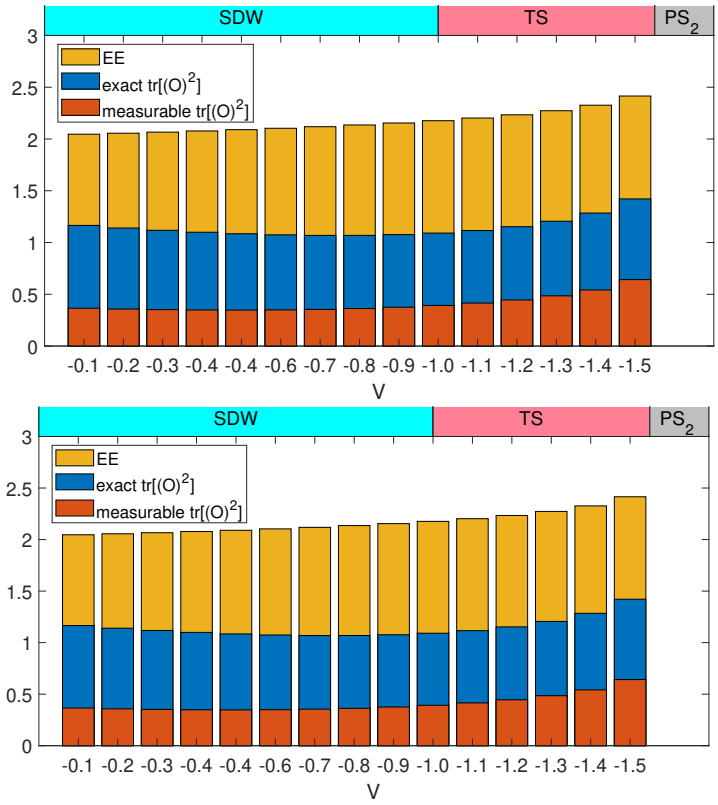

Figure A-3: DMRG results of EHM at quarter filling with open boundary condition. Only the central 12 orbitals are counted for $\mathrm{Tr}\left[(O^{\mathrm{con}})^2\right]$. $U = 4$, $t = 1$ and nearest neighbor interaction V shows in the x-axis. The exact and measurable values of $\mathrm{Tr}\left[(O^{\mathrm{con}})^2\right]$ and the entanglement entropy are shown.

Appendix B

Appendices of Chapter 4

In this Appendix, we provide more details about the setup of our theoretical and numerical studies. In Sec. B.1-B.1.5, we explain how we study integer quantum Hall states on the surface of topological crystalline insulator (TCI), which has Dirac dispersion that is both tilted and massive. In Sec. B.1 we discuss the symmetry on the (001) surface of TCI $Sn_{1-x}Pb_x$(Te,Se), and introduce the low-energy $k \cdot p$ model for our subsequent study. The Dirac Landau levels in this system are solved in Sec. B.1.1, and it is argued in Sec. B.1.2 that in the presence of delta-potential impurity, there are exactly two states per Landau level that are perturbed away in energy. In Sec. B.1.3 we explain the values of parameters adopted in our model. In Sec. B.1.4 we derive the relation between the local impurity dipole moment and the bulk adiabatic dipole moment, which is quoted in the main text, while in Sec. B.1.5 we distinguish these two notions of dipole and identify the one that can reveal ferroelectricity in our system. In Sec. B.1.6, we present the setup for carrying out exact diagonalization which leads to the prediction of non-trivial excitonic states near strong impurities. While the experimental signatures of these many-body states in systems with Dirac dispersion have been discussed in the main text, a simpler situation with anisotropic parabolic dispersion (such as in AlAs quantum well) is analyzed in Sec. B.1.7.

B.1 $M\mathcal{T}$ symmetry and its spontaneous breaking

The low-energy effective Hamiltonian is introduced in Eq. (1) of the main text. Here we describe a symmetry that relates the two valleys under consideration.

We are interested in the (001) surface of TCI. It is known from earlier studies that there is a structural distortion occurring spontaneously at low temperature and breaks all rotation symmetry [188]. This distortion can happen along either [110] or [1$\bar{1}$0] direction, and leads to a ferroelectric polarization. Note that this is *not* the quantum Hall ferroelectricity that we study in this paper. Without loss of generality, let us assume the distortion is along [110] and set up the coordinates such that it is the x-direction. Because of the ferroelectric distortion, the (001) surface has only the mirror symmetry M_y, which reverses the y-direction, and time-reversal $\mathcal{T}$. An illustration of the surface Brillouin zone is shown in Fig. B-1. The low-energy effective model consists of four Dirac cones, with a massive degenerate pair near $\bar{X}_1$ and a massless degenerate pair near $\bar{X}_2$ [189]. The $2+2$-fold degeneracy is protected by $\mathcal{T}$.

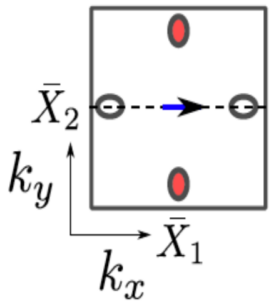

Figure B-1: Surface Brillouin zone of the (001) surface of TCI. There is a pair of Dirac cones near $\bar{X}_1$ and a pair near $\bar{X}_2$. The blue arrow indicates the ferroelectric distortion.

In the presence of magnetic field, the mirror symmetry M_y and the time-reversal $\mathcal{T}$ are *individually* broken. Still, the product $M_y\mathcal{T}$ remains a symmetry. Notice that $M_y\mathcal{T}$ relates the individual valleys near $\bar{X}_1$ to themselves, while it exchanges opposite valleys near $\bar{X}_2$. Hence, under a magnetic field, such $2+2$-fold degeneracy of Landau levels is explicitly broken down to just the 2-fold degeneracy for the massless Dirac

cones near $\bar{X}_2$. Moreover, such originally massless Dirac cones can now acquire a Zeeman gap, as we explain below.

Let us label the location of the Dirac cones as $\pm\Lambda$. At $+\Lambda$, a two-band model has been constructed before and admits the following form [189, 190]:

$$H_{+\Lambda} = v_x\sigma_y p_x + v_y\sigma_x p_y + \delta v_x p_x + \Delta\sigma_z, \tag{B.1}$$

Here δv_x characterizes the tilt of Dirac cone, which is symmetry-allowed and has been observed experimentally [191]. The mirror symmetry M_y acts on the pseudo-spin and momentum as follows:

$$M_y : p_x \to p_x,\ p_y \to -p_y,\ \sigma_x \to -\sigma_x,\ \sigma_y \to \sigma_y,\ \sigma_z \to -\sigma_z, \tag{B.2}$$

while time-reversal $\mathcal{T}$ acts as follows:

$$\mathcal{T} : p_x \to -p_x,\ p_y \to -p_y,\ \sigma_x \to -\sigma_x,\ \sigma_y \to -\sigma_y,\ \sigma_z \to -\sigma_z. \tag{B.3}$$

From these we see that the mass term $\Delta = 0$ in the absence of background field, as M_y is a symmetry that relates the cone at $+\Lambda$ to itself but sends $\Delta\sigma_z$ to $-\Delta\sigma_z$. However, in the presence of a magnetic field, M_y is no longer a symmetry, and hence the massless Dirac cone at $+\Lambda$ can acquire mass in general (*i.e.* Zeeman effect). The remaining symmetry is the $M_y\mathcal{T}$ symmetry which relates the cone at $+\Lambda$ to the one at $-\Lambda$:

$$H_{-\Lambda} = (M_y\mathcal{T})H_{+\Lambda}(M_y\mathcal{T})^{-1} = v_x\sigma_y p_x + v_y\sigma_x p_y - \delta v_x p_x + \Delta\sigma_z. \tag{B.4}$$

To simplify notation, we rotate the basis: $\sigma_x \to -\sigma_y,\ \sigma_y \to \sigma_x,\ \sigma_z \to \sigma_z$ and obtain the following unitarily equivalent Hamiltonian:

$$H_{\pm\Lambda} = v_x\sigma_x p_x - v_y\sigma_y p_y \pm \delta v_x p_x + \Delta\sigma_z. \tag{B.5}$$

This is Eq. (1) in the main text, which provides the starting point for our study.

In the main text, we have referred to the symmetry that protects the degeneracy of the two valleys as a “two-fold rotation" or “inversion" symmetry, but when applied specifically to the surface of TCI, it has a precise meaning as the $M\mathcal{T}$ symmetry. This symmetry is spontaneously broken by Coulomb interaction and results in a valley-polarized state.

B.1.1 Massive and tilted Dirac Landau levels

Assuming valley-polarization, we focus on the one at $+\Lambda$. Under an out-of-plane magnetic field $-B\hat{z}$, in the un-tilted limit, the massive Dirac Hamiltonian in Eq. (B.5) can be written as

$$H_0 = \frac{\sqrt{2}\, v}{l_B} \begin{pmatrix} \lambda & a^\dagger \\ a & -\lambda \end{pmatrix} \tag{B.1}$$

where $v = \sqrt{v_x v_y}$, magnetic length $l_B = \sqrt{\hbar c/eB}$ and the mass parameter $\lambda = \Delta l_B/(\sqrt{2}v)$. Here, $a^\dagger, a$ are parabolic Landau level raising and lowering operators respectively, and are related to the momentum operators by:

$$\begin{gathered} p_x = \frac{1}{l_B}\sqrt{\frac{v_y}{2v_x}}(a^\dagger + a)\ , \quad p_y = \frac{i}{l_B}\sqrt{\frac{v_x}{2v_y}}(a - a^\dagger) \\ [a, a^\dagger] = 1 \end{gathered} \tag{B.2}$$

The wavefunctions of the massive Dirac Landau levels and their corresponding energy can then be solved exactly. For the n-th Landau level with $n \neq 0$:

$$\psi_{n,m} = \frac{1}{\sqrt{1+\gamma_n^2}} \begin{pmatrix} \phi_{n,m} \\ \gamma_n \phi_{n-1,m} \end{pmatrix}, \quad E_n = s_n \frac{\sqrt{2}\, v}{l_B}\sqrt{\lambda^2 + n} \tag{B.3}$$

where

$$\gamma_n = \frac{-\lambda + s_n\sqrt{\lambda^2 + n}}{\sqrt{n}} \tag{B.4}$$

Here $s_n = \mathrm{sign}(n)$, and $\phi_{n,m}$ are the wavefunctions for a parabolic Landau level in the symmetric gauge with angular momentum $m - n$. For the 0-th Dirac Landau level,

we have:

$$\psi_{0,m} = \begin{pmatrix} \phi_{0,m} \\ 0 \end{pmatrix}, \quad E_0 = \frac{\sqrt{2}\, v}{l_B}\lambda \tag{B.5}$$

When the tilt of Dirac cone δv_x is turned on, we can do first order perturbation theory to obtain the approximate eigenstates. To leading order in $\tau = \delta v_x/(2v_x)$, for the $n \neq 0$ massive and tilted Dirac LL, we obtain (up to normalization):

$$\psi_{n,m} = \begin{pmatrix} \phi_{n,m} \pm \tau[\alpha_{-1}\phi_{n-1,m} + \alpha_1\phi_{n+1,m}] \\ \gamma_n[\phi_{n-1,m} \mp \tau(\alpha_0\phi_{n,m} + \alpha_{-2}\phi_{n-2,m})] \end{pmatrix} \tag{B.6}$$

where

$$\begin{aligned} \alpha_{-1} &= \frac{(2n-1)\sqrt{\lambda^2+n} \pm \lambda}{\sqrt{n}}\,,\ \alpha_1 = -2\sqrt{n+1}\sqrt{\lambda^2+n} \\ \alpha_0 &= \frac{(2n+1)\sqrt{\lambda^2+n} \pm \lambda}{\sqrt{n}}\,,\ \alpha_{-2} = -2\sqrt{n-1}\sqrt{\lambda^2+n} \end{aligned} \tag{B.7}$$

As for the massive and tilted 0-th Dirac LL:

$$\psi_{0,m} = \begin{pmatrix} \phi_{0,m} - 2\tau\lambda\phi_{1,m} \\ -\tau\phi_{0,m} \end{pmatrix} \tag{B.8}$$

These expressions allow us to calculate dipole moments, and energy shifts under the influence of impurity, straightforwardly.

B.1.2 Number of impurity states for massive and tilted Dirac cones

Here we demonstrate that there are only two states that have probability amplitudes at the impurity site, and which therefore are split from the Landau level, even in the presence of perturbations in mass and tilt of the Dirac cone.

We consider a delta-function impurity $H_{imp} = V_0 l_B^2 \delta(\vec{x})$. Upon projection to a specific Landau level, the impurity Hamiltonian has matrix elements:

$$\langle n, m|\, H_{imp}\, |n, m'\rangle = V_0 l_B^2 \Psi^\dagger_{n,m}\Psi_{n,m'} \tag{B.1}$$

where we have defined $\Psi_{n,m} \equiv \psi_{n,m}(\vec{0})$, *i.e.* the amplitude of the Landau level orbital at the impurity site. To the first order in tilt τ, the Dirac Landau level is found in Eq. (B.6). To prove our claim in full generality, let us assume we have carried out a k-th order perturbation theory in τ, so that the n-th tilted Dirac Landau level $\psi_{n,m}$ is expressed in terms of $\phi_{p,m}$ with $p = n-k-1, ..., n+k$. The only states that are relevant to our impurity problem are those that have non-vanishing probability amplitudes at the impurity site, which correspond to those $\psi_{n,m}$ with $m = n-k-1, ..., n+k$. We thus study the degenerate perturbation theory within this subspace, and consider linear combinations of $\Psi_{n,m}$:

$$\Phi = r_1 \Psi_{n,n-k-1} + r_2 \Psi_{n,n-k} + ... + r_{2k+2} \Psi_{n,n+k} \tag{B.2}$$

If there is a choice of $(r_1, r_2, ..., r_{2k+2})$ such that $\Phi = (0,0)^T$, the corresponding linear combination of intra-Landau level orbitals are guaranteed to diagonalize the impurity Hamiltonian and thus remain at the same energy as the Landau level in the absence of impurity. Below, we argue that there are $2k$ such solutions.

Denote $\Psi_{n,m} = (\psi^{\uparrow}_m,\ \psi^{\downarrow}_m)^T$. Only the intra-Landau level index m is made explicit here. Notice that $\psi^{\uparrow}_m$ and $\psi^{\downarrow}_m$ are both real or both imaginary. This is because each of them is proportional to the wavefunction of parabolic Landau level $\phi_{m,m}$ evaluated at the origin, which is real when m is even and is imaginary when m is odd. Redefining $i\Psi_{n,m} \mapsto \Psi_{n,m}$ for odd m, Eq. (B.2) with $\Phi = (0,0)^T$ becomes a set of simultaneous equations for *real* unknowns r_i. Setting $r_{2k+2} = 1$ without loss of generality, we reach the following set of equations for $r_i \in \mathbb{R}$:

$$\begin{cases} r_1 \psi^{\uparrow}_{n-k-1} + r_2 \psi^{\uparrow}_{n-k} + ... + r_{2k+1} \psi^{\uparrow}_{n+k-1} = -\psi^{\uparrow}_{n+k} \\ r_1 \psi^{\downarrow}_{n-k-1} + r_2 \psi^{\downarrow}_{n-k} + ... + r_{2k+1} \psi^{\downarrow}_{n+k-1} = -\psi^{\downarrow}_{n+k} \end{cases} \tag{B.3}$$

With $2k+1$ unknowns and only two linear equations, there are in general $2k$ linearly independent solutions, leading to $2k$ states that have vanishing amplitudes at the impurity site. Since we start with a $(2k+2)$-dimensional subspace, only $2k+2-2k = 2$ states are allowed to have non-vanishing amplitudes at the origin.

These are the two impurity bound states whose energy are split from the bulk Landau level, and are the ones employed in our construction of impurity dipole moment in the main text.

The above argument also works for the 0-th Landau level. However, only one impurity state is significantly shifted away from the bulk Landau level, while the shift of the second impurity state is minuscule (controlled by the size of the tilt), so practically, in the quantum Hall ferroelectric system that we consider, only one impurity state can be probed in this special case.

B.1.3 Choice of Parameters

In the main text, we use the following parameters to study the quantum Hall ferroelectrics in topological crystalline insulator $Sn_{1-x}Pb_x$(Te,Se):

$$\tau = 0.1, \quad \lambda = 0, \quad v_x/v_y = 1.6 \tag{B.4}$$

Here we explain why these values match with the low-energy physics of the system obtained either from experiments or *ab initio* calculations.

The tilting effect of Dirac cones (at $\bar{\Lambda}$) has been observed in the ARPES measurements by Tanaka *et al.* [191], from which we estimate the tilting parameter to be $\tau = \delta v_x/(2v_x) = 0.1$. The acquisition of mass in topological crystalline insulators was observed by Okada *et al.* [192]. Under a ferroelectric distortion, two of the four surface Dirac cones were measured to obtain mass of about $\Delta = 10$ meV, and this would correspond to $\lambda = \Delta l_B/(\sqrt{2}v) \approx 0.5$. But notice that these two massive cones are located near $\bar{X}_1$ (see Fig. B-1), which are not symmetry-related in our quantum Hall setting. In our study we are instead focusing on the Dirac cones near $\bar{X}_2$, whose degeneracy is symmetry-protected as explained in Sec. B.1. These cones can acquire a mass via the Zeeman effect, but the experiment by Okada *et al.* [192] suggests that it is too small to be observed. A rough estimate with the vacuum Zeeman effect would give $\lambda \sim 0.01$, and thus in the main text we decide to assume $\lambda = 0$. The values of v_x and v_y have been obtained by Liu *et al.* by fitting with *ab initio* calculations [190].

For the effective Dirac Hamiltonian (around $\bar{\Lambda}$) that we are considering, $v_x = 1.3$ eV and $v_y = 0.83$ eV. Thus, the anisotropy $v_x/v_y = 1.6$.

B.1.4 Relation between the local impurity dipole and the bulk adiabatic dipole

Here we present more details of the derivations of Eqs.(4) and (6) in the main text.

Let us begin with the bulk adiabatic dipole moment introduced in the modern theory of polarization [193]. Since the tilt of Dirac cone in our model breaks inversion symmetry in the p_x-direction, electric polarization is non-vanishing only in the y-direction and we thus focus only on that component. Following the conventional Berry phase approach, we have [194]:

$$D_y = ie\frac{l_B^2}{L_x}\int_0^{L_x/l_B^2} dk_y \ \langle u_{k_y}|\, \partial_{k_y}\, |u_{k_y}\rangle \tag{B.5}$$

where $|u_{k_y}\rangle$ is the Bloch wavefunction in a gauge which is invariant under translation in y-direction. In this gauge, the complete wavefunction is $\psi_{k_y}(x,y) = \frac{e^{ik_y y}}{\sqrt{L_y}} u_{k_y}(x)$. Making use of $u_{k_y}(x) = u_0(x - k_y\_B^2)$, one can recast Eq.(B.5) into the following form:

$$\begin{aligned} D_y &= -iel_B^2 \int d^2r\ \psi^*_{k_y}(x,y)\partial_x\psi_{k_y}(x,y) \\ &= el_B^2\, \langle\psi_{k_y}|\, p_x\, |\psi_{k_y}\rangle \end{aligned} \tag{B.6}$$

Expressing the momentum operator in terms of inter-Landau level ladder operators as in Eq. (B.2), and acting it on the first-order perturbed Landau orbitals in Eq. (B.6), one would obtain Eq. (4) of the main text:

$$\mathbf{D}_n = \tilde{s}_n\sqrt{2}\ \tau\ e\ l_B\ \left(\frac{2\lambda^2 + 3|n|}{\sqrt{\lambda^2 + |n|}}\right)\sqrt{\frac{v_y}{v_x}}\hat{\mathbf{y}}, \tag{B.7}$$

where $\tilde{s}_n = \mathrm{sgn}(n)$ (and $\tilde{s}_0 = 1$).

Next we turn to the local impurity dipole moment, which is defined as

$$D_y^{\text{imp}} = e(\langle\tilde{\psi}_1|\,\hat{y}\,|\tilde{\psi}_1\rangle + \langle\tilde{\psi}_2|\,\hat{y}\,|\tilde{\psi}_2\rangle), \tag{B.8}$$

where $\tilde{\psi}_{1,2}$ are the two impurity states bound to the delta-potential defect. Expressing the position operator $\hat{y}$ in terms of the guiding-center operator and the momentum operator: $\hat{y} = \hat{R}_y - l_B^2\hat{p}_x$, it follows that:

$$D_y^{\text{imp}} = e(\langle\tilde{\psi}_1|\,\hat{R}_y\,|\tilde{\psi}_1\rangle + \langle\tilde{\psi}_2|\,\hat{R}_y\,|\tilde{\psi}_2\rangle) - 2D_y. \tag{B.9}$$

Notice that the guiding-center operator can be expressed in terms of *intra*-Landau level ladder operators: $\hat{R}_y = il_B(b^\dagger - b)/\sqrt{2}$. To proceed analytically, we first consider the massless limit and to leading order in the tilt of Dirac cone. The impurity states for the n-th Landau level have the following expressions:

$$\tilde{\psi}_1 = -s_n\frac{i\tau\alpha_{-2}}{\sqrt{2}}\psi_{n,n-2} + (-\frac{1}{\sqrt{2}} + \frac{\tau n}{\sqrt{2}})\psi_{n,n-1} + s_n i(\frac{1}{\sqrt{2}} + \frac{\tau n}{\sqrt{2}})\psi_{n,n} - \frac{\tau\alpha_1}{\sqrt{2}}\psi_{n,n+1} \tag{B.10a}$$

$$\tilde{\psi}_2 = s_n\frac{i\tau\alpha_{-2}}{\sqrt{2}}\psi_{n,n-2} + (\frac{1}{\sqrt{2}} + \frac{\tau n}{\sqrt{2}})\psi_{n,n-1} + s_n i(\frac{1}{\sqrt{2}} - \frac{\tau n}{\sqrt{2}})\psi_{n,n} - \frac{\tau\alpha_1}{\sqrt{2}}\psi_{n,n+1} \tag{B.10b}$$

where $s_n = \text{sgn}(n)$. Note that $\psi_{n,m}$ and α_i are defined in Eqs. (B.6) and (B.7) respectively. Combining Eqs. (B.9) and (B.10), we obtain:

$$\mathbf{D}_n^{\text{imp}} = \frac{2}{3}\mathbf{D}_n \tag{B.11}$$

in the massless limit. For the massive case, the algebra becomes complicated without specifying an explicit LL index. For $n = 1$ and $n = 2$, we have obtained explicit analytic expressions for the impurity states and evaluated the impurity dipole. The

result suggests that

$$\mathbf{D}_n^{\text{imp}} = \frac{2|n|}{3|n| + 2\lambda^2}\mathbf{D}_n. \tag{B.12}$$

The validity of this expression is further checked numerically for higher Landau levels (see Fig. B-2). It is also worth pointing out that for higher Landau levels, we are usually in the regime where $\lambda \ll \sqrt{n}$, so the relation in Eq. (B.11) for the massless limit is a good approximation.

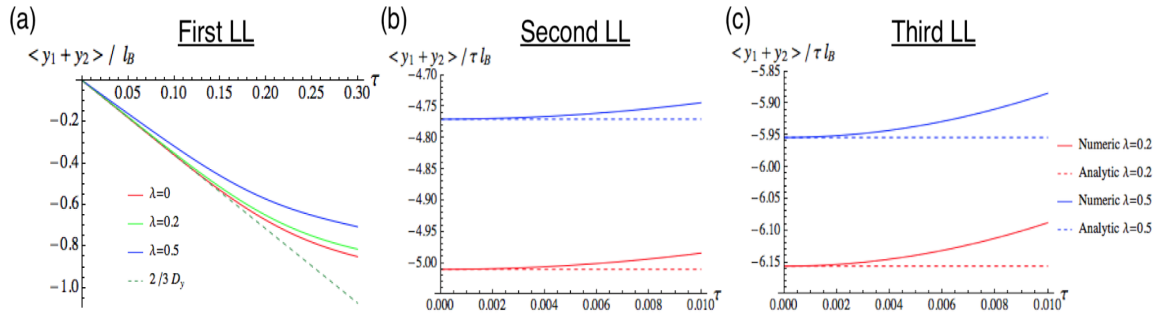

Figure B-2: Numerical checks of the relation between impurity dipole and bulk adiabatic dipole. (a) Impurity dipole D_y^{imp} (with e set to 1) as a function of tilt τ, for the first Dirac Landau level in the valence band with various mass λ. The dashed line is given by the analytic result in Eq. (B.11). (b) and (c): D_y/τ as a function of tilt τ for the second and third Landau levels in the valence band respectively. Solid lines represent results from solving the impurity states numerically, while dashed lines are generated using the analytic formula in Eq. (B.12). For small enough tilt such that the first-order perturbation theory is sufficient, it is shown that the analytic result complies with the numerical calculation. Note that the figures here show the analysis for Landau levels in the valence band ($n < 0$), which differ from the situation in the conduction band ($n > 0$) simply by a minus sign in the dipole.

B.1.5 Differences in the two notions of electric dipole moment

To further clarify the difference between the adiabatic bulk dipole moment (following the modern theory of polarization) and the impurity dipole moment $\mathbf{D}^{\text{imp}}$ introduced

in this paper, we consider a toy model with a parabolic dispersion:

$$H = \frac{(p_x - a_x)^2}{2m_x} + \frac{p_y^2}{2m_y} \tag{B.1}$$

The parameter a_x plays a similar role as the tilt δv_x in the Dirac Hamiltonian.

Now, apply a magnetic field $B\hat{z}$ on the system. Denote a Landau orbital as $|\psi\rangle$ for a_x=0, and the corresponding Landau orbital when a_x is tuned from zero to some finite value as $|\tilde{\psi}\rangle$. According to the polarization theory based on Berry phase, the difference of polarization between these two Landau orbitals is:

$$\begin{aligned}
\Delta D_y &= -el^2[\langle\tilde{\psi}|\ p_x\ |\tilde{\psi}\rangle\ - \langle\psi|\, p_x\, |\psi\rangle] \\
&= -el^2[\langle\tilde{\psi}|\ \tilde{p}_x + a_x\ |\tilde{\psi}\rangle\ - \langle\psi|\, p_x\, |\psi\rangle] \\
&= -el^2[\langle\tilde{\psi}|\ \tilde{p}_x\ |\tilde{\psi}\rangle\ - \langle\psi|\, p_x\, |\psi\rangle + a_x] \\
&= -\frac{a_x}{B}
\end{aligned} \tag{B.2}$$

The last equality is obtained because $\tilde{p}_x = p_x - a_x$ is just a gauge transformation, while the expectation value $\langle\psi|\, p_x\, |\psi\rangle$ should be gauge-invariant.

However, this dipole moment does not reflect the inversion asymmetry of the Landau orbital. In this example, there is simply no inversion asymmetry to begin with, and this can be verified if one examine $\mathbf{D}^{\text{imp}} = e\langle\phi|\mathbf{r}|\phi\rangle$, for the Landau orbital bound to a delta-potential impurity. By a proper gauge transformation, one can move the center of unperturbed Landau orbitals to the impurity site, irrespective of what a_x is. After all, the presence of a_x can be viewed as a gauge-transformation. In the presence of a delta-function impurity, only one state in each Landau level is bound to the impurity. That is the state $\phi_{n,n}$, which has a non-zero amplitude at the origin where the impurity sits. As this state is inversion symmetric, and the perturbation (i.e. the delta potential) preserves this symmetry, the bound state should also be inversion symmetric. Thus $\mathbf{D}^{\text{imp}} = \mathbf{0}$.

In this extreme example, which can be considered as the parabolic limit ($\lambda \to \infty$) of the Dirac Hamiltonian, $\mathbf{D}$ measures solely the effect of Landau orbital displace-

ment, which cannot be detected in a quantum Hall system due to edge screening. On the other hand, $\mathbf{D}^{\text{imp}}$ measures only the inversion asymmetry of Landau orbitals, and therefore gives a local experimental signature for quantum Hall ferroelectrics.

B.1.6 Numerical Setup of Exact Diagonalization

Anisotropic parabolic dispersions

To exact-diagonalize the Hamiltonian with Coulomb interaction, one has to project the Coulomb term onto the Landau orbitals. In the main text, we deal with Landau levels arising from the tilted Dirac cones dispersion, while in this appendix we will also consider the case with parabolic dispersion. The parabolic case is the cornerstone for case with tilted Dirac cones dispersion, since the Dirac Landau orbitals are spinors consisting of parabolic Landau orbitals. The parabolic dispersion Hamiltonian is:

$$H = \frac{1}{2m^*} p_a g_{ab} p_b = \frac{1}{l_B^2 m^*}(a^\dagger a + \frac{1}{2}) \tag{B.1}$$

where $p = \nabla/i - eA$, $g = Q^T S^2 Q$ is a 2×2 tensor, $Q \in SO(2)$ describes the rotation around principal axes in real space, the valleys we are interested in are vertical oriented, so we can set the real space axes along the principal axes of rotation, thus $Q = I$, and simply $g = S^2$. $S = diag\{(m_x/m_y)^{1/4}(m_y/m_x)^{1/4}\}$ is the mass tensor for the valley , effective mass $m^* = (m_x m_y)^{1/2}$. We introduce the mass ratio: $\alpha = m_x/m_y$ that specifies aspect ratio of the valley. The rescaled momenta along the principal axes of the tensor $\pi_a = S_{ab} p_b$ satisfy:

$$[\pi_a, \pi_b] = i l_B^{-2} \epsilon_{ab} \tag{B.2}$$

and the LL lowering operator is:

$$a = \frac{l_B}{\sqrt{2}}(\pi_x + i\pi_y), \quad [a, a^\dagger] = 1 \tag{B.3}$$

Numerically, the electrons are on the 2D surface of torus, $L_x(L_y)$ represents the circumference of the torus along $x(y)$ direction and they satisfy relation $L_xL_y = 2\pi N_0$, N_0 represents the number of orbitals for each valley.

Choosing the Landau gauge, $\vec{A} = (0, x)B$, the wavefunction of LL orbital is expressed as:

$$\phi^{\alpha}_{n,j}(r) = \left(\frac{2\pi}{L_y l_B}\right)^{1/2} \Sigma^{+\infty}_{k=-\infty} \overline{H_n}\left[\frac{x - kL_x - X_j}{\alpha^{1/4} l_B}\right] \times \exp[i(X_j + kL_x)y/l_B^2 - (X_j + kL_x - x)^2/(2\alpha^{1/2} l_B^2)] \tag{B.4}$$

where $X_j = \frac{2\pi l_0^2 j}{L_y}$ to fulfill the periodic boundary condition, $\overline{H_n}$ is the physicist's Hermite polynomial that has been normalized so that:

$$\int_{-\infty}^{+\infty} \left(\overline{H_n}(x)\right)^2 e^{-x^2} dx = 1 \tag{B.5}$$

With $\phi^{\alpha}_{n,j}(r)$ normalized as $\int_0^{L_y} dy \int_0^{L_x} dx |\phi^{\alpha}_{n,j}(r)|^2 = 2\pi$, when a Landau level is completely filled and thus the electron density is uniformly distributed, $\int_0^{L_y} dy \int_0^{L_x} dx \sum_j |\phi^{\alpha}_{n,j}(r)|^2 = 2\pi N_0 = L_x L_y$ would then imply $\sum_j |\phi^{\alpha}_{n,j}(r)|^2 = 1$.

Next, we define f_{nm} as the form factor for the parabolic Landau levels calculated in the Landau gauge:

$$\begin{aligned} f_{nm}(\mathbf{q}^{\alpha}) &= \langle n, \alpha | e^{i l_B^2 \mathbf{q}^{\alpha} \cdot \boldsymbol{\pi}} | m, \alpha \rangle \\ &= e^{-l_B^2 (q_y^{\alpha})^2/4} \int_{-\infty}^{+\infty} \overline{H_m}(x - \frac{q_y^{\alpha}}{2}) \overline{H_n}(x + \frac{q_y^{\alpha}}{2}) e^{-x^2} e^{i q_x^{\alpha} x} dx \end{aligned} \tag{B.6}$$

where the wavevector $\mathbf{q}^{\alpha}$ is not the natural wavevector $\mathbf{q}$ but rotated as

$$\mathbf{q}^{\alpha} = -S^{-1} \epsilon \mathbf{q} \tag{B.7}$$

where ϵ is the rank-2 levi-civita symbol, Q and S are the matrices associated with the mass ratio α. This definition will become clear later when we project the electron interaction on the LLs.

Tilted Dirac cone dispersion

The massless Dirac Hamiltonian is just Eq. (B.1) with $\lambda = 0$. Similar to the case with a parabolic Hamiltonian in Eq. (B.1), here we would define $S = diag\{(v_x/v_y)^{1/2}, (v_y/v_x)^{1/2}\}$ and rescale the momentum by $\pi_a = S_{ab}p_b$, which explains Eq. (B.2). One can relate the mass ratio α in the anisotropic parabolic dispersion and velocity ratio $r = v_x/v_y$ in the Dirac dispersion as: $\alpha = r^2$.

Tilting of the Dirac cone along the x-direction is described by the following perturbation:

$$H_1 = \delta v_x p_x = \delta v_x \sqrt{\frac{v_y}{v_x}} \frac{(a + a^\dagger)}{\sqrt{2} l_B} = \tau \frac{\sqrt{2} v}{l_B} (a + a^\dagger) \tag{B.8}$$

where $\tau = \delta v_x/(2v_x)$. Using the general expression for the tilted Dirac LL in Eq. (B.6), we have the following expression for the $n = +3$ Dirac Landau level:

$$|+3, \tau\rangle = \frac{1}{\sqrt{2}} \begin{pmatrix} |3\rangle + \tau(-4\sqrt{3}|4\rangle + 5|2\rangle) \\ |2\rangle + \tau(2\sqrt{6}|1\rangle - 7|3\rangle) \end{pmatrix} \tag{B.9}$$

Here, for simplicity, we have suppressed the intra-Landau level indices and the mass ratio α that would label the parabolic Landau orbitals. The form factor for the Dirac Landau level is then obtained as follows:

$$\begin{aligned} F^3(\mathbf{q}^\alpha, \tau) &= \langle +3, \tau | e^{i l_B^2 \mathbf{q}^\alpha \cdot \boldsymbol{\pi}} | +3, \tau \rangle \\ &= \frac{1}{2}[f_{33} + f_{22} - 2\tau(f_{32} + f_{23}) - 4\sqrt{3}\tau(f_{34} + f_{43}) + 2\sqrt{6}\tau(f_{12} + f_{21})] \end{aligned} \tag{B.10}$$

where f_{nm} is the form factor for the parabolic Landau levels (Eq. B.6).

Impurity potential

The impurity potential is $U(\mathbf{r}) = V_0 l_B^2 \delta(\mathbf{r})$. The matrix elements of impurity potential projected to the n-th and m-th parabolic Landau levels are:

$$U^{\alpha}_{j_1,j_2,n,m} = V_0 \frac{2\pi l_B}{L_y} \Sigma_{l=-\infty}^{+\infty} \Sigma_{k=-\infty}^{+\infty} \overline{H_n}\left[\frac{X_{j_1}+lL_x}{l_B\alpha^{1/4}}\right] \times \overline{H_m}\left[\frac{X_{j_2}+kL_x}{l_B\alpha^{1/4}}\right] e^{-\frac{(X_{j_1}+lL_x)^2+(X_{j_2}+kL_x)^2}{2l_B^2\sqrt{\alpha}}} \tag{B.11}$$

In the parabolic dispersion case, one only need to consider the case $n = m$, and in the main text we focus on the lowest Landau level, so $n = m = 0$; on the other hand, in the tilted Dirac case there exist non-trivial terms with $n \neq m$, the impurity matrix elements $\langle +3, \tau|\hat{U}(\mathbf{r})| + 3, \tau\rangle_{j_1,j_2}$ are linear combinations of $U_{j_1,j_2,n,m}$ with $n, m = 1, 2, 3, 4$, which is similar to the form factor in Eq. (B.10).

Coulomb interaction

The Coulomb interaction in a finite system has the form

$$V(\mathbf{r}) = \frac{1}{L_x L_y} \sum_{\mathbf{q}} V(q) e^{i\mathbf{q}\cdot\mathbf{r}} \tag{B.12}$$

where $V(q) = \frac{2\pi e^2}{\epsilon q}$, for finite size torus with the circumference L_x and L_y. Here $\mathbf{q} = (\frac{2\pi s}{L_x}, \frac{2\pi t}{L_y})$ takes discrete values to ensure the periodicity.

The projected Coulomb interaction between two electrons in the valleys i and j (i, j can either be the same valley or two different valleys) into the n-th Landau level has the form:

$$P_n V(\mathbf{r}_i - \mathbf{r}_j) P_n = \frac{1}{L_x L_y} \sum_{\mathbf{q}} V(\mathbf{q}) F_i^n(\mathbf{q}_i) F_j^n(\mathbf{q}_j)^* e^{i\mathbf{q}\cdot(\mathbf{R}_i - \mathbf{R}_j)} \tag{B.13}$$

Here we have introduced the guiding center operator $\mathbf{R}_i$ for valley i, which is related to the position operator as follows:

$$\mathbf{r}_i \equiv \mathbf{R}_i - l_B^2 \epsilon \mathbf{p}_i = \mathbf{R}_i - l_B^2 \epsilon S_i^{-1} \boldsymbol{\pi}_i \tag{B.14}$$

where ϵ is the rank-2 levi-civita symbol and S_i is the S tensor associated to valley i, which has been defined earlier for both parabolic and Dirac dispersions. Accordingly, wavevector $\mathbf{q}_i$ is defined as:

$$\mathbf{q}_i = -S_i^{-1}\epsilon\mathbf{q} \tag{B.15}$$

For the numerical results presented in the main text, the valleys have the same velocity ratio r (or mass ratio $\alpha = r^2$) and opposite τ. Thus we have $\mathbf{q}_i = \mathbf{q}_j = \mathbf{q}^\alpha, F^n_{i/j}(\mathbf{q}^\alpha) = F^3(\mathbf{q}^\alpha, \pm\tau)$. While for the numerics to be presented in the next section for anisotropic parabolic dispersion at $n = 0$ LL, different valleys have different mass ratio α and β, where $\beta = \frac{1}{\alpha}$ for the two orthogonal-orientated valleys of interest. There we have $\mathbf{q}_{i/j} = \mathbf{q}^{\alpha/\beta}$, and $F^n_{i/j} = f_{00}$.

B.1.7 Quantum Hall Nematics with Anisotropic Parabolic Dispersions

After considering electron-electron interaction in ferroelectric states in the main text, here we illustrate a simpler scenario where the anisotropic parabolic dispersion is used so that the impurity only hosts a single bound state. The two valleys A and B are parabolic dispersive with the same aspect ratio, but vertical elliptical axes, meaning that if we choose the principal axes along the same direction for two valleys, there mass ratio will satisfy $\alpha = \frac{1}{\beta}$. A smaller system size with $N_0 = 20$ single-valley orbitals is enough to demonstrate this case. The corresponding energy spectra with disorder are shown in Fig. B-3, and some representative tunneling density profiles are shown in Fig. B-4, with various mass ratios. Again, just like what happens in the ferroelectric state around an impurity, when the impurity potential is larger than a certain threshold a quasihole state becomes the new ground state. Adding an electron to this state would lead to an exciton state, and the resulting density profile can be captured by STM measurements.

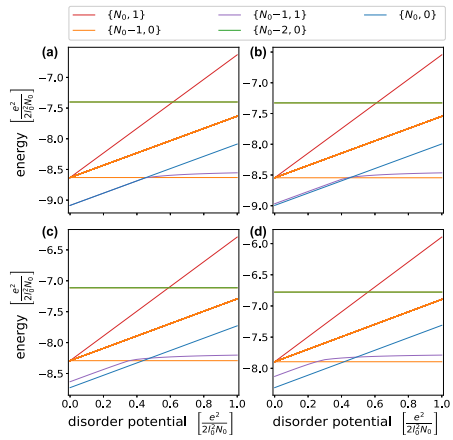

Figure B-3: The energy spectra with increasing impurity potentials, as indicated in the legend, blue lines represent $\{N_0, 0\}$, red lines $\{N_0, 1\}$, orange lines $\{N_0 - 1, 0\}$, purple lines $\{N_0 - 1, 1\}$ and green lines $\{N_0 - 2, 0\}$. The mass ratios($\alpha = m_x/m_y$) in panels (a),(b),(c),(d) are $1, 2, 4, 8$, respectively. The orbital number $N_0 = 20$.

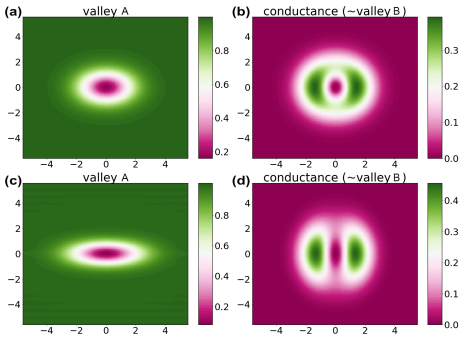

Figure B-4: The tunneling matrix elements from the ground state $\{N_0 - 1, 0\}$ to the excitonic state $\{N_0 - 1, 1\}$ for different mass ratio: $\alpha = 2$ in (a, b) and $\alpha = 8$ in (c,d), which are proportional to the differential conductance obtained by direct STM measurements. The strength of impurity potential is set to be $0.6\frac{e^2}{2l_B^2 N_0}$ and the length scale is in the unit of l_B.

Appendix C

Appendices of Chapter 5

C.1 Angel dependent lattice structures for twisted homobilayer MoS_2

We have discussed the lattice relaxation from DFT simulation in the main text and given the twist angle dependence of layer distance d_{far} and d_{near} at MM and MX(XM) region, respectively. In the moiré superlattice, the vertical layer spacing of the metallic atom as a function of the inplane coordinate $d_(\mathbf{r})$ can be obtained from the zeroth and first Fourier expansion with the two-dimensional reciprocal lattice vectors $\mathbf{G}_j^m$ in the lateral cell:

$$d(\mathbf{r}) = c_0 + c_1 \sum_{j=1}^{3} \left\{ \cos\left(\mathbf{G}_j^m \mathbf{r}\right) \right\} \tag{C.1}$$

We have c_1 for three reciprocal lattice vectors due to the C_{3z} in the moiré superlattice. Here we expand from the MM region so that $d(0) = d_{far}$, $d(r_{\mathrm{MX}}) = d_{near}$.

We first optimize the structures of heterobilayer with relatively large twist angles from 7.34° to 2.876°. At infinite wavelength limit $\theta \sim 0$, the spatial variation of layer spacing can be extracted for the shifted configuration in the untwisted bilayer. Then the Fourier coefficients c_0, c_1 can be calculated from relaxed structures at a series of twist angles. We find that $c_0 \approx 6.19$ Angstroms for $\theta < 5$, and c_1 is monotonously

increasing when θ is reduced as shown in Table C.1

θ	0°	2.876°	3.15°	3.48°	3.89°	4.41°	5.08°	6.0°	7.34°
c_0	6.19	6.19	6.19	6.19	6.19	6.19	6.19	6.20	6.23
c_1	0.073	0.069	0.068	0.067	0.064	0.061	0.058	0.056	0.049
L_m	∞	63.5	58.0	52.5	47.0	41.4	35.9	30.4	24.9
N_m	∞	2382	1986	1626	1302	1014	762	546	366

Table C.1: Fourier coefficients c_0, c_1 (in Angstroms) for inplane coordinate dependent vertical layer spacing, moire wavelength L_m (in Angstroms) and the number of atoms N_m in the commensurate structures.

We can further fit the expression of Fourier coefficients c_0, c_1 from discrete twist angles to approximate the out-of-plane corrugation at a general twist angle. This expression for lattice structures can be used to perform more realistic atomic tight-binding simulation [142, 141].

C.2 Density functional theory calculation

Density functional calculations are performed using Perdew-Burke-Ernzerhof generalized gradient approximation[195] with the vdW correction incorporated by the vdW-DF (optB86) functionals [146] as implemented in the Vienna Ab *initio* Simulation Package[147]. Pseudopotentials are used to describe the electron-ion interactions. We have calculated eight commensurate structures with twist angle from 7.34° with 366 atoms to 2.876° with 2382 atoms, for the band structure after lattice relaxation.

In bilayer $MoSe_2$ and WS_2, the valence band maximum also locates at Γ point [138]. As presented in the previous DFT work [138], the valence band maximum at MX (XM) is higher than MM region in both $MoSe_2$ and WS_2, which means that the antibonding orbitals at MX and XM form an emergent honeycomb lattice [140] as the twisted MoS_2 investigated in this work. While in twisted bilayer WSe_2, the valence band maximum locates at K valley due to the large spin splitting up to 466 meV [196].

C.3 Field tunable charge transfer gap

In this section, we present the gating field dependent charge transfer gap at the long wavelength region. In Fig. C-1 for $\theta = 2^\circ$ with wavelength $L_m = 9.1$ nm, the bandwidth without field is 13 meV. The gating filed $E_d = 1$ V/nm creates a charge transfer gap Δ up to 5.3 meV, which means that the critical Δ_c for the phase transition at $n = 1/2, 2/3$ can be reached experimentally already at $L_m = 9.1$ nm.

We plot the continuum band structure at $\theta = 2^\circ$ with $E_d = 0.5$ V/nm in Fig. C-1b, where the charge transfer gap is comparable as the than the bandwidth of top moiré band. At $n = 1$, the large onsite interaction $U > \Delta$ gives rise to a charge transfer insulator.

C.4 Interaction strength under gate screening

In the deep potential limit, the size of Wannier orbital ξ is much smaller than the moiré periodicity and the point charge approximation is used to calculated extended interaction $V(r)$ screened by a pair of metallic gates with distance $\pm d$:

$$V(r) = \frac{e^2}{\epsilon} \sum_{z \in \mathbb{Z}} \frac{(-1)^z}{\sqrt{r^2 + (2dz)^2}} \tag{C.2}$$

Here the unit is $\frac{e^2}{\epsilon L_{\mathrm{M}}} = \frac{1440}{\epsilon (L_m/nm)}$meV, and we take dielectric constant as $\epsilon = 5$. At $r \gg d$, the Coulomb interaction $V(r)$ decays exponentially as shown in Fig. C-2a.

C.5 Monte Carlo simulation for ground state charge order

Classical Monte Carlo (MC) simulation with Metropolis transition rule is performed at $N \times N$ honeycomb lattice with periodic boundary conditions. To avoid the truncation problem, we drop the long-range interaction V_n only when $V_n < 0.001 V_1$. A single step MC move is generated by removing an occupied charge and add an

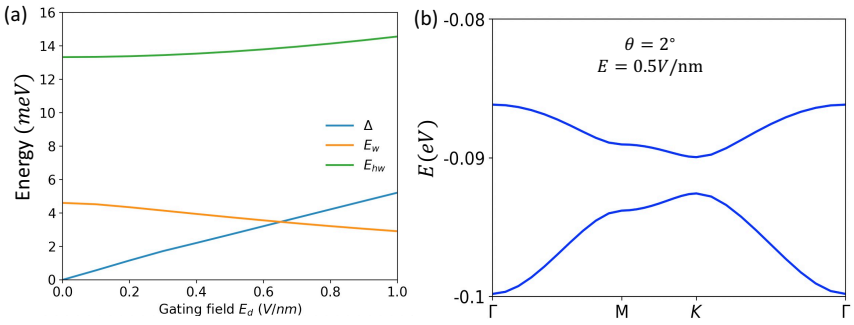

Figure C-1: (a)Gating field dependent charge transfer gap Δ, bandwidth for the top moiré band E_w and bandwidth of two moiré bands of the honeycomb lattice E_{hw}; (b) Continuum model band structures for $\theta = 2°$ and gating field $E_d = 0.5$ V/nm.

unoccupied charge randomly, the acception rate is determined from the Metropolis transition rule. We test Coulomb interactions with various screening gate distances: $d = 1/2L_m, L_m, 2L_m, 4L_m, 5L_m, 6L_m, 10L_m$. It is found that screening distance only changes the ground state charge order at $n = 1/4$ but not at other fillings. However, we note that a smaller gate distance would reduce the critical charge transfer gap for phase transition at fixed filling $\Delta = 1/2, 2/3$, and therefore can control the sublattice/layer charge distribution.

As we are interested in the ground state charge distribution, we perform the cooling down from $T = \frac{e^2}{\epsilon L_m}$ to $T = 10^{-4}\frac{e^2}{\epsilon L_m}$ to avoid the possible trapped states at the local minimum. At every temperature, $1e^4 * N * N$ local updates are performed as warm-up steps. When reaching at $T = 10^{-4}\frac{e^2}{\epsilon L_m}$, $1e^6 * N * N$ sampling steps are taken to identify the lowest energy configuration.

To identify the lowest energy ground state charge patterns, we perform the simulations with system size N from 30 to 120, and compare their lowest energy charge patterns. At $n = 1/4, 1/3$ and 1, charges are spontaneously polarized to one sublattice site even at $\Delta = 0$. While at $n = 1/2$ and $2/3$, we find two sublattice sites are equally occupied. To locate the critical charge transfer gap Δ_c for the fully sublattice polarized state, we perform MC simulations with varying Δ. The exact expression of Δ_c can be also obtained by comparing $\Delta = 0$ charge order and fully sublattice polarized charge order. These two values are found to be consistent.

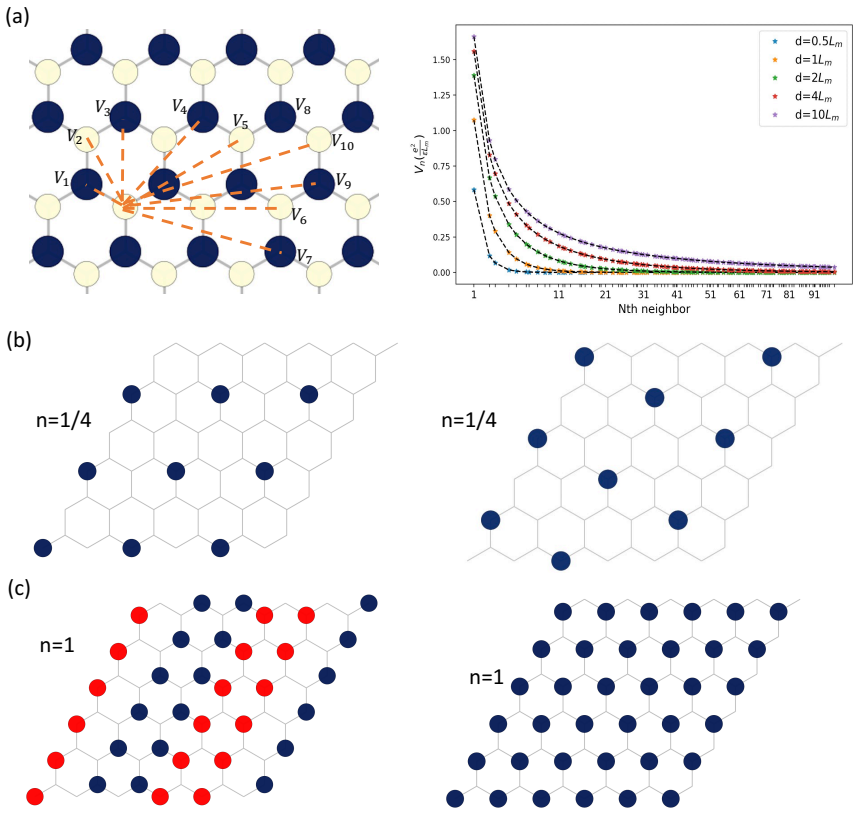

Figure C-2: (a) Interaction within two sublattice sites, and Nth neighbour interaction strength in the unit of $\frac{e^2}{\epsilon L_m}$ with gate screening distance $d = (1/2, 1, 2, 4, 10)L_m$. Ground state charge order at filling (b) n=1/4 with gating distance $d < 5L_m$ and $d > 5L_m$ (c) n=1 with $V_1 - V_2$ model and long range interaction.

C.6 Charge orders at n=1/4, 1/3 and 1

At filling factor $n = 1/4$, the charges are all filled to one sublattice site, forming the enlarged triangular lattice with 2×2 periodicity up to $d < 5L_m$. For $d > 5L_m$, the $\sqrt{3} \times 2$ rectangular configuration appears to be the ground state as shown in Fig. C-2b. The phase transition between these two charge orders can be realized also in the previous $WSe2_2/WS_2$ heterobilayer.

At filling factor $n = 1/3$, we find the ground state as a charge density wave state with $\sqrt{3} \times \sqrt{3}$ periodicity for all gate distances as the case in $WSe2_2/WS_2$ [132, 134]. We note that even in the honeycomb lattice with equal site potential, the classical ground state charge orders at $n < 1/2$ break the sublattice symmetry and spontaneous filled to one sublattice site. When the out of plane gating field is applied

to the superlattice, the tiny potential difference between two sites would stabilize the proposed sublattice-symmetry breaking insulating states.

At $n = 1$, it has been shown that the system favors fully sublattice polarized states even at $\Delta = 0$ for all studied gate distances. We further analyze the possible charge order at $n = 1$ involving two honeycomb sites. The microscopic phase separation with broken rotational symmetry in Fig. C-2c can be the ground state in the $V_1 - V_2$ model with $V_1 < 4V_2$, which happens at the strong screening.

Bibliography

[1] C. L. Degen, F. Reinhard, and P. Cappellaro. Quantum sensing. *Rev. Mod. Phys.*, 89:035002, Jul 2017.

[2] Hao Luo, Peng Yu, Gen Li, and et al. Topological quantum materials for energy conversion and storage. *Nat Rev Phys*, 4(9):611–624, 2022.

[3] Chetan Nayak, Steven H. Simon, Ady Stern, Michael Freedman, and Sankar Das Sarma. Non-abelian anyons and topological quantum computation. *Rev. Mod. Phys.*, 80:1083–1159, Sep 2008.

[4] Ryszard Horodecki, Paweł Horodecki, Michał Horodecki, and Karol Horodecki. Quantum entanglement. *Rev. Mod. Phys.*, 81:865–942, Jun 2009.

[5] Charles H Bennett. Quantum information. *Physica Scripta*, 1998(T76):210, jan 1998.

[6] A.Yu. Kitaev. Fault-tolerant quantum computation by anyons. *Annals of Physics*, 303(1):2–30, 2003.

[7] Philipp Hauke, Markus Heyl, Luca Tagliacozzo, and Peter Zoller. Measuring multipartite entanglement through dynamic susceptibilities. *Nat. Phys.*, 12(8):778–782, 2016.

[8] Luuk J. P. Ament, Michel van Veenendaal, Thomas P. Devereaux, John P. Hill, and Jeroen van den Brink. Resonant inelastic x-ray scattering studies of elementary excitations. *Rev. Mod. Phys.*, 83:705–767, Jun 2011.

[9] Jordyn Hales, Utkarsh Bajpai, Tongtong Liu, Denitsa R. Baykusheva, Mingda Li, Matteo Mitrano, and Yao Wang. Witnessing light-driven entanglement using time-resolved resonant inelastic X-ray scattering. *Nat. Commun.*, 14(1):3512, June 2023.

[10] Yao Wang, Yuan Chen, Thomas P. Devereaux, Brian Moritz, and Matteo Mitrano. X-ray scattering from light-driven spin fluctuations in a doped Mott insulator. *Commun. Phys.*, 4(1):212, 2021.

[11] Chunjing Jia, Krzysztof Wohlfeld, Yao Wang, Brian Moritz, and Thomas P. Devereaux. Using rixs to uncover elementary charge and spin excitations. *Phys. Rev. X*, 6:021020, May 2016.

[12] Juan Carrasquilla. Machine learning for quantum matter. *Advances in Physics: X*, 5(1):1797528, 2020.

[13] Mario Geiger, Tess Smidt, Alby M., Benjamin Kurt Miller, Wouter Boomsma, Bradley Dice, Kostiantyn Lapchevskyi, Maurice Weiler, Michał Tyszkiewicz, Simon Batzner, Martin Uhrin, Jes Frellsen, Nuri Jung, Sophia Sanborn, Josh Rackers, and Michael Bailey. e3nn/e3nn: 2021-08-27, August 2021.

[14] Nathaniel Thomas, Tess Smidt, Steven Kearnes, Lusann Yang, Li Li, Kai Kohlhoff, and Patrick Riley. Tensor field networks: Rotation-and translation-equivariant neural networks for 3d point clouds. *arXiv preprint arXiv:1802.08219*, 2018.

[15] Luigi Amico, Rosario Fazio, Andreas Osterloh, and Vlatko Vedral. Entanglement in many-body systems. *Rev. Mod. Phys.*, 80:517–576, May 2008.

[16] Ryszard Horodecki, Paweł Horodecki, Michał Horodecki, and Karol Horodecki. Quantum entanglement. *Rev. Mod. Phys.*, 81:865–942, Jun 2009.

[17] V. Vedral, M. B. Plenio, M. A. Rippin, and P. L. Knight. Quantifying entanglement. *Phys. Rev. Lett.*, 78:2275–2279, Mar 1997.

[18] Alexei Kitaev and John Preskill. Topological entanglement entropy. *Phys. Rev. Lett.*, 96(11):110404, 2006.

[19] Ingemar Bengtsson and Karol Zyczkowski. Multipartite entanglement. *Geometry of Quantum States*, pages 493–543, 2017.

[20] Philipp Hyllus, Wiesław Laskowski, Roland Krischek, Christian Schwemmer, Witlef Wieczorek, Harald Weinfurter, Luca Pezzé, and Augusto Smerzi. Fisher information and multiparticle entanglement. *Phys. Rev. A*, 85:022321, Feb 2012.

[21] John Schliemann, J. Ignacio Cirac, Marek Kuś, Maciej Lewenstein, and Daniel Loss. Quantum correlations in two-fermion systems. *Phys. Rev. A*, 64:022303, Jul 2001.

[22] K. Eckert, J. Schliemann, D. Bruß, and M. Lewenstein. Quantum correlations in systems of indistinguishable particles. *Ann. Phys.*, 299(1):88–127, 2002.

[23] H. M. Wiseman and John A. Vaccaro. Entanglement of indistinguishable particles shared between two parties. *Phys. Rev. Lett.*, 91:097902, Aug 2003.

[24] Christina V. Kraus, Michael M. Wolf, J. Ignacio Cirac, and Géza Giedke. Pairing in fermionic systems: A quantum-information perspective. *Phys. Rev. A*, 79:012306, Jan 2009.

[25] Alfréd Rényi. On measures of entropy and information. *Proceedings of the 4th Berkeley Symposium on Mathematical Statistics and Probability*, 1:547–561, 1961.

[26] Asutosh Kumar. Multiparty quantum mutual information: An alternative definition. *Phys. Rev. A*, 96:012332, Jul 2017.

[27] Jens Eisert, Marcus Cramer, and Martin B. Plenio. Area laws for the entanglement entropy—a review. *Rev. Mod. Phys.*, 82(1):277–306, 2010.

[28] Bei Zeng, Xie Chen, Duan-Lu Zhou, and Xiao-Gang Wen. *Quantum Information Meets Quantum Matter*. Springer, New York, 2019. Also available with ISBN 978-1-4939-9084-9.

[29] Huan-Cheng Jiang, Zhenghan Wang, and Leon Balents. Identifying topological order by entanglement entropy. *Nature Physics*, 8(11):902–905, 2012.

[30] Michael Seevinck and Jos Uffink. Sufficient conditions for three-particle entanglement and their tests in recent experiments. *Phys. Rev. A*, 65(1):012107, December 2001.

[31] Otfried Gühne, Mátyás Mechler, Géza Tóth, and Peter Adam. Entanglement criteria based on local uncertainty relations are strictly stronger than the computable cross norm criterion. *Phys. Rev. A*, 74(1):010301, July 2006.

[32] W. Dür, J. I. Cirac, and R. Tarrach. Separability and Distillability of Multiparticle Quantum Systems. *Phys. Rev. Lett.*, 83(17):3562–3565, October 1999.

[33] Gábor Sárosi and Péter Lévay. Entanglement classification of three fermions with up to nine single-particle states. *Phys. Rev. A*, 89:042310, Apr 2014.

[34] Vittorio Giovannetti, Seth Lloyd, and Lorenzo MacCone. Quantum metrology. *Phys. Rev. Lett.*, 96(1):010401, 2006.

[35] Luca Pezzé and Augusto Smerzi. Entanglement, nonlinear dynamics, and the heisenberg limit. *Phys. Rev. Lett.*, 102(10):100401, 2009.

[36] Magdalena Szczykulska, Tillmann Baumgratz, and Animesh Datta. Multiparameter quantum metrology. *Adv. Phys.: X*, 1(4):621–639, 2016.

[37] L. Pezzè and Augusto Smerzi. Quantum theory of phase estimation. *Atom Interferometry*, 188:691–741, 2014.

[38] Jing Liu, Haidong Yuan, Xiao-Ming Lu, and Xiaoguang Wang. Quantum Fisher information matrix and multiparameter estimation. *J. Phys. A Math.*, 53(2):023001, December 2019.

[39] F. Benatti, R. Floreanini, F. Franchini, and U. Marzolino. Entanglement in indistinguishable particle systems. *Physics Reports*, 878:1–27, 2020. Entanglement in indistinguishable particle systems.

[40] Benjamin Morris, Benjamin Yadin, Matteo Fadel, Tilman Zibold, Philipp Treutlein, and Gerardo Adesso. Entanglement between Identical Particles Is a Useful and Consistent Resource. *Physical Review X*, 10(4):1–23, 2020.

[41] Jan Sperling and Elizabeth Agudelo. Entanglement of particles versus entanglement of fields: independent quantum resources. 042420:1–10, 2022.

[42] Benjamin Morris, Benjamin Yadin, Matteo Fadel, Tilman Zibold, Philipp Treutlein, and Gerardo Adesso. Entanglement between identical particles is a useful and consistent resource. *Phys. Rev. X*, 10:041012, Oct 2020.

[43] Ricardo Costa de Almeida and Philipp Hauke. From entanglement certification with quench dynamics to multipartite entanglement of interacting fermions. *Phys. Rev. Res.*, 3:L032051, Aug 2021.

[44] Bikash Padhi, Chandan Setty, and Philip W Phillips. Doped twisted bilayer graphene near magic angles: proximity to wigner crystallization, not mott insulation. *Nano letters*, 18(10):6175–6180, 2018.

[45] Ingemar Bengtsson and Karol Zyczkowski. *Geometry of Quantum States: An Introduction to Quantum Entanglement*. Cambridge University Press, 2006.

[46] W. Dür and J. I. Cirac. Classification of multiqubit mixed states: Separability and distillability properties. *Phys. Rev. A*, 61(4):042314, March 2000.

[47] Otfried Gühne, Géza Tóth, and Hans J Briegel. Multipartite entanglement in spin chains. *New J. Phys.*, 7(1):229, nov 2005.

[48] Otfried Gühne and Géza Tóth. Energy and multipartite entanglement in multidimensional and frustrated spin models. *Phys. Rev. A*, 73:052319, May 2006.

[49] Michael Levin and Xiao-Gang Wen. Detecting topological order in a ground state wave function. *Phys. Rev. Lett.*, 96(11):110405, 2006.

[50] Xiao-Liang Qi and Shou-Cheng Zhang. Topological insulators and superconductors. *Rev. Mod. Phys.*, 83(4):1057–1110, 2012.

[51] Matteo Paris and Jaroslav Řeháček, editors. *Quantum State Estimation*, volume 649 of *Lecture Notes in Physics*. Springer, 2004.

[52] Manuel Gessner, Luca Pezzè, and Augusto Smerzi. Sensitivity Bounds for Multiparameter Quantum Metrology. *Phys. Rev. Lett.*, 121(13):130503, 2018.

[53] Sam A. Hill and William K. Wootters. Entanglement of a pair of quantum bits. *Phys. Rev. Lett.*, 78:5022–5025, Jun 1997.

[54] Valerie Coffman, Joydip Kundu, and William K. Wootters. Distributed entanglement. *Phys. Rev. A*, 61:052306, Apr 2000.

[55] Ricardo Costa de Almeida and Philipp Hauke. From entanglement certification with quench dynamics to multipartite entanglement of interacting fermions. *Phys. Rev. Research*, 3:L032051, Aug 2021.

[56] Tamás Juhász and David A. Mazziotti. The cumulant two-particle reduced density matrix as a measure of electron correlation and entanglement. *J. Chem. Phys.*, 125(17):174105, 2006.

[57] Werner Kutzelnigg and Debashis Mukherjee. Irreducible Brillouin conditions and contracted Schrödinger equations for n-electron systems. II. Spin-free formulation. *J. Chem. Phys.*, 116(12):4787–4801, 2002.

[58] Debashis Mukherjee and Werner Kutzelnigg. Irreducible Brillouin conditions and contracted Schrödinger equations for n-electron systems. I. The equations satisfied by the density cumulants. *J. Chem. Phys.*, 114(5):2047–2061, 2001.

[59] David A. Mazziotti, editor. *Reduced-Density-Matrix Mechanics: With Application to Many-Electron Atoms and Molecules*. Advances in Chemical Physics. John Wiley & Sons, Inc., March 2007.

[60] David A. Mazziotti. Two-electron reduced density matrix as the basic variable in many-electron quantum chemistry and physics. *Chem. Rev.*, 112(1):244–262, 2012.

[61] David A. Mazziotti. Contracted Schrödinger equation: Determining quantum energies and two-particle density matrices without wave functions. *Phys. Rev. A*, 57(6):4219–4234, 1998.

[62] David A. Mazziotti. Complete reconstruction of reduced density matrices. *Chem. Phys. Lett.*, 326(3-4):212–218, 2000.

[63] Julie T. Skolnik and David A. Mazziotti. Cumulant reduced density matrices as measures of statistical dependence and entanglement between electronic quantum domains with application to photosynthetic light harvesting. *Phys. Rev. A*, 88(3):032517, 2013.

[64] Hui Li, Songjun Li, Emma C. Regan, and et al. Imaging two-dimensional generalized wigner crystals. *Nature*, 597(7877):650–654, 2021.

[65] David A. Mazziotti. Pure- N -representability conditions of two-fermion reduced density matrices. *Phys. Rev. A*, 94(3):032516, 2016.

[66] Tamás Juhász and David A. Mazziotti. The cumulant two-particle reduced density matrix as a measure of electron correlation and entanglement. *J. Chem. Phys.*, 125(17):174105, November 2006.

[67] Werner Kutzelnigg and Debashis Mukherjee. Cumulant expansion of the reduced density matrices. *J. Chem. Phys.*, 110(2-12):2800–2809, 1999.

[68] Josef Betten. Integrity basis for a second-order and a fourth-order tensor. *Int. J. Math. Math. Sci.*, 5:354081, 1982.

[69] George Backus. A geometrical picture of anisotropic elastic tensors. *Rev. Geophys.*, 8(3):633–671, 1970.

[70] Xiao-Yang Liu and Xiaodong Wang. Fourth-order Tensors with Multidimensional Discrete Transforms. *arXiv:1705.01576*, May 2017.

[71] East Anglia. Fourth-rank tensors of the thirty-two crystal classes: multiplication tables. *Proc. R. Soc. A: Math. Phys. Eng. Sci.*, 391(1800):149–179, 1984.

[72] Mario Rosina. Reduced density operators with application to physical and chemical systems. In A. J. Coleman and R. M. Erdahl, editors, *Queens Papers in Pure and Applied Mathematics*, number 11. Queen's University, Kingston, Ontario, 1968.

[73] Pok Man Tam, Tongtong Liu, Inti Sodemann, and Liang Fu. Local probes for quantum hall ferroelectrics and nematics. *Phys. Rev. B*, 101:241103, Jun 2020.

[74] Benjamin E. Feldman, Mallika T. Randeria, András Gyenis, Fengcheng Wu, Huiwen Ji, Robert J. Cava, Allan H. MacDonald, and Ali Yazdani. Observation of a disordered axion insulator possessing topological chern bands. *Science*, 354(6310):316–321, 2016.

[75] Mallika T. Randeria, Benjamin E. Feldman, Fengcheng Wu, Hao Ding, András Gyenis, Huiwen Ji, Robert J. Cava, Allan H. MacDonald, and Ali Yazdani. Disordered weyl semimetals: Theory and transport. *Nature Physics*, 14(8):796–800, 2018.

[76] Inti Sodemann, Zhiyuan Zhu, and Liang Fu. Weyl fermions, fermi arcs, and minority-spin carriers in ferromagnetic weyl semimetals. *Physical Review X*, 7(4):041068, 2017.

[77] S. A. Parameswaran and B. E. Feldman. Fragile topology and wannier obstructions. *Journal of Physics: Condensed Matter*, 31(27):273001, 2019.

[78] Mallika T. Randeria, Kartiek Agarwal, Benjamin E. Feldman, Hao Ding, Huiwen Ji, Robert J. Cava, S. L. Sondhi, S. A. Parameswaran, and Ali Yazdani. Fragile topology and wannier obstructions in nodal line semimetals. *Nature*, 566(7743):363–367, 2019.

[79] Kartiek Agarwal, Mallika T. Randeria, Ali Yazdani, S. L. Sondhi, and S. A. Parameswaran. Surface-state signatures of the anomalous bulk spin hall effect in weyl semimetals. *Physical Review B*, 100(16):165103, 2019.

[80] M Shayegan, EP De Poortere, O Gunawan, YP Shkolnikov, E Tutuc, and K Vakili. Quantum hall effects in a two-dimensional electron system. *Phys. Stat. Sol. b*, 243:3629, 2006.

[81] T Gokmen, M Padmanabhan, and M Shayegan. Broken symmetries in doubly-degenerate two-dimensional electron systems. *Nat. Phys.*, 6:621, 2010.

[82] VA Chitta, W Desrat, DK Maude, BA Piot, NF Oliveira Jr, PHO Rappl, AY Ueta, and E Abramof. Electric-field-controlled anisotropy of the g factor in a modulation-doped quantum well. *Physica E: Low-dimensional Systems and Nanostructures*, 34:124, 2006.

[83] Y Okada, M Serbyn, H Lin, D Walkup, W Zhou, C Dhital, M Neupane, S Xu, YJ Wang, R Sankar, F Chou, A Bansil, MZ Hasan, SD Wilson, L Fu, and V Madhavan. Topological insulators and superconductors. *Science*, 341:1496, 2013.

[84] X Li, F Zhang, and AH MacDonald. Landau-level degeneracy and quantum hall ferromagnetism of a chiral spin state. *Phys. Rev. Lett.*, 116:026803, 2016.

[85] DA Abanin, SA Parameswaran, SA Kivelson, and SL Sondhi. Theory of hall plateau-plateau transitions in two-dimensional electron systems. *Phys. Rev. B*, 82:035428, 2010.

[86] A Kumar, SA Parameswaran, and SL Sondhi. Inhomogeneous superconductivity induced by quenched disorder in two-dimensional dirac semimetals. *Phys. Rev. B*, 88:045133, 2013.

[87] Z Papić, RSK Mong, A Yazdani, and MP Zaletel. Topological and interaction-induced symmetry breaking in a nearly flat band. *Phys. Rev. X*, 8:011037, 2018.

[88] P. Dziawa, B. J. Kowalski, K. Dybko, R. Buczko, A. Szczerbakow, M. Szot, E. Lusakowska, T. Balasubramanian, B. M. Wojek, M. H. Berntsen, O. Tjernberg, and T. Story. Topological crystalline insulator states in $Pb_{1-x}Sn_xSe$. *Nature Materials*, 11:1023, 2012.

[89] T. H. Hsieh, H. Lin, J. Liu, W. Duan, A. Bansil, and L. Fu. Topological crystalline insulators in the SnTe material class. *Nature Communications*, 3:982, 2012.

[90] Y. Tanaka, Z. Ren, T. Sato, K. Nakayama, S. Souma, T. Takahashi, K. Segawa, and Y. Ando. Experimental realization of a topological crystalline insulator in SnTe. *Nature Physics*, 8:800, 2012.

[91] J. Liu, W. Duan, and L. Fu. Topological crystalline insulators in the mirror-symmetry-protected regime. *Physical Review B*, 88:241303(R), 2013.

[92] M. Serbyn and L. Fu. Symmetry-protected topological phases in noninteracting metals. *Physical Review B*, 90:035402, 2014.

[93] D. J. Thouless. Quantization of particle transport. *Physical Review B*, 27:6083, 1983.

[94] R. D. King-Smith and D. Vanderbilt. Theory of polarization of crystalline solids. *Physical Review B*, 47:1651(R), 1993.

[95] I. Sodemann and L. Fu. Quantum impurity problems in topological phases of matter. *Physical Review Letters*, 115:216806, 2015.

[96] Note on inter-valley scattering. For simplicity we neglect inter-valley scattering although it has been recently shown that certain detailed aspects of the states near the impurity require understanding the intervalley scattering properties [75].

[97] Yu-Sheng Fu, Minoru Kawamura, Kazuhiko Igarashi, Hidenori Takagi, Hiroshi Hannaguri, and Takao Sasagawa. Two-component nature of superconductivity in sr2ruo4 revealed by the response to microwave irradiation. *Nature Physics*, 10:815, 2014.

[98] A. H. MacDonald. Quantum hall effect in a two-dimensional electron gas. *arXiv preprint cond-mat/9410047*, 1994.

[99] Gabriele Giuliani and Giovanni Vignale. *Quantum Theory of the Electron Liquid*. Cambridge University Press, 2008.

[100] Yang Zhang, Tongtong Liu, and Liang Fu. Electronic structures, charge transfer, and charge order in twisted transition metal dichalcogenide bilayers. *Phys. Rev. B*, 103:155142, Apr 2021.

[101] Chenhao Jin, Zui Tao, Tingxin Li, Yang Xu, Yanhao Tang, Jiacheng Zhu, Song Liu, Kenji Watanabe, Takashi Taniguchi, James C Hone, et al. Stripe phases in wse2/ws2 moir\'e superlattices. *arXiv preprint arXiv:2007.12068*, 2020.

[102] Yuya Shimazaki, Clemens Kuhlenkamp, Ido Schwartz, Tomasz Smolenski, Kenji Watanabe, Takashi Taniguchi, Martin Kroner, Richard Schmidt, Michael Knap, and Atac Imamoglu. Optical signatures of charge order in a mott-wigner state. *arXiv preprint arXiv:2008.04156*, 2020.

[103] Yuan Cao, Valla Fatemi, Ahmet Demir, Shiang Fang, Spencer L Tomarken, Jason Y Luo, Javier D Sanchez-Yamagishi, Kenji Watanabe, Takashi Taniguchi, Efthimios Kaxiras, et al. Correlated insulator behaviour at half-filling in magic-angle graphene superlattices. *Nature*, 556(7699):80, 2018.

[104] Yuan Cao, Valla Fatemi, Shiang Fang, Kenji Watanabe, Takashi Taniguchi, Efthimios Kaxiras, and Pablo Jarillo-Herrero. Unconventional superconductivity in magic-angle graphene superlattices. *Nature*, 556(7699):43, 2018.

[105] Xiaobo Lu, Petr Stepanov, Wei Yang, Ming Xie, Mohammed Ali Aamir, Ipsita Das, Carles Urgell, Kenji Watanabe, Takashi Taniguchi, Guangyu Zhang, et al. Superconductors, orbital magnets and correlated states in magic-angle bilayer graphene. *Nature*, 574(7780):653–657, 2019.

[106] Alexander Kerelsky, Leo J McGilly, Dante M Kennes, Lede Xian, Matthew Yankowitz, Shaowen Chen, K Watanabe, T Taniguchi, James Hone, Cory Dean,

et al. Maximized electron interactions at the magic angle in twisted bilayer graphene. *Nature*, 572(7767):95–100, 2019.

[107] Yuhang Jiang, Xinyuan Lai, Kenji Watanabe, Takashi Taniguchi, Kristjan Haule, Jinhai Mao, and Eva Y Andrei. Charge order and broken rotational symmetry in magic-angle twisted bilayer graphene. *Nature*, 573(7772):91–95, 2019.

[108] Yonglong Xie, Biao Lian, Berthold Jäck, Xiaomeng Liu, Cheng-Li Chiu, Kenji Watanabe, Takashi Taniguchi, B Andrei Bernevig, and Ali Yazdani. Spectroscopic signatures of many-body correlations in magic-angle twisted bilayer graphene. *Nature*, 572(7767):101–105, 2019.

[109] Youngjoon Choi, Jeannette Kemmer, Yang Peng, Alex Thomson, Harpreet Arora, Robert Polski, Yiran Zhang, Hechen Ren, Jason Alicea, Gil Refael, et al. Electronic correlations in twisted bilayer graphene near the magic angle. *Nature Physics*, 15(11):1174–1180, 2019.

[110] Matthew Yankowitz, Shaowen Chen, Hryhoriy Polshyn, Yuxuan Zhang, K Watanabe, T Taniguchi, David Graf, Andrea F Young, and Cory R Dean. Tuning superconductivity in twisted bilayer graphene. *Science*, 363(6431):1059–1064, 2019.

[111] Emilio Codecido, Qiyue Wang, Ryan Koester, Shi Che, Haidong Tian, Rui Lv, Son Tran, Kenji Watanabe, Takashi Taniguchi, Fan Zhang, et al. Correlated insulating and superconducting states in twisted bilayer graphene below the magic angle. *Science Advances*, 5(9):eaaw9770, 2019.

[112] Aaron L Sharpe, Eli J Fox, Arthur W Barnard, Joe Finney, Kenji Watanabe, Takashi Taniguchi, MA Kastner, and David Goldhaber-Gordon. Emergent ferromagnetism near three-quarters filling in twisted bilayer graphene. *Science*, 365(6453):605–608, 2019.

[113] SL Tomarken, Yuan Cao, Ahmet Demir, Kenji Watanabe, Takashi Taniguchi, Pablo Jarillo-Herrero, and RC Ashoori. Electronic compressibility of magic-angle graphene superlattices. *Physical review letters*, 123(4):046601, 2019.

[114] Uri Zondiner, Asaf Rozen, Daniel Rodan-Legrain, Yuan Cao, Raquel Queiroz, Takashi Taniguchi, Kenji Watanabe, Yuval Oreg, Felix von Oppen, Ady Stern, et al. Cascade of phase transitions and dirac revivals in magic angle graphene. *arXiv preprint arXiv:1912.06150*, 2019.

[115] Guorui Chen, Lili Jiang, Shuang Wu, Bosai Lyu, Hongyuan Li, Bheema Lingam Chittari, Kenji Watanabe, Takashi Taniguchi, Zhiwen Shi, Jeil Jung, et al. Evidence of a gate-tunable mott insulator in a trilayer graphene moiré superlattice. *Nature Physics*, 15(3):237, 2019.

[116] Guorui Chen, Aaron L. Sharpe, Patrick Gallagher, Ilan T. Rosen, Eli J. Fox, Lili Jiang, Bosai Lyu, Hongyuan Li, Kenji Watanabe, Takashi Taniguchi, Jeil Jung, Zhiwen Shi, David Goldhaber-Gordon, Yuanbo Zhang, and Feng Wang. Signatures of tunable superconductivity in a trilayer graphene moirésuperlattice. *Nature*, 572(7768):215–219, 2019.

[117] M Serlin, CL Tschirhart, H Polshyn, Y Zhang, J Zhu, K Watanabe, T Taniguchi, L Balents, and AF Young. Intrinsic quantized anomalous hall effect in a moiré heterostructure. *Science*, 2019.

[118] Xiaomeng Liu, Zeyu Hao, Eslam Khalaf, Jong Yeon Lee, Kenji Watanabe, Takashi Taniguchi, Ashvin Vishwanath, and Philip Kim. Spin-polarized correlated insulator and superconductor in twisted double bilayer graphene. *arXiv preprint arXiv:1903.08130*, 2019.

[119] Chendong Zhang, Chih-Piao Chuu, Xibiao Ren, Ming-Yang Li, Lain-Jong Li, Chuanhong Jin, Mei-Yin Chou, and Chih-Kang Shih. Interlayer couplings, moiré patterns, and 2d electronic superlattices in mos2/wse2 hetero-bilayers. *Science advances*, 3(1):e1601459, 2017.

[120] Hongyi Yu, Gui-Bin Liu, Jianju Tang, Xiaodong Xu, and Wang Yao. Moiré excitons: From programmable quantum emitter arrays to spin-orbit–coupled artificial lattices. *Science advances*, 3(11):e1701696, 2017.

[121] Kyle L Seyler, Pasqual Rivera, Hongyi Yu, Nathan P Wilson, Essance L Ray, David G Mandrus, Jiaqiang Yan, Wang Yao, and Xiaodong Xu. Signatures of moiré-trapped valley excitons in mose 2/wse 2 heterobilayers. *Nature*, 567(7746):66–70, 2019.

[122] Kha Tran, Galan Moody, Fengcheng Wu, Xiaobo Lu, Junho Choi, Kyounghwan Kim, Amritesh Rai, Daniel A Sanchez, Jiamin Quan, Akshay Singh, et al. Evidence for moiré excitons in van der waals heterostructures. *Nature*, 567(7746):71–75, 2019.

[123] Long Yuan, Biyuan Zheng, Jens Kunstmann, Thomas Brumme, Agnieszka Beata Kuc, Chao Ma, Shibin Deng, Daria Blach, Anlian Pan, and Libai Huang. Twist-angle-dependent interlayer exciton diffusion in ws 2–wse 2 heterobilayers. *Nature Materials*, pages 1–7, 2020.

[124] Weijie Li, Xin Lu, Sudipta Dubey, Luka Devenica, and Ajit Srivastava. Dipolar interactions between localized interlayer excitons in van der waals heterostructures. *Nature Materials*, pages 1–6, 2020.

[125] Mauro Brotons-Gisbert, Hyeonjun Baek, Alejandro Molina-Sánchez, Aidan Campbell, Eleanor Scerri, Daniel White, Kenji Watanabe, Takashi Taniguchi, Cristian Bonato, and Brian D Gerardot. Spin–layer locking of interlayer excitons trapped in moiré potentials. *Nature Materials*, pages 1–7, 2020.

[126] Yuya Shimazaki, Ido Schwartz, Kenji Watanabe, Takashi Taniguchi, Martin Kroner, and Ataç Imamoğlu. Strongly correlated electrons and hybrid excitons in a moiré heterostructure. *Nature*, 580(7804):472–477, 2020.

[127] Yusong Bai, Lin Zhou, Jue Wang, Wenjing Wu, Leo J McGilly, Dorri Halbertal, Chiu Fan Bowen Lo, Fang Liu, Jenny Ardelean, Pasqual Rivera, et al. Excitons in strain-induced one-dimensional moiré potentials at transition metal dichalcogenide heterojunctions. *Nature materials*, pages 1–6, 2020.

[128] Lei Wang, En-Min Shih, Augusto Ghiotto, Lede Xian, Daniel A Rhodes, Cheng Tan, Martin Claassen, Dante M Kennes, Yusong Bai, Bumho Kim, et al. Correlated electronic phases in twisted bilayer transition metal dichalcogenides. *Nature materials*, pages 1–6, 2020.

[129] Leo J McGilly, Alexander Kerelsky, Nathan R Finney, Konstantin Shapovalov, En-Min Shih, Augusto Ghiotto, Yihang Zeng, Samuel L Moore, Wenjing Wu, Yusong Bai, et al. Visualization of moiré superlattices. *Nature Nanotechnology*, 15(7):580–584, 2020.

[130] Zhiming Zhang, Yimeng Wang, Kenji Watanabe, Takashi Taniguchi, Keiji Ueno, Emanuel Tutuc, and Brian J LeRoy. Flat bands in twisted bilayer transition metal dichalcogenides. *Nature Physics*, pages 1–4, 2020.

[131] Astrid Weston, Yichao Zou, Vladimir Enaldiev, Alex Summerfield, Nicholas Clark, Viktor Zólyomi, Abigail Graham, Celal Yelgel, Samuel Magorrian, Mingwei Zhou, et al. Atomic reconstruction in twisted bilayers of transition metal dichalcogenides. *Nature Nanotechnology*, pages 1–6, 2020.

[132] Emma C Regan, Danqing Wang, Chenhao Jin, M Iqbal Bakti Utama, Beini Gao, Xin Wei, Sihan Zhao, Wenyu Zhao, Zuocheng Zhang, Kentaro Yumigeta, et al. Mott and generalized wigner crystal states in wse 2/ws 2 moiré superlattices. *Nature*, 579(7799):359–363, 2020.

[133] Yanhao Tang, Lizhong Li, Tingxin Li, Yang Xu, Song Liu, Katayun Barmak, Kenji Watanabe, Takashi Taniguchi, Allan H MacDonald, Jie Shan, et al. Simulation of hubbard model physics in wse 2/ws 2 moiré superlattices. *Nature*, 579(7799):353–358, 2020.

[134] Yang Xu, Song Liu, Daniel A Rhodes, Kenji Watanabe, Takashi Taniguchi, James Hone, Veit Elser, Kin Fai Mak, and Jie Shan. Abundance of correlated insulating states at fractional fillings of wse _{2}/ws _{2} moir\'e superlattices. *arXiv preprint arXiv:2007.11128*, 2020.

[135] Xiong Huang, Tianmeng Wang, Shengnan Miao, Chong Wang, Zhipeng Li, Zhen Lian, Takashi Taniguchi, Kenji Watanabe, Satoshi Okamoto, Di Xiao, et al. Correlated insulating states at fractional fillings of the ws2/wse2 moir\'e lattice. *arXiv preprint arXiv:2007.11155*, 2020.

[136] Yang Zhang, Noah FQ Yuan, and Liang Fu. Moiré quantum chemistry: charge transfer in transition metal dichalcogenide superlattices. *Physical Review B*, 102(20):201115, 2020.

[137] Hongyuan Li, Shaowei Li, Mit H Naik, Jingxu Xie, Xinyu Li, Jiayin Wang, Emma Regan, Danqing Wang, Wenyu Zhao, Sihan Zhao, et al. Imaging moir\'e flat bands in 3d reconstructed wse2/ws2 superlattices. *arXiv preprint arXiv:2007.06113*, 2020.

[138] Mit H Naik and Manish Jain. Ultraflatbands and shear solitons in moiré patterns of twisted bilayer transition metal dichalcogenides. *Physical review letters*, 121(26):266401, 2018.

[139] Lede Xian, Martin Claassen, Dominik Kiese, Michael M Scherer, Simon Trebst, Dante M Kennes, and Angel Rubio. Realization of nearly dispersionless bands with strong orbital anisotropy from destructive interference in twisted bilayer mos2. *arXiv preprint arXiv:2004.02964*, 2020.

[140] Mattia Angeli and AH MacDonald. γ-valley transition-metal-dichalcogenide moirè bands. *arXiv preprint arXiv:2008.01735*, 2020.

[141] Zhen Zhan, Yipei Zhang, Guodong Yu, Francisco Guinea Jose Angel Silva-Guillen, and Shengjun Yuan. Multi-ultraflatbands tunability and effect of spin-orbit coupling in twisted bilayer transition metal dichalcogenides. *arXiv preprint arXiv:2005.13868*, 2020.

[142] Somepalli Venkateswarlu, Andreas Honecker, and Guy Trambly de Laissardière. Electronic localization in twisted bilayer mos _2 with small rotation angle. *arXiv preprint arXiv:2005.13054*, 2020.

[143] Stephen McDonnell, Angelica Azcatl, Rafik Addou, Cheng Gong, Corsin Battaglia, Steven Chuang, Kyeongjae Cho, Ali Javey, and Robert M Wallace. Hole contacts on transition metal dichalcogenides: Interface chemistry and band alignments. *ACS nano*, 8(6):6265–6272, 2014.

[144] Fengcheng Wu, Timothy Lovorn, Emanuel Tutuc, Ivar Martin, and AH MacDonald. Topological insulators in twisted transition metal dichalcogenide homobilayers. *Physical review letters*, 122(8):086402, 2019.

[145] Kazuyuki Uchida, Shinnosuke Furuya, Jun-Ichi Iwata, and Atsushi Oshiyama. Atomic corrugation and electron localization due to moiré patterns in twisted bilayer graphenes. *Physical Review B*, 90(15):155451, 2014.

[146] Jiří Klimeš, David R Bowler, and Angelos Michaelides. Van der waals density functionals applied to solids. *Physical Review B*, 83(19):195131, 2011.

[147] Georg Kresse and Jürgen Furthmüller. Efficiency of ab-initio total energy calculations for metals and semiconductors using a plane-wave basis set. *Computational materials science*, 6(1):15–50, 1996.

[148] Rafi Bistritzer and Allan H MacDonald. Moiré bands in twisted double-layer graphene. *Proceedings of the National Academy of Sciences*, 108(30):12233–12237, 2011.

[149] Bikash Padhi, R Chitra, and Philip W Phillips. Generalized wigner crystallization in moiré materials. *Physical Review B*, 103(12):125146, 2021.

[150] Zhiren Zheng, Qiong Ma, Zhen Bi, Sergio de la Barrera, Ming-Hao Liu, Nannan Mao, Yang Zhang, Natasha Kiper, Kenji Watanabe, Takashi Taniguchi, et al. Unconventional ferroelectricity in moiré heterostructures. *Nature*, 588(7836):71–76, 2020.

[151] Kevin Slagle and Liang Fu. Charge transfer excitations, pair density waves, and superconductivity in moir\'e materials. *arXiv preprint arXiv:2003.13690*, 2020.

[152] J Zaanen, GA Sawatzky, and JW Allen. Band gaps and electronic structure of transition-metal compounds. *Physical Review Letters*, 55(4):418, 1985.

[153] Haining Pan, Fengcheng Wu, and Sankar Das Sarma. Band topology, hubbard model, heisenberg model, and dzyaloshinskii-moriya interaction in twisted bilayer wse _2. *arXiv preprint arXiv:2004.04168*, 2020.

[154] Haining Pan, Fengcheng Wu, and Sankar Das Sarma. Quantum phase diagram of a moir\'e-hubbard model. *arXiv preprint arXiv:2008.08998*, 2020.

[155] Zhen Bi and Liang Fu. Excitonic density wave and spin-valley superfluid in bilayer transition metal dichalcogenide. *arXiv preprint arXiv:1911.04493*, 2019.

[156] Helena A. Merker, Harry Heiberger, Linh Nguyen, Tongtong Liu, Zhantao Chen, Nina Andrejevic, Nathan C. Drucker, Ryotaro Okabe, Song Eun Kim, Yao Wang, Tess Smidt, and Mingda Li. Machine learning magnetism classifiers from atomic coordinates. *iScience*, 25(10):105192, 2022.

[157] Albert Fert. Nobel Lecture: Origin, development, and future of spintronics. *Rev. Mod. Phys.*, 80(4):1517–1530, December 2008.

[158] Marinus T. Vlaardingerbroek and Jacques A. Boer. *Magnetic Resonance Imaging: Theory and Practice*. Springer Science & Business Media, 2003.

[159] A. Manchon, J. Železný, I.M. Miron, T. Jungwirth, J. Sinova, A. Thiaville, K. Garello, and P. Gambardella. Current-induced spin-orbit torques in ferromagnetic and antiferromagnetic systems. *Rev. Mod. Phys.*, 91(3):035004, September 2019.

[160] L.A. Artsimovich. Tokamak devices. *Nucl. Fusion*, 12(2):215–252, March 1972.

[161] Helmut Wiedemann. *Particle Accelerator Physics*. Springer Nature, January 2015.

[162] Neil A. Gershenfeld and Isaac L. Chuang. Bulk Spin-Resonance Quantum Computation. *Science*, 275(5298):350–356, January 1997.

[163] Leon Balents. *Spin Liquids in Frustrated Magnets*. *Nature*, 464(7286):199–208, 2010.

[164] B. Keimer, S. A. Kivelson, M. R. Norman, S. Uchida, and J. Zaanen. From quantum matter to high-temperature superconductivity in copper oxides. *Nature*, 518(7538):179–186, February 2015.

[165] C. G. Shull and J. Samuel Smart. Detection of Antiferromagnetism by Neutron Diffraction. *Phys. Rev.*, 76(8):1256–1257, October 1949.

[166] S. Mühlbauer, B. Binz, F. Jonietz, C. Pfleiderer, A. Rosch, A. Neubauer, R. Georgii, and P. Böni. Skyrmion Lattice in a Chiral Magnet. *Science*, 323(5916):915–919, February 2009.

[167] K. Binder and A. P. Young. Spin glasses: Experimental facts, theoretical concepts, and open questions. *Rev. Mod. Phys.*, 58(4):801–976, October 1986.

[168] Arnab Banerjee, Jiaqiang Yan, Johannes Knolle, Craig A. Bridges, Matthew B. Stone, Mark D. Lumsden, David G. Mandrus, David A. Tennant, Roderich Moessner, and Stephen E. Nagler. Neutron scattering in the proximate quantum spin liquid alpha-$RuCl_3$. *Science*, 356(6342):1055–1059, June 2017.

[169] Yi Zhou, Kazushi Kanoda, and Tai-Kai Ng. Quantum spin liquid states. *Rev. Mod. Phys.*, 89(2):025003, April 2017.

[170] Stephen W. Lovesey. *Theory of Neutron Scattering from Condensed Matter: Volume I: Nuclear Scattering*. International Series of Monographs on Physics. Oxford University Press, Oxford, New York, October 1986.

[171] Luuk J. P. Ament, Michel van Veenendaal, Thomas P. Devereaux, John P. Hill, and Jeroen van den Brink. Resonant inelastic x-ray scattering studies of elementary excitations. *Rev. Mod. Phys.*, 83(2):705–767, June 2011.

[172] Samuel V. Gallego, J. Manuel Perez-Mato, Luis Elcoro, Emre S. Tasci, Robert M. Hanson, Koichi Momma, Mois I. Aroyo, and Gotzon Madariaga. *MAGNDATA*: towards a database of magnetic structures. I. The commensurate case. *J. Appl. Crystallogr.*, 49(5):1750–1776, 10 2016.

[173] Samuel V. Gallego, J. Manuel Perez-Mato, Luis Elcoro, Emre S. Tasci, Robert M. Hanson, Mois I. Aroyo, and Gotzon Madariaga. *MAGNDATA*: towards a database of magnetic structures. II. The incommensurate case. *J. Appl. Crystallogr.*, 49(6):1941–1956, 12 2016.

[174] Zhendong Li, Sheng Guo, Qiming Sun, and Garnet Kin-Lic Chan. Electronic landscape of the P-cluster of nitrogenase as revealed through many-electron quantum wavefunction simulations. *Nat. Chem.*, 11(11):1026–1033, November 2019.

[175] Wei Huang, Deng-Hui Xing, Jun-Bo Lu, Bo Long, W. H. Eugen Schwarz, and Jun Li. How Much Can Density Functional Approximations (DFA) Fail? The Extreme Case of the FeO4 Species. *J. Chem. Theory Comput.*, 12(4):1525–1533, April 2016.

[176] Fang Liu, Tzuhsiung Yang, Jing Yang, Eve Xu, Akash Bajaj, and Heather J. Kulik. Bridging the Homogeneous-Heterogeneous Divide: Modeling Spin for Reactivity in Single Atom Catalysis. *Front. Chem.*, 7:219, 2019.

[177] Anubhav Jain, Shyue Ping Ong, Geoffroy Hautier, Wei Chen, William Davidson Richards, Stephen Dacek, Shreyas Cholia, Dan Gunter, David Skinner, Gerbrand Ceder, and Kristin A. Persson. Commentary: The Materials Project: A materials genome approach to accelerating materials innovation. *APL Mater.*, 1(1):011002, July 2013.

[178] Trevor David Rhone, Wei Chen, Shaan Desai, Steven B. Torrisi, Daniel T. Larson, Amir Yacoby, and Efthimios Kaxiras. Data-driven studies of magnetic two-dimensional materials. *Sci. Rep.*, 10(1):15795, September 2020.

[179] Fawei Zheng and Ping Zhang. MagGene: A genetic evolution program for magnetic structure prediction. *Comput. Phys. Commun.*, 259:107659, February 2021.

[180] Georgios Katsikas, Charalampos Sarafidis, and Joseph Kioseoglou. Machine Learning in Magnetic Materials. *Phys. Status Solidi B*, 258(8):2000600, 2021.

[181] Nathan C. Frey, Matthew K. Horton, Jason M. Munro, Sinéad M. Griffin, Kristin A. Persson, and Vivek B. Shenoy. High-throughput search for magnetic and topological order in transition metal oxides. *Sci. Adv.*, 6(50):eabd1076, December 2020.

[182] Dingchen Wang, Songrui Wei, Anran Yuan, Fanghua Tian, Kaiyan Cao, Qizhong Zhao, Yin Zhang, Chao Zhou, Xiaoping Song, Dezhen Xue, and Sen Yang. Machine Learning Magnetic Parameters from Spin Configurations. *Adv. Sci.*, 7(16):2000566, 2020.

[183] Anjana M. Samarakoon, Kipton Barros, Ying Wai Li, Markus Eisenbach, Qiang Zhang, Feng Ye, V. Sharma, Z. L. Dun, Haidong Zhou, Santiago A. Grigera, Cristian D. Batista, and D. Alan Tennant. Machine-learning-assisted insight into spin ice $Dy_2Ti_2O_7$. *Nat. Commun.*, 11(1):892, February 2020.

[184] Juan Rodríguez-Carvajal and Jacques Villain. Magnetic structures. *C. R. Phys*, 20(7):770–802, November 2019.

[185] Shyue Ping Ong, William Davidson Richards, Anubhav Jain, Geoffroy Hautier, Michael Kocher, Shreyas Cholia, Dan Gunter, Vincent L. Chevrier, Kristin A. Persson, and Gerbrand Ceder. Python Materials Genomics (pymatgen): A robust, open-source python library for materials analysis. *Comput. Mater. Sci.*, 68:314–319, February 2013.

[186] Zhantao Chen, Nina Andrejevic, Tess Smidt, Zhiwei Ding, Qian Xu, Yen-Ting Chi, Quynh T. Nguyen, Ahmet Alatas, Jing Kong, and Mingda Li. Direct Prediction of Phonon Density of States With Euclidean Neural Networks. *Adv. Sci.*, 8(12):2004214, March 2021.

[187] Dai-Wei Qu, Bin-Bin Chen, Hong-Chen Jiang, Yao Wang, and Wei Li. Spin-triplet pairing induced by near-neighbor attraction in the extended hubbard model for cuprate chain. *Commun. Phys.*, 5(1):257, 2022.

[188] L. J. Brillson, E. Burstein, and L. Muldawer. *Phys. Rev. B*, 9:1547, 1974.

[189] M. Serbyn and L. Fu. *Phys. Rev. B*, 90:035402, 2014.

[190] J. Liu, W. Duan, and L. Fu. *Phys. Rev. B*, 88:241303(R), 2013.

[191] Y. Tanaka, Z. Ren, T. Sato, K. Nakayama, S. Souma, T. Takahashi, K. Segawa, and Y. Ando. *Nat. Phys.*, 8:800, 2012.

[192] Y. Okada, M. Serbyn, H. Lin, D. Walkup, W. Zhou, C. Dhital, M. Neupane, S. Xu, Y. J. Wang, R. Sankar, F. Chou, A. Bansil, M. Z. Hasan, S. D. Wilson, L. Fu, and V. Madhavan. *Science*, 341(6153):1496, 2013.

[193] R. D. King-Smith and D. Vanderbilt. *Phys. Rev. B*, 47:1651(R), 1993.

[194] I. Sodemann, Z. Zhu, and L. Fu. *Phys. Rev. X*, 7:041068, 2017.

[195] John P Perdew, Kieron Burke, and Matthias Ernzerhof. Generalized gradient approximation made simple. *Physical review letters*, 77(18):3865, 1996.

[196] Zhiyong Y Zhu, Yingchun C Cheng, and Udo Schwingenschlögl. Giant spin-orbit-induced spin splitting in two-dimensional transition-metal dichalcogenide semiconductors. *Physical Review B*, 84(15):153402, 2011.